SMART NANOCOMPOSITES

Volume 1, Issue 1

TABLE OF CONTENTS

Nova Science Publishers, Inc.
Hauppauge, New York
2010

Smart Nanocomposites

This Journal presents new studies in the fast growing area of smart materials, in particular, composite nanostructured materials. It focuses on the physics and physical chemistry of surfaces, interfaces, thin films and coatings, nanoparticles and other nanostructures, as well as on their new and smart applications. Original approaches in fabrication and applications of nanostructured materials will get special attention. Nanostructured ceramics, alloys, various nanocarbon forms (nanotubes, fullerenes, graphene) and their composites used in sensors (including single molecule sensing) and actuators, artificial metabolism, drug delivery, selective membranes, fuel cells, energy storage, and photovoltaics are just a few examples of new classes of materials and applications that are within the scope of the Journal. It features the results of interdisciplinary research from universities, national labs, and privately owned companies.

The Journal is peer-reviewed with the highest standards and quality of publications. The purpose of this Journal is to bring the most up-to-date advances in nanotechnology together, and to give research groups the opportunity to compare their results with other groups' data. To achieve this, the Journal focuses mostly on practical applications of nanodevices, and on proof of the concept publications. Areas of interest include (but not are limited to): sensors, smart membranes, smart coatings for corrosion protection, aspects of significance to nanorobots: power supplies, nanorobot manipulating devices, and microchips for artificial intelligence. The Journal also deals with safety issues: safety of nanotechnology to the environment, controlling the nanodevices, and other aspects.

Smart Nanocomposites

is published quarterly by

Nova Science Publishers, Inc.

400 Oser Avenue, Suite 1600

Hauppauge, New York 11788-3619, U.S.A.

Telephone: (631) 231-7269

Fax: (631) 231-8175

E-mail: novapublishers@earthlink.net

Web: www. novapublishers.com

Institutional Subscription Rate (2010): $195

Personal Subscription Rate (2010): $50

ISSN: 1949-4823

Instructions for manuscript preparation can be found on our website.

Smart Nanocomposites
Volume 1, Issue 1.
ISSN: 1949-4823

TWO DIFFERENT CHEMICAL ROUTES TO OBTAIN GRAPHENE OR FEW-LAYER GRAPHITE

S. A. V. Jannuzzi[a], S. Dubin[b], M. J. Allen[b], J. Wassei[b], S. A. Moshkalev[a] and R. B. Kaner[b,c]

[a]Center for Semiconductor Components, University of Campinas, Campinas, São Paulo, Brazil.
[b]Department of Chemistry and Biochemistry, University of California, Los Angeles, California, USA
[c]Department of Materials Science and Engineering, and California NanoSystems Institute, University of California, Los Angeles, California, USA

ABSTRACT

Two different chemical routes have been applied to produce graphite oxide (GO) and pure hydrazine was used to convert GO into few-layer graphite or single-layer graphite (graphene). The products were characterized by X-ray diffractometry, scanning electron microscopy and atomic force microscopy (AFM). Graphene in-plane resistance has been measured by resistor device, while out-of-plane resistance has been measured by conductive AFM.

INTRODUCTION

New carbon nanoforms, single-layer graphite (graphene) or few-layer graphite (FLG), have many potential applications in nanoelectronics due to high charge density and mobility. Electrons can undergo ballistic transport as easy as holes on an atomically flat sp^2 carbon surface. The possibility of solution-based mass production of graphene or FLG has been recently demonstrated [1].

Graphene or FLG have been produced by a number of different methods and most of them are either time consuming or have low yields. Highly oriented pyrolytic graphite can be repeatedly peeled using an adhesive tape and transferred to silicon substrate [2]. However, single sheets are few and need to be found among a myriad of multi-layers flakes. Alternatively, silicon carbide can be reduced to yield graphene, but large samples need temperatures over 1100 °C [3]. All of these methods are difficult to scale up in order to achieve mass production of graphene or FLG.

Although single-layer GO is easy to obtain, this material is an electrical insulator. The removal of oxygen functional groups results in electrical conductivity 10^8 times higher, which is comparable to peeled HOPG samples [3]. This process is carried out by reduction in pure hydrazine, where hydrazinium salt is formed, yielding solution-stable high-conductive graphene sheets ready to device production.

Detailed studies of graphene-based devices have been carried out by this group [4,5], but they were based on graphite oxide produced by one method. By varying this method, different kind of graphite oxides can be produced, consequently, different characteristics of chemically converted graphene can be achieved. Note that graphite oxide may be useful not only for nanoelectronic applications, but also to produce GO/polymer conductive nanocomposites [6] and polymer supported carbon ultra thin films [7].

EXPERIMENTAL SECTION

Oxidation by Hummers' Method

The synthesis of GO followed the modified Hummers method proposed by Kovtyukhova *et al.* [8], who claim that a pre-oxidation step is necessary for complete oxidation of graphite flakes, avoiding formation of graphite-core/GO-shell particles [9]. The pre-oxidation was carried out with 12 g of powder graphite (*Bay Carbon*, 325 mesh, SP-1) pre-oxidized using 10 g of potassium persulfate (*Alpha Aesar*, 99%), 10 g of phosphorous pentoxide (*Sigma-Aldrich*, 98%) and 50 mL of concentrated sulfuric acid (*Sigma-Aldrich* 95-98%) for 5h at 90°C. The oxidation was performed using 460 mL of concentrated sulfuric acid with 60 g of potassium permanganate (*Sigma-Aldrich*, 99+%) for 2h at 10 °C (ice bath).

Finally, 920 mL of water was added dropwise and the oxidation step is ended by 50 mL of hydrogen peroxide (*Fischer Scientific*, 30%) addition. Hummer's GO was purified by centrifugation (*Allegra X 15-R Beckman Coulter*, 4750 RPM, 30 minutes) with HCl 10% (5L) and Milli-Q® water (5.6L) and also by dialysis.

Oxidation by Brodie's Method

The oxidation by Brodie's method [10] was performed as described by Szabó *et al* [11]. It has been used 1 g of powder graphite (*Bay Carbon*, 325 mesh, SP-1) mixed with 20 mL of fuming nitric acid (*Fluka Analytical*, 100%) and 8.5 g of sodium chlorate (*Fluka*, 99%) was added very slowly to avoid deflagration. The reaction was heated to 60 °C and held for 5 days. After this, the mixture was diluted in water, filtered and washed with 1.0 L of HCl 3 mol/L, centrifuged with 8.6 L of Milli-Q® water to remove acid and impurities. The dispersion was dried in vacuum oven at 60 °C overnight to yield a metallic gray strong GO paper. The reduction procedure was the same described before using pure hydrazine.

Reduction in Pure Hydrazine

A solution of ~3 %-wt graphite oxide was filtered to produce GO paper. It was put in anhydrous hydrazine (*Sigma-Aldrich*, 98%) to produce 1 g/L solution. Within 2-3 days, there were no more bubbles evolving, which is an evidence that the reduction is complete. The chemically converted graphene was purified by centrifugation (2000 RPM, 40 minutes) and 200 μL of the top part was diluted in 800 μL of pure hydrazine to produce a solution for spin-coating [5].

Scanning Electron Microscopy (SEM) and Atomic Force Microscopy (AFM) Sample Preparation

The centrifuged and diluted hydrazine-converted graphene was spin-coated on oxygen-plasma treated SiO_2/doped Si substrates. The spin coating speed was 1300 RPM for period of 50 s. The silicon oxide was thermally grown and had 300 Å of thickness. SEM images were acquired using JEOL JSM-6700F field emission scanning electron microscope. The AFM measurements were performed in a Digital Instruments Dimension 5000 atomic force microscope and the images were treated using the WSxM 4.0 [12].

Conductive Atomic Force Microscopy (C-AFM) and Resistor Device Sample Preparation

As-prepared substrates for SEM/AFM described above received gold-patterned pads through a conventional photolithography/lift-off procedure. Some gold pads and the bottom of the substrates were scratched in order to expose the doped silicon underneath; a small piece of indium was placed and smashed to bridge the gold pad and the doped silicon; the substrates were fastened over a coin-shaped metallic sample holder using a conductive epoxy resin (*Chemtronics*). A scheme is presented in the Figure 1a.

The resistance between several spots of the circuit and the sample holder was measured with a multimeter and ranged from 15 to 55 Ω. The C-AFM measurements were performed with Extended TUNA module. Resistor devices were produced by changing the mask. Square-patterned gold pads with 7 μm of channel length were laid down and graphene bridging two gold pads was searched using an optical microscope. Current-bias curves of several specimens were collected using Keithley 4200 SCS probe station.

X-Ray Diffractometry (XRD)

Powder X-ray diffractometry of GO was performed in a Shimadzu X'Pert PRO PANanalytical diffractometer, with 2θ range from 6-100 degree and step scan of 0.084 degree.

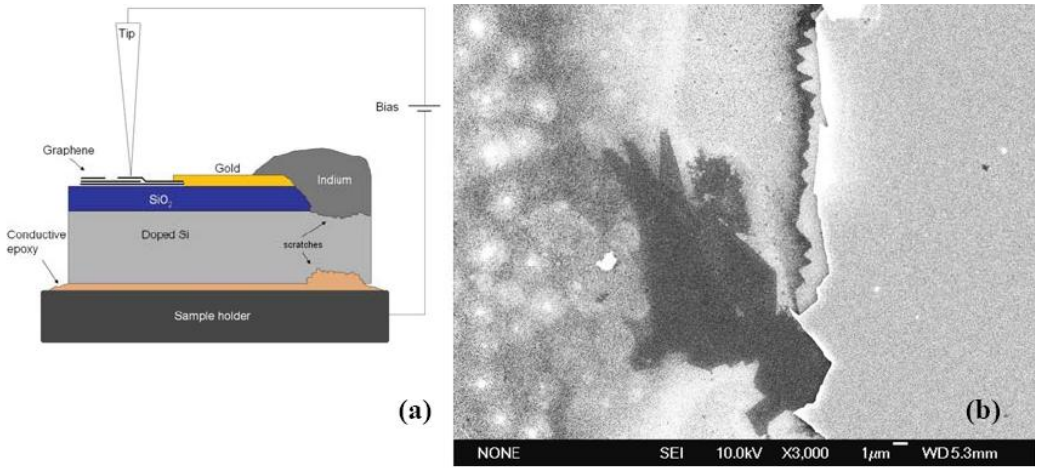

Figure 1. Schematic sample preparation for C-AFM (a) and SEM image of a suitable few-layer graphite for C-AFM because it is partially overlapped by gold pad (b).

RESULTS AND DISCUSSION

Powder X-ray diffractometry of graphite oxides are presented in Figure 2.

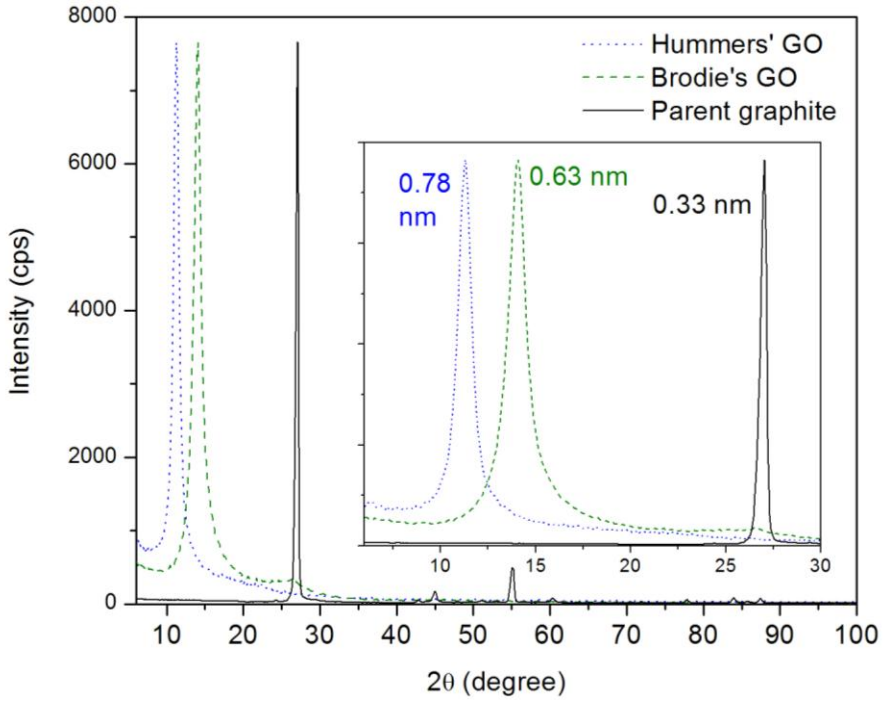

Figure 2. X-ray diffractometry of the starting graphite and the graphite oxides produced by Hummers' and Brodie's methods. The insert shows only the d_{002} reflection and the respective interlayer distance of the materials.

The graphite's most intense peak at 27° is related to the reflection of plane 002, whose position is related to the interlayer spacing (0.33 nm). The oxygen intercalated functional groups which are predominantly epoxys and 1,3-ethers and the defects caused by the oxidation yield an increase in interlayer distance to 0.78 nm in the Hummers' GO (H-GO) and to 0.63 nm in the Brodie's GO (B-GO). The great difference between GOs diffractograms and the starting graphite are evidence of good conversion in GO and use of an appropriate purification procedure.

Moisture is known to play an important role in an interlayer spacing [11]. It is important to note that GO drying was performed here differently in the two methods: H-GO was air-dried while the B-GO was dried in a vacuum oven. Therefore, it is very likely that intercaled water content is greater for H-GO. This can explain, at least in part, the significant difference in interlayer distances (~1 Å), which can be also due to different chemical functionalities inserted by the two different oxidation procedures.

While H-GO and B-GO exhibit similarity in the XRD pattern, the morphology of the hydrazine-reduced products has great differences.

Figure 3 shows SEM images of chemically converted graphene from H-GO (H-graphene) and from B-GO (B-graphene) after the reaction in hydrazine.

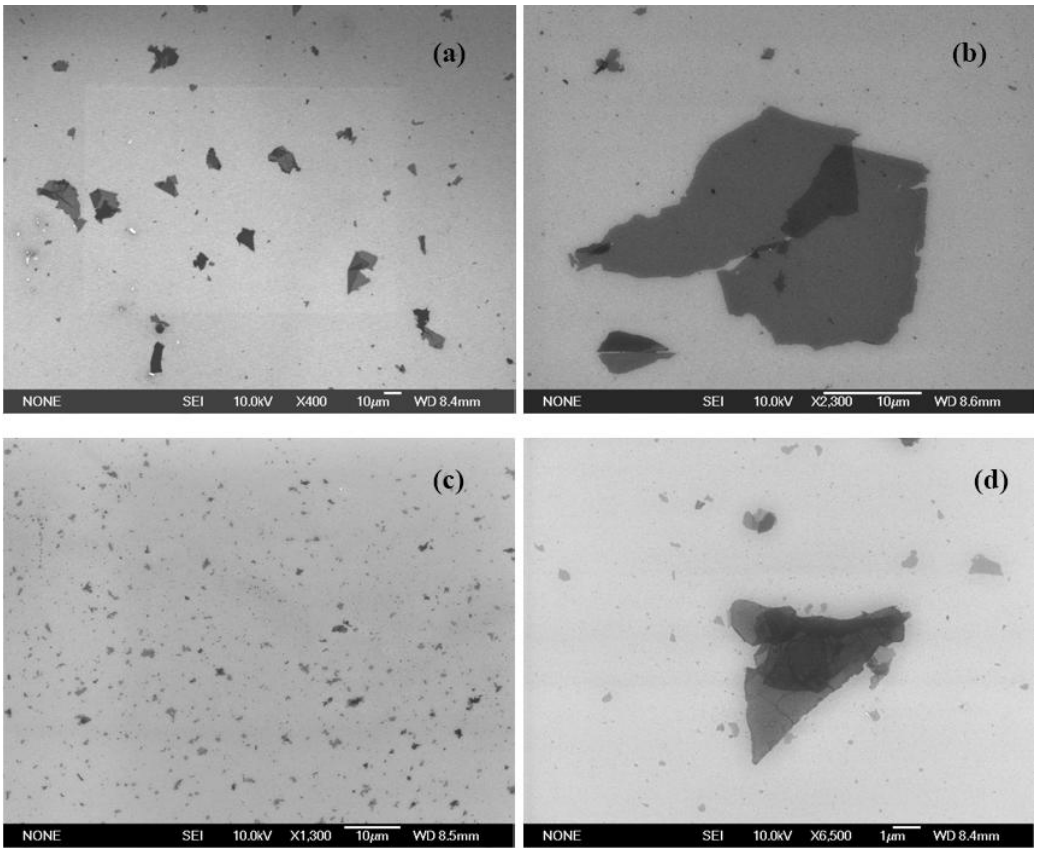

Figure 3. SEM images of chemically converted graphene from H-GO (a) and (b) and from B-GO (c) and (d) observed on SiO_2/Si substrates.

H-graphene samples exhibit uniformly-distributed large single sheets, with sizes ranging from 7 to 45 μm and with average size of 10 μm. On the other hand, B-graphene samples show few single-layered specimens with sizes ranging from 0.4-5 μm and with average size of 1 μm.

In the SEM inspections, the number of layers in specimens can be estimated roughly. Conclusions that such specimens consist of one layer are usually based only on the their low contrast and transparency that depend strongly on the layer thickness. For instance, Figure 3b shows a clear overlap (darker area) of two sheets (lighter areas). However, the number of layers can only be addressed precisely by Raman spectroscopy [13] or by measurement of the step heights using AFM.

Figure 4 shows tapping mode images of H-graphene.

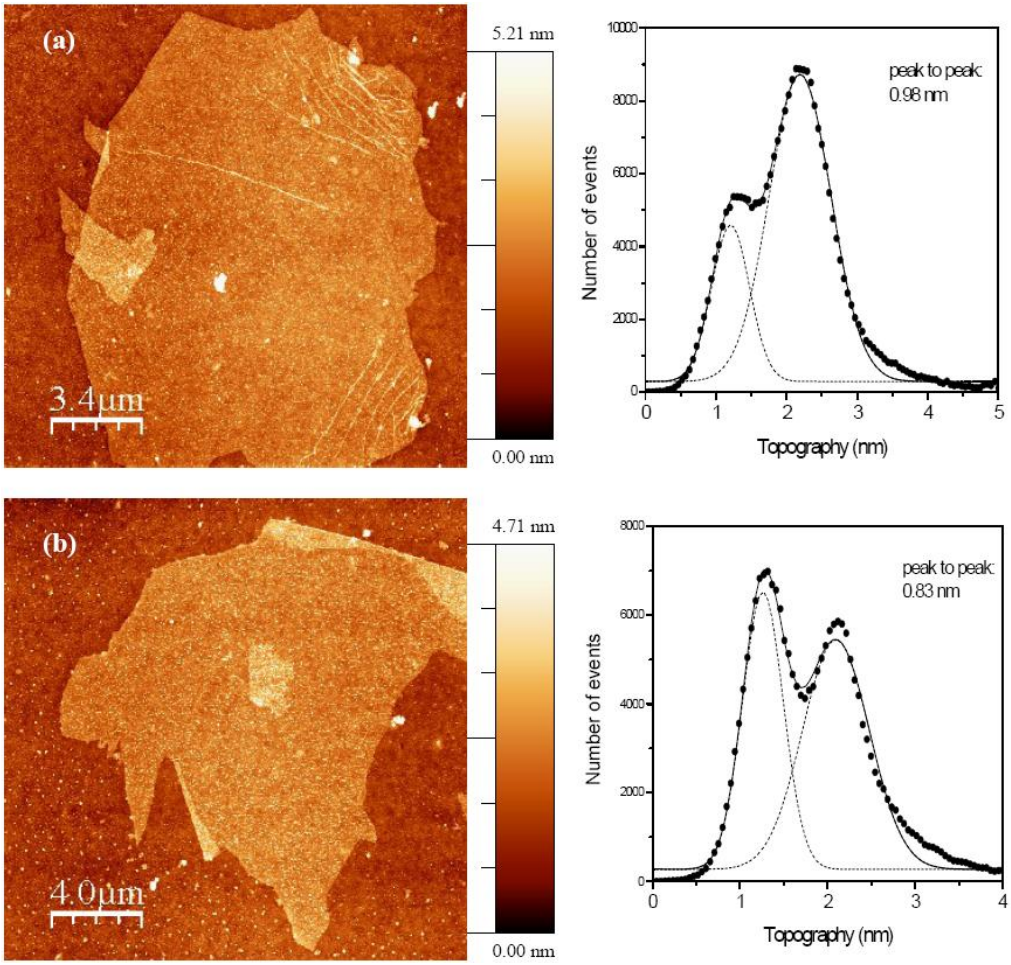

Figure 4. AFM tapping mode images of H-graphene and the respective topography histogram fitted with Gaussian peaks (dotted curves). The scan sizes are 17x17 μm (a) and 20x20 μm (b).

The average step height is measured in the histogram. Each pixel is an event and is addressed to a *z* value. When the frequency of each event is plotted against the z value (topography), we have a distribution of the *z* values over the height range. The bimodal

histograms show that there are two frequent *z* values, which comprises the substrate and the graphene sheet. Therefore, the peak-to-peak distance means the average step height. If these two superposing surfaces were ideally flat and if the experimental errors are small enough, the histogram would be in a form of two Dirac's delta functions whose displacement would be the interlayer distance. On the other hand, if step height is given by a line profile, the overall information is lost and it is just considered very local information, not statistically representative of the whole image.

The average step heights ranged from 0.83 to 0.98 nm (Figure 4a,b), which is in fairly agreement with the values currently reported in the literature: from 0.6 to 1.0 nm. The observed substrate-graphene spacing is larger than the expected graphene-graphene spacing (0.33 nm), this is probably due to differences in the tip attraction/repulsion between the semimetallic graphene and the insulating substrate. Under ambient conditions, a thin layer of adsorbed water on graphene comprises an additional complication to the measurements [14].

The B-graphene size as determined by AFM agreed with what was found using SEM. Images of many spots over the substrate showed nano-sized graphene with crystallite size ranging from 450 nm to 1.2 μm. Figure 5 presents one topographic image acquired. The average thickness was above 1 nm, which indicates double-layered graphenes.

Electrical characterization can also be performed using an atomic force microscope. In the C-AFM mode, a bias is applied between the metal-coated tip and the sample holder. As the tip scans the sample in a contact mode, the electrical current in each point is recorded and displayed in the *z* scale of the image. That is why it is necessary to have a conductive path between graphene and the microscope sample holder (Figure 1a). Another C-AFM working mode is the feedback-on mode, where the user sets an electrical current setpoint and the bias floats in order to achieve the set bias.

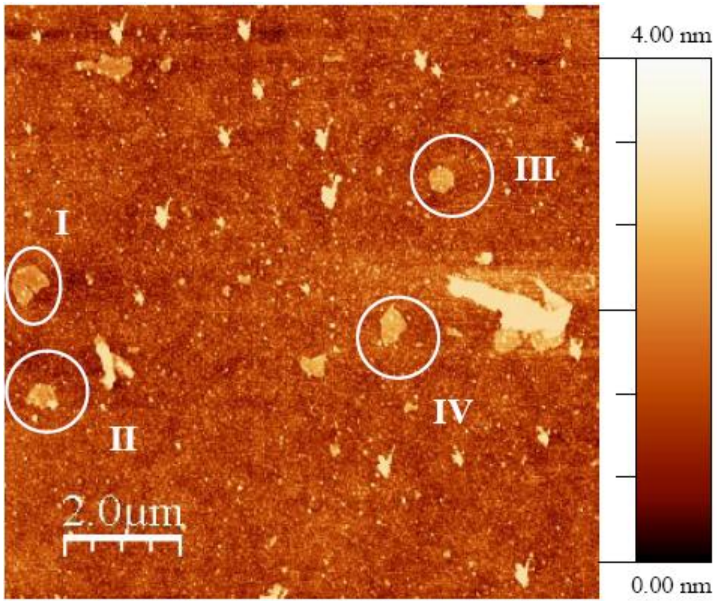

Figure 5. AFM tapping mode image of B-graphene. The regions I-IV show nano-sized graphene with 450-600 nm lateral dimensions and with thickness of 1.13 nm (I), 1.15 nm (II), 1.15 nm (III), 1.18 nm (IV).

This mode was found to be not suitable to image insulating substrate/semimetallic graphene since sudden huge bias must have been applied when the tip was scanning the substrate. C-AFM is a straightforward and useful tool to characterize local resistivity over a graphene sheet as well as π coupling between stacked sheets of a few-layer crystallite. The most time-consuming step was the sample preparation. Once good conditions of deposition are found, a photolithography/lift-off process is done and suitable pieces of graphene can be searched in the optical microscope (Figure 6).

Geim *et al.* [15] used the well-known interference effect at a specific SiO_2 thickness (300 nm) on Si to visualize graphene single sheets under white light. This fact has included simple optical microscopy in the set of techniques that allow the graphene study. Figure 6 presents two images of optical microscopy of H-graphene samples prepared to C-AFM.

Conductive AFM measurements were performed on H-graphene.

Figure 7a,c present the usual contact mode image and of two few-layer graphite flakes and Figure 7b,d exibit the corresponding electrical current map. One can notice that the current profile is not continuous; it is a dot-like profile, possibly due to subtle tip hopping during the scan which could make the electrical contact intermittent.

Nevertheless, fine details on graphene crystal can be clearly seen on the current map. The circled area in Figure 7c indicates a defect of the crystal, an area where stacked graphene sheets did not covered. There is correspondence on the current map in Figure 7d, since no current could flow due to the defect. More examples of this observation can be seen in many other spots over the images.

C-AFM also allows the acquisition of current-bias curves (I-V curves) on designed spots over the scanned field.

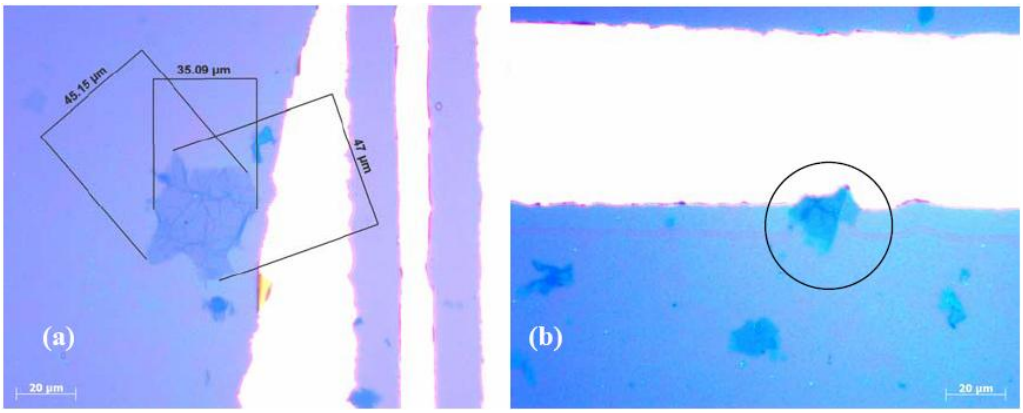

Figure 6. Optical microscopy of H-graphene on thermally grown SiO_2 (300 Å) on Si. Bright areas are gold pads. A large piece of graphene not suitable to C-AFM (a) and a few-layer graphite partially overlapped by the gold pad suitable for C-AFM (b).

Figures 7e,f show I-V curve acquired where the arrows are pointing on Figure 7c and Figure 7d respectively. The resistances of the few-layer graphite flakes measured in the –30 to 30 mV bias interval ranged from MΩ to GΩ depending on the number of layers in FLG at the point of measurements and on the quality of the atomic lattice. The few-layer graphite sample shown in Figure 7a has 6.99 nm of step height, which comprises 7-11 graphene sheets. The resistance measured on the black spot is 9.6 GΩ (Figure 7e).

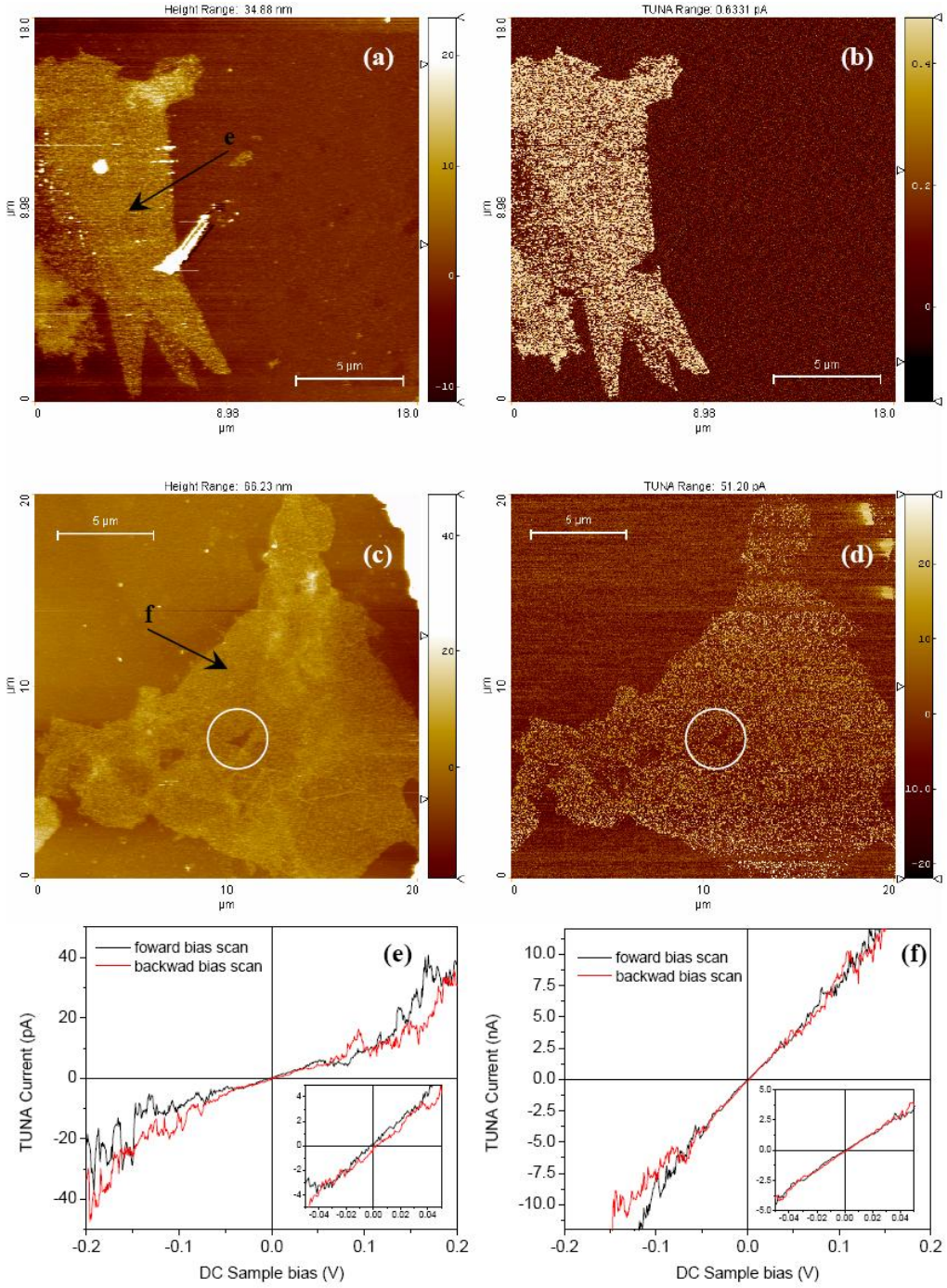

Figure 7. AFM contact mode images (a,c), the respective electrical current map (b,d) of two few-layer H-graphene and I-V curves collected on the point shown by the arrows (e,f). The height range is 0-34.88 nm in (a) and 0-66.23 nm in (c). The current range is 0-0.6331 pA in (b) and 0-51.20 pA in (d).

On the other hand, the FLG of Figure 7c has 6.10 nm of step height (6-10 sheets) and the registered I-V curve (Figure 7f) shows resistance of 13.4 MΩ. This observation may be

understood when it is considered that each stacked graphene platelet adds a resistance connected in series, enhancing the resistance of the system. The quality of the chemically reduced crystallite plays also an important role in its conductivity properties. Each graphene layer has its own defect-rich regions and graphitic (defectless) regions, which may be not matched vertically, so that a better conductive path may be formed through multiple layers of graphene when they are stacked. While C-AFM is a valuable tool to measure the out-of-plane graphene resistance, fabrication of graphene resistors allows measurements of the in-plane resistance.

Figure 8 presents one example of the I-V curve acquired from H-graphene resistor devices. They show Ohmic behavior with resistances ranging from 55 kΩ to 500 kΩ, which are 10^3-10^6 times lower than the out-of-plane resistance measured with C-AFM. Resistor devices were not built using B-graphene due to the nanometric size of specimens. The great discrepancy between a pristine graphite resistance and chemically converted graphene resistance is the most important drawback of graphene synthesis using the described above chemical route. Other methods may yield graphenes with lower resistance, but their throughput may not be so high [5].

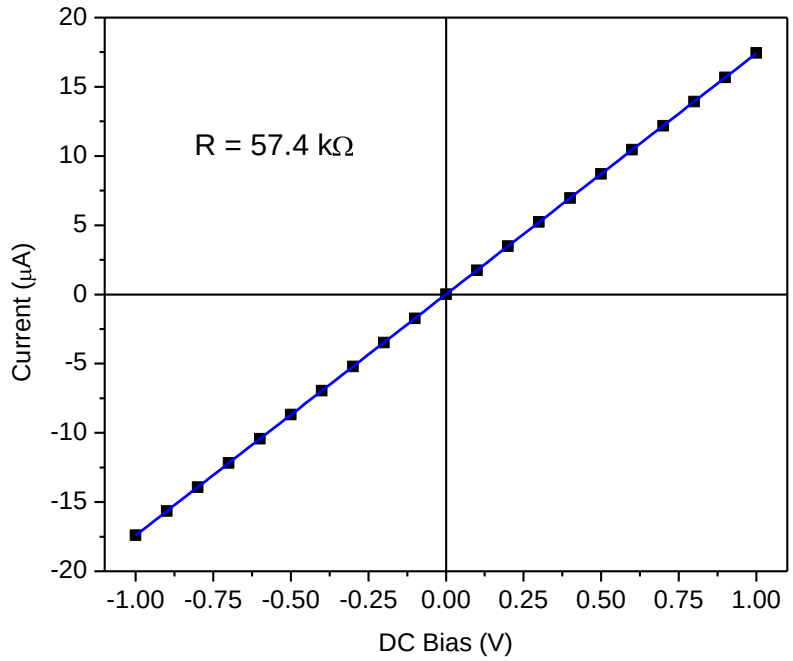

Figure 8. Ohmic resistor behavior shown by one H-graphene bridging two gold pads.

CONCLUSIONS

Different chemical routes are applicable to the synthesis of chemically converted graphene. Different morphologies can be achieved by varying the oxidizing agents and the purification procedure. It has been found that the Hummers' method yielded ~10 μm graphene sheets while the Brodie's method yielded double-layered nanographenes.

The relatively high electrical resistance shown by chemically converted graphene is a great drawback of this procedure and efforts are required to either lower the oxidation degree while maintaining the solubility or enhance the reduction in order to eliminate defects introduced in the oxidation step. Motivation to do so comes from the fact that the solution-processable graphene is the most attractive way to scale-up its production.

ACKNOWLEDGMENTS

This work has been developed during an international exchange program supported by the Institute of Chemistry of the University of Campinas, by the Center for Semiconductor Components of the University of Campinas and by the National Science Foundation (USA). S. A. V. J. thanks Vincent Tung, Adam Stieg and Dr. Yang Yang from the California NanoSystem Institute, at the University of California, Los Angeles for valuable discussions and training.

REFERENCES

[1] Li, D.; Mueler, M. B.; Gilje, S.; Kaner, R. B.; Wallace, G. G., "Processable aqueous dispersions of graphene nanosheets", *Nature Nanotech.*, 3(2), (2008) 101-105.

[2] Castro Neto, A. H.; Guinea, F.; Peres, N. M. R.; Novoselov, K. S.; Geim, A. K., "The electronic properties of gralhene", *Rev. Mod. Phys.*, 81(1), (2009) 109-162.

[3] Berger, C.; Song, Z.; Li, T.; Li, X.; Ogbazghi, A. Y.; Feng, R.; Dai, Z.; Marchenkov, A. N.; Conrad, E. H.; First, P. N.; de Heer, W. A., "Ultrathin Epitaxial Graphite: 2D Electron Gas Properties and a Route toward Graphene-based Nanoelectronics" *J. Phys. Chem. B*, 108(52), (2004) 19912-19916.

[4] Gilje, S.; Han, S.; Wang, M. S.; Wang, K. L.; Kaner, R. B., *Nano Lett.*, 7(11), (2007) 3394-3398.

[5] Tung, V. C.; Allen, M. J.; Yang, Y.; Kaner, R. B.,"High-throughput solution procesing of large-scale graphene", *Nature Nanotech.*, 4(1), (2009) 25-29.

[6] Wang, G.; Yang, Z.; Li, X.; Li, C., "Synthesis of poly(aniline-co-o-anisidine)-intercalated graphite oxide composite by delamination/reassembling method", *Carbon*, 43(12), (2005) 2564-2570.

[7] Li, X.; Zhang, G.; Bai, Z.; Sun, X.; Wang, X.; Wang, E.; Dai, H., "Highly conductiong graphene sheets and Langmuir-Blodgett films", *Nature Nanotech.*, 3(4), (2008) 538-542.

[8] Hummers, W. S.; Offeman, R. E., "Prepatarion of graphitic oxide", *J. Am. Chem. Soc.*, 80(6), (1958) 1339.

[9] Kovtyukhova, N. I.; Ollivier, P. J.; Martin, B. R.; Mallouk, T. E.; Chizhik, S. A.; Buzaneva, E. V.; Gorchinsky, A. D., "Layer-by-layer Assembly of Ultrathin Composite films from Micron-Sized Graphite Oxide Shets and Polycations", *Chem. Mater.*, 11(3), (1999) 771-778.

[10] Brodie, B. C., "Researches on the Atomic Weight of Graphite" *Q. J. Chem. Soc.*, 12 (1860) 261-268.

[11] Szabó, T.; Berkesi, O. ; Forgó, P. ; Josepovtis, K. ; Sanakins, Y.; Petridis, D.; Dékány, I., "Evolution of surface functional groups in a series of progressively oxidized graphite oxides", *Chem. Mater.*, 18(11), (2006) 2740-2749.

[12] Horcas, I., Fernandez, R., Gomez-Rodriguez, J. M., Colchero, J., Gomez-Herrero, J., Baro, A.M., *Review of Scientific Instruments*, 78 (2007) 013705.

[13] Ferrari, A. C.; Meyer, J. C.; Scardaci, V.; Casiraghi, C.; Lazzeri, M.; Mauri, F.; Piscanec, S.; Jiang, D.; Novoselov, K. S.; Roth, S.; Geim, A. K., "Raman spectrum of graphene and graphene layers", *Phys. Rev. Lett.*, 97(18), (2006) 187401.

[14] Novoselov, K. S.; Geim, A. K.; Morozov, S. V.; Jiang, D.; Zhang, Y.; Dubonos, S. V.; Grigorieva, I. V.; Firsov, A. A., "Electric field in atomically thin carbon films", *Science*, 306(5696), (2004) 666-669.

[15] Blake, P.; Hill, E. W.; Castro Neto, A. H.; Novoselov, K. S.; Jiang, D.; Yang, R.; Booth, T. J.; Geim. A. K., "Making graphene visible", *Appl. Phys. Lett.*, 91(6), (2007) 063124.

Smart Nanocomposites
Volume 1, Issue 1.
ISSN: 1949-4823

GAS SENSORS BASED ON MULTIWALL CARBON NANOTUBES DECORATED WITH DIFFERENT METAL OXIDES NANOPARTICLES

A. Abbaspourrad, C. Verissimo, R. V. Gelamo, M. M. da Silva, A. R. Vaz, F. P. M. Rouxinol, O. L. Alves and S. A. Moshkalev
Center for Semiconductor Components,
University of Campinas – UNICAMP, Campinas, SP, Brazil

ABSTRACT

In this work, we present experimental procedures that have been developed to prepare metal oxides nanoparticles for further decoration of CNTs, to gas sensing. We show here, that Sn, Cu and Ti oxides have been attached on the surface of acid treated CNTs. For preparation of carbon nanotubes decorated with SnO_2 and CuO, the concentration of reagents and the time of sonication were found to be crucial parameters to control the size and the amount of nanoparticles attached on the nanotubes surface. In the case of CNTs decorated with TiO_2 decoration, the pH value of the solution plays a key role in the final size of the nanoparticles. According to our results, the control of nanoparticles diameters and distribution on CNTs surface was obtained for an optimum pH value around 2 whereas higher pH values led to fully covered CNTs. The material decorated with SnO_2 were tested with H_2S and changes in the conductivity showed the potential of this material for gas sensing application. The samples were characterized also by HRTEM, SEM and EDS.

INTRODUCTION

Carbon nanotubes (CNTs) exhibit unique electronic properties, high aspect ratio, and excellent chemical and environmental stability, which make them ideal candidates for components of nanodevices. There is a great interest in decorating of CNTs with metal, metal oxide or semiconductor nanoparticles with the exploration of new properties and applications [1-3]. Gas sensors made of carbon nanotubes have been extensively studied [4]. Those fabricated from single-walled carbon nanotubes (SWNTs) have been found to be very sensitive to ambient gas [5]. However, most of them are based on SWNTs field-effect transistors or need UV light irradiation to desorb the detected gas molecules. Furthermore, multiwall carbon nanotubes (MWNTs) are not very sensitive to ambient gas. Recently, as a recent focus of attention in nanotechnology; the oxide semiconductor nanobelts have been

used for highly sensitive gas detection [6]. By decorating MWNTs with various metal oxides we may fabricate a new generation of gas sensing devices with high sensitivity. SnO_2 is an n-type semiconductor oxide with wide band gap energy and is always applied as gas sensing material to detect combustible, toxic and pollutant gases [7]. CuO is a p-type semiconductor and extensively used as gas sensors due to its property, which changes its conductivity under gas exposures. TiO_2 seems to be one of the most interesting candidates for gas detection and has commercially been used as lambda sensor in exhaust pipes [8].

The fundamental mechanism of semiconductor gas sensors relies upon the change in electrical conductivity due to the interaction between semiconducting materials and gas molecules to be detected. When a sensor is exposed to air, oxygen is adsorbed on the surface to form negative ions; the adsorbed oxygen has extracted the conduction electrons from the near-surface region of the metal oxide grains leading to an insulating surface layer. Upon exposure to reductive gas species such as CO, the arrested electrons are released by the reactions between the reductive gas and the negatively charged ions: $CO+O^{-}\rightarrow CO_2+e^{-}$, reducing the steady-state surface oxygen concentration and donating a few electrons back to the bulk resulting in an increased conductivity [9].

In this study, a simple *in situ* chemical hydrolysis method was applied for the synthesis of CuO, TiO_2 and SnO_2-coated MWNTs materials. Metal oxide particles uniformly coated the walls of the MWNTs, and this was found to increase the specific surface area. A gas sensor sample was fabricated from SnO_2-coated MWNTs and the gas-sensing properties were measured in the H_2S and air presence.

EXPERIMENTAL

MWNTs prepared by chemical vapor deposition were purchased from Iljin Nanotech Co., Ltd (Seoul, Korea). Purity of the pristine MWNTs, as received, was 97%. The MWNTs were first heated for 2 h at 330 ºC to eliminate the residual amorphous carbon. The clean nanotubes were refluxed with nitric acid (7 N) for 12 h at 120 ºC. The acid-treated nanotubes were washed with distilled water several times until the pH reached 7 and dried at 80 ºC for 6 h. The acid-treated nanotubes so prepared were used for decorating SnO_2, CuO and TiO_2 using ultrasonic bath and appropriate metal chloride salt.

In a typical synthesis, CuO was prepared by dissolving 130 mg $CuCl_2$ (98%) in 20 mL of distilled water and 5 mg of acid treated MWNTs were dispersed in this solution using ultrasonic bath for 10 min. The mixture was stirred for 12 h and then filtered, dried at 80 ºC for 2 h and calcined at 350 ºC for 24 h.

To prepare SnO_2 decorated MWNTs, 1 g of $SnCl_2$ was dissolved in 40 mL of distilled H_2O and then 1 mL of HCl (38%) was added. Subsequently, 10 mg of the as-treated MWNTs were dispersed in the above solution. This mixture was sonicated for 5 min and then stirred for 90 min at room temperature. The precipitate was then separated from the mother liquor by filtration and was washed with distilled H_2O for several times, and then dried at 80 ºC for 6 h.

In order to decorate MWNTs with TiO_2 nanoparticles, 300 µL HCl and 4 µL $TiCl_4$ (98%) were added to 100 mL distilled water and the mixture stirred for 30 min. Then 3 mg of acid treated MWNTs dissolved in the above solution. The mixture sonicated for 1 min and stirred

for another 30 min by increasing pH up to 2.5 using NH_4OH (1%). The precipitate was filtered and washed several times with distilled water and dried at 80 ºC for 24 h.

In the sensor fabrication, firstly, a decorated MWNTs dispersed solution was prepared by ultrasonic vibrating and then the dispersed solution was dropped between Au and Pd electrodes (fabricated on a SiO_2 wafer) under an ac electric field of 3V at 100 kHz for 2 minutes. The electric measurements of the samples decorated with SnO_2 were made by 2-point probe using HP 4145B Semiconductor Parameter Analyzer. In order to perform electric measurements, samples were placed in a chamber that permits the measurements in vacuum (minimum pressure = $1x10^{-2}$ Torr) or with H_2S and synthetic air flux. The gases were introduced in the chamber by a needle valve coupled in a flow meter. The flows used were 30 sccm to air and 370 sccm to H_2S. The *I x t* curves were obtained using a constant voltage (3V) applied in the metal electrodes.

RESULTS AND DISCUSSION

The morphology, size and electrical properties of CNTs make them an ideal material to use in sensing devices. Decoration of CNTs is of great interest to modify the properties of pristine CNTs for versatile applications. CNTs decorated by metal oxide nanoparticles are a type of novel nanotube/nanoparticle hybrid material for nano devices, which could find promising application as nano sensors. In our metal oxide decoration of MWNTs, we aimed to deposit various nanoparticles on CNTs surfaces with good uniformity; therefore both the specific surface area and the sensing activity can be increased significantly. The good dispersion of CNTs is a crucial requisite for nanoparticle decoration, since it is extremely difficult to disperse the pristine CNTs in common solvents due to their high surface tension. We first conducted a functionalization process to modify the chemical properties of MWNTs by attaching carboxylic acid and hydroxide functional groups to their surface. XPS analysis of functionalized CNTs indicated that up to 20% of carbon atoms on the CNT surface could be oxidized [10]. This functionalization step results in much better CNT dispersion because of the electrostatic repulsion between the functional groups. Furthermore, these functional groups might serve as anchor seeds for the subsequent deposition of metal oxide nanoparticles [10]. Figures 1(a) and (b) show that tin oxide nanoparticles bond on the CNT surface efficiently. The dimension of SnO_2 nanoparticles falls in the range of 1–10 nm with the average value of 4 nm (Figure 1(c) and (d)). It is believed that functional MWNTs play dual roles during nanoparticle deposition. They not only form numerous anchor seeds for nanoparticle deposition on their surface but also form a network with a high surface area preventing the possible agglomeration of the deposited nanoparticles effectively.

SEM micrograph (Figure 2(a)) shows good overall uniformity and dispersion of TiO_2 decorated functionalized carbon nanotubes. Large titanium oxide agglomeration was rarely observed. TEM characterization (Figure 2(b)) showed the formation a crystalline phase for TiO_2.

For CuO, the syntheses led to the formation of very small nanoparticles presenting diameters in the range of 1-3 nm. HRTEM image (Figure 3) also showed the amorphous character for this material.

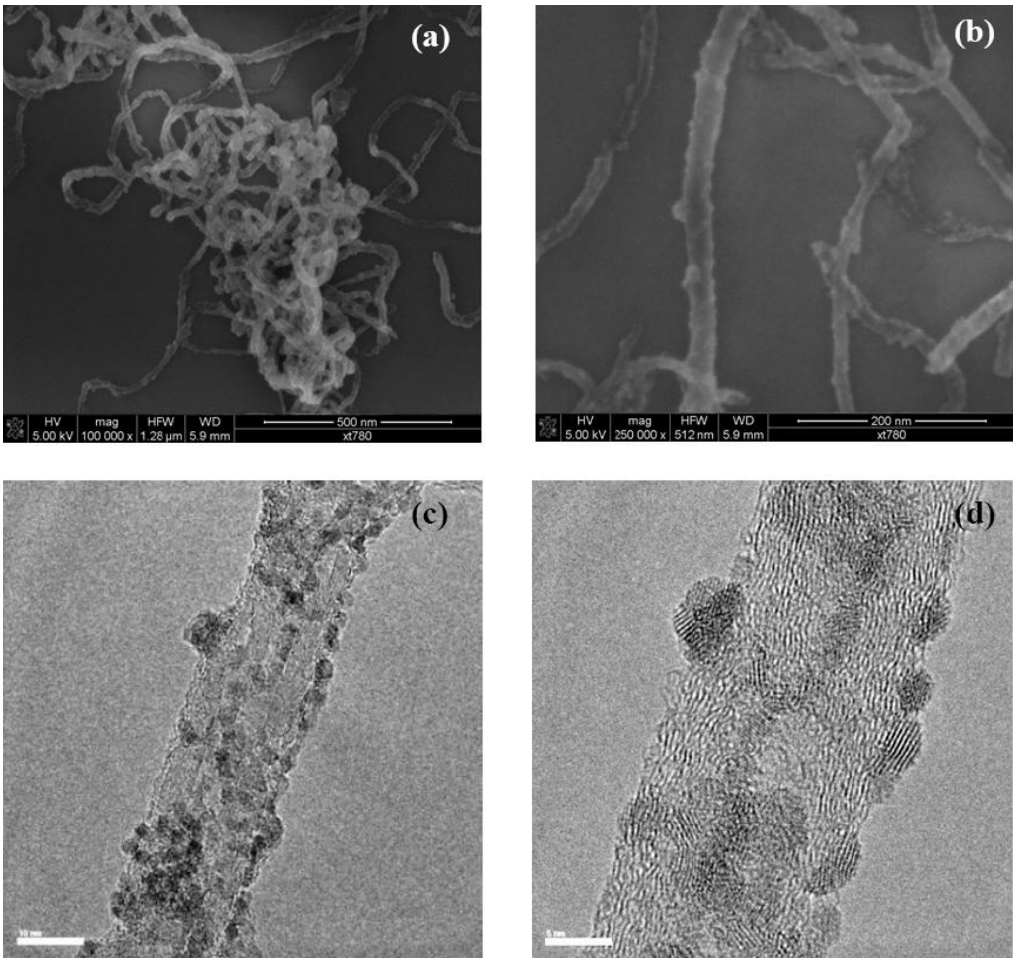

Figure 1. SEM (a, b) and TEM (c, d) images of SnO_2 decorated MWNTs.

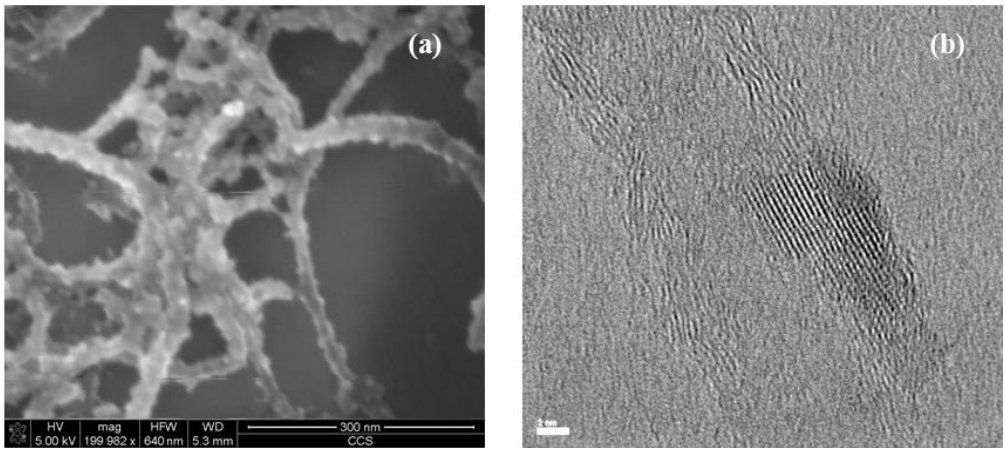

Figure 2. SEM (a) and TEM (b) images of TiO_2 decorated MWNTs.

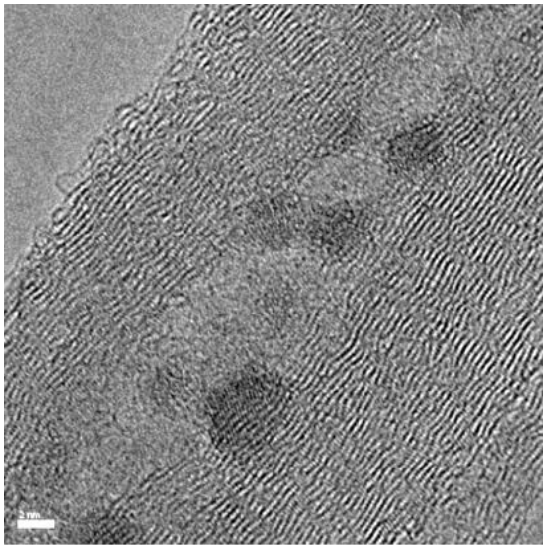

Figure 3. TEM image of CuO decorated MWNT.

Gas sensing device prepared using SnO_2 decorated MWNTs was submitted to the H_2S atmosphere with a constant voltage applied between Pd electrodes. During the test, synthetic air (370 sccm) was kept inside the chamber and H_2S was introduced for 30 seconds and turn-off for 2 minutes at room temperature. When H_2S (30 sccm) was introduced, an increase in the current could be seen. The current dropped back to the original value obtained initially for synthetic air when H_2S flow is stopped, showing the sensor recovery (Figure 4).

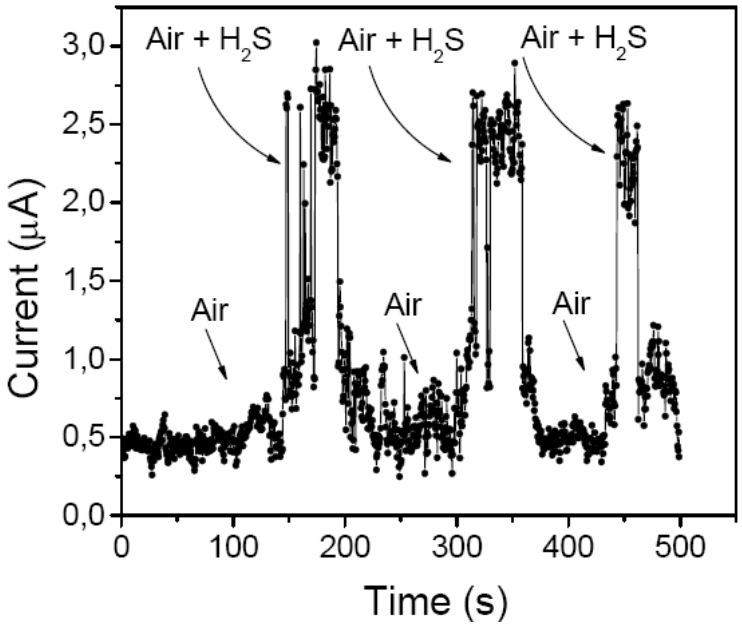

Figure 4. *I x t* curve obtained under air and H_2S atmospheres at room temperature (T = 30°C) using SnO_2 decorated CNTs prototype sensor.

This sensor operation is based on the interaction of H_2S molecules with the SnO_2 nanoparticles removing electrons from the CNTs and changing the conductivity characteristics of this system.

CONCLUSIONS

The development of gas sensor devices based on carbon nanotubes and metal oxide nanoparticles attached on the surface of CNTs walls represents a very promising research area. By choosing appropriate oxides to be associated with carbon nanotubes for the preparation of this class of hybrid materials, it will be possible to fabricate several sensor devices to be employed in different technological applications. According to our experimental data, initial encouraging results were obtained using our prototype gas sensor which was able to operate at room temperature since conventional gas sensors based on metal oxide like SnO_2 are efficient only at relatively high temperatures around 300^oC.

ACKNOWLEDGMENTS

Authors would like to thank CNPq, FAPESP, and NAMITEC for financial support.

REFERENCES

[1] Kong J, Franklin N, Zhou C, Chapline M, Peng S, Cho K and Dai H *Science* 287 (2000) 622–5.
[2] Zhao L P and Gao L *J. Mater. Chem*. 14 (2004) 1001–4.
[3] Sainbury T and Fitzmaurice D, *Chem. Mater*.16 (2004) 3780–90.
[4] Y. M. Wong, W. P. Kang, J. L. Davidson, A. Wisitsora-at, and K. L. Soh, *Sens. Actuators* B 93 (2003) 327.
[5] P. F. Qi, O. Vermesh, M. Grecu, A. Javey, Q. Wang, H. J. Dai, S. Peng, K. J. Cho, *Nano Lett.* 3 (2003) 347.
[6] E. Comini, G. Faglia, G. Sberveglieri, Z. W. Pan, and Z. L. Wang, *Appl. Phys. Lett*. 81 (2002) 1069.
[7] J.F. McAleer, P.T. Moseley, J.O.W. Norris, D.E. Williams, P. Taylor, *Mater. Chem. Phys*. 17 (1987) 577.
[8] Sberveglieri G, Comini E, Faglia G, Atashbar MZ, Wlodarski W *Sensors Actuators* B66 (2000)139.
[9] A. Kolmakov, Y. X. Zhang, G. S. Cheng, and M. Moskovits, *Adv. Mater*. Weinheim, Ger._ 15 (2003) 997.
[10] Xie J, Zhang N and Varadan V J. *Smart Mater. Struct*. 15 (2006) S5–8.
[11] Hyunju Chang et al, *Appl. Phys. Lett*. 79 (23), (2001) 3863 - 3865.

Smart Nanocomposites
Volume 1, Issue 1.
ISSN: 1949-4823

MECHANISM OF MULTI-WALL NANOTUBE NUCLEATION BASED ON MULLINS-SEKERKA INSTABILITY

S. A. Moshkalev [*] ***and C. Veríssimo***
Center for Semiconductor Components – CCS,
State University of Campinas - UNICAMP,
Campinas, SP, CEP 13083-870, Brazil

ABSTRACT

Mechanisms of nucleation and growth of carbon nanotubes and nanofibers in catalytic chemical vapor deposition are analyzed, with the main attention focused on the structural evolution of catalyst particles during the process. Based on experimental observations using high resolution scanning and transmission electron microscopy, a model is developed where the nanotube nucleation is considered as an instability occurring on the catalyst particle surface supersaturated with carbon. The instability, giving rise to the nucleation of tubular graphitic layers, is developed when certain critical conditions (temperature, supersaturation, catalyst volume) are achieved. For lower temperatures, another mechanism of carbon segregation from supersaturated catalyst particles has been observed, when flat rather than tubular graphitic layers are formed. Conditions required for nucleation of nanotubes or nanofibers are formulated.

1. INTRODUCTION

The role of metal catalyst particles and their structural evolution (reshaping) during synthesis of carbon nanotubes (CNTs) by catalytic chemical vapor deposition (CVD) is discussed in many works [1-5], but many important issues still have to be addressed. Note that in most of studies reported so far the mechanisms of nanotubes growth have been considered, while the important step of nucleation attracted less attention and is poorly understood. Strong reshaping of catalyst particles occuring during the nucleation, indicates that considerable energy is released during this stage, and the driving force for this transformation has to be analyzed. In many studies it has been demonstrated that the size of catalyst particles determines the diameter and other properties of the grown CNTs [1,5],

[*] Author to whom correspondence should be addressed. Tel.: +55-19-3521-5213; Fax.: +55-19-3521-5177; E-mail: stanisla@ccs.unicamp.br

however the effect of the particles shape has been studied much less [6-8]. In the process of nanoparticles formation from the film, an interaction with the substrate is important [9,10]. This interaction determines the size and shape of the particle and may affect also its chemical state (through possible catalyst oxidation).

Different substrates have been utilized for CNT synthesis, with SiO_2 and Al_2O_3 being the most popular. The aluminum oxide is usually reported to give better results for both single-wall and mulit-wall nanotubes (SWNT and MWNT, respectively) [1], although the reasons for this are not well clarified. One of the possible effects is stronger catalyst-substrate interaction (better wetting), which promotes formation of smaller particles believed to be more efficient in the synthesis.

A linear correlation between the size of catalyst particles and nanotubes has been reported in many cases, however this correlation is not always direct: saturation of nanotube diameters for bigger particles has been reported [11-13]. Big catalyst particles were found inactive for CNT synthesis, being frequently encapsulated in amorphous carbon or graphitic layers (GL) [14,15]. Note that it cannot be excluded that such encapsulation happened after the growth process. As the microscopy analysis is carried out ex-situ, it is not clear whether the GL encapsulation was the consequence of nucleation failure or nanotube nucleation has not occurred because the carbon supply to the particle was hampered due to eairler GL encapsulation.

The widely accepted model of MWNT formation [1,16] is based on the VLS (vapor-liquid-solid) theory, where the mains steps are: dissolution of carbon atoms in a catalyst, their diffusion through the particle (which can be in a liquid or solid state; in the last case, the mechanism should be called VSS – vapor-solid-solid), followed by precipitation of carbon atoms forming tubular GLs. This model may give reasonable description for the stable growth phase, however the nanotube nucleation and catalyst particle reshaping mechanisms remain basically unclear and need further studies.

In chemical vapor deposition (CVD) experiments, the temperature is usually considerably lower than the catalyst melting temperature T_m. Thus the metal particle is expected to be solid during the synthesis, although it is known that the T_m value can be significantly lowered for small particles saturated with carbon [17-20]. The question of whether the catalyst particle is liquid of solid during nanotubes growth under typical CVD conditions (T<1000° C) is still the subject of discussions [17,21]. This is determined by the difficulty to monitor the particle state *in-situ*, whereas the post-growth observations can give only limited information on the particle behavior during the process. Moreover, particle can suffer reshaping and phase transformations during cooling when the synthesis is stopped. *In-situ* environmental TEM (ETEM) observations by Helveg *et al* performed at a relatively low temperature of 500 °C, indicated that the small Ni particles were crystalline (solid) during the growth process using CH_4/H_2 mixtures [22]. More recently, Hofmann *et al* in similar ETEM experiments [23] using low-pressure NH_3/C_2H_2 gases and temperatures up to 700 °C, have shown that the core of Ni catalyst particle remains crystalline during the continuous process of carbon nanofiber formation. Liquidlike behavior of the catalyst particle (fast self-diffusivity) was invoked in order to explain enhanced particle mobility during process phases when a strong particle reshaping occurs: dewetting from the substrate during the thermal catalyst treatment, and particle elongation followed by its contraction during the nucleation [23].

On the other hand, in experiments of Gorbunov *et al* [18] (see also references therein), apparently molten Ni nanoparticles moving on the surface of amorphous carbon were observed at 700° C. For particles bigger than 100 nm, the lost of mobility and crystallization were observed. Bartsch *et al* [17] studied the growth of multi-wall nanotubes (MWNTs) in a plasma enhanced CVD process using methane and Ni as catalyst (similar results were obtained for Co and Fe) and compared the rates of nanotube growth and carbon diffusion in a solid and liquid Ni. The substrate temperature was varied between 850 and 1100 °C. From temperature dependencies of the growth rate it was concluded that the catalyst particles were solid for lower temperatures (T < 950 °C), when mostly bamboo-like tubes were grown at a low growth rate of ~1 nm/sec. For higher temperatures, longer (growth rate about an order of magnitude higher) and more regular tubular structures were obtained, and the catalyst particles were apparently in a liquid (or liquidlike) state. It is also possible that catalyst particles were only partially liquified as carbon diffusion, to supply the nanotube growth, could occur mostly through the liquid surface layers.

It is important to note that ex situ characterization of carbon nanostructures involves several steps of sample preparation, which may cause serious damages in the material structure, its modification or even disintegration. Normally, the sample preparation for TEM measurements employs ultrasonic bath to take the material off the substrate where it was grown. The effect of the ultrasonication as well as the solvent and surfactants on the structures under study may be significant and undesirable. A promising alternative to the possibly damaging sample transference procedure is to obtain the material directly over TEM grids [24]. In this work, a novel approach is applied to prepare electron-transparent multi-layer membranes (ETMLM), which can be used for growth of carbon nanomaterials directly over TEM grids under typical catalytic thermal chemical vapor deposition conditions. These ETMLM are fabricated by sequential deposition of a thin amorphous carbon film (a structural layer) over a TEM grid, followed by deposition of a thin support layer (different films as SiO_2, Si_xN_y, Al_2O_3, etc. can be used), and finally by deposition of a catalyst metal film. Here, we describe the fabrication of ETMLM using a thin SiO_2 film as support layer for the deposition of metal catalysts, similarly to the conventionally used substrates (thermally oxidized silicon wafers). The main advantage of using carbon amorphous films as structural layers is their compatibility with support layers (oxides or nitrides) during high temperature processing.

Based on results of experimental studies carried out using both conventional and substrates and ETMLMs, a new model of the nucleation of multi-wall carbon nanotubes is developed.

2. EXPERIMENTAL

The n-type (100) silicon wafers covered either by thermally grown silicon oxide layer or amorphous aluminum oxide layer deposited by sputtering (both ~300 nm thick) were used, and electron beam evaporation was employed for deposition of thin Ni or Fe metal films, 6 and 5 nm, respectively. The annealing, to form separate netal nanoparticles, was carried at 700° C. After the annealing, the temperature was raised and synthesis of carbon nanomaterials by CVD method was started by addition of CH_4 for 30 minutes. High

resolution scanning electron microscopes FEG-SEM JSM-6330F - JEOL and Nova 200 Nanolab - FEI Co. were used for structural analysis of samples. High resolution transmission electron microscopy (HR-TEM) was performed using HRTEM-JEM 3010 URP - JEOL. In order to study the process of nucleation, some experiments were realized on specially prepared TEM grids. The grids were sequentially covered by thin layers of amorphous carbon (a structural layer), SiO_2 and Ni catalyst. After that, conventional annealing and short (5 min) growth processes were carried out. This procedure allows to avoid the process of a sample transfer to a TEM grid, which is known to be highly damaging, and to obtain high quality TEM images of nanotubes soon after their nucleation, under the same conditions that those used for normal growth.

3. RESULTS AND DISCUSSION

Figures 1a,b show typical SEM images of Ni catalyst particles (sized from 10 to 100 nm in diameter, and from 10 to 40 nm in height) before the growth in experiments were no methane was admitted to the chamber. Images taken after growth in methane-hydrogen mixture usually demonstrate tip-growth mechanism with catalyst particles visible at the top of nanotubes (Figure 2 a). Note also that distribution of nanotube diameters is relatively narrow (20-60 nm), compared with that for nanoparticles before the growth. However, for shorter growth times it is possible to find Ni particles also at the bottom or inside the nanotube (Figure 2b), clearly indicating that Ni particles partly or completely flew inside the tubes during the nucleation.

It is important to emphasize that low rates of nanotubes growth obtained here (20-50 nm/min), comparable with those obtained under similar temperature conditions [17], strongly indicate that the catalyst particles were predominantly in a solid rather than liquid state during the stable phase of the growth. The lowering of T_m for Ni-C solution at the eutectic point is relatively small (110 °C).

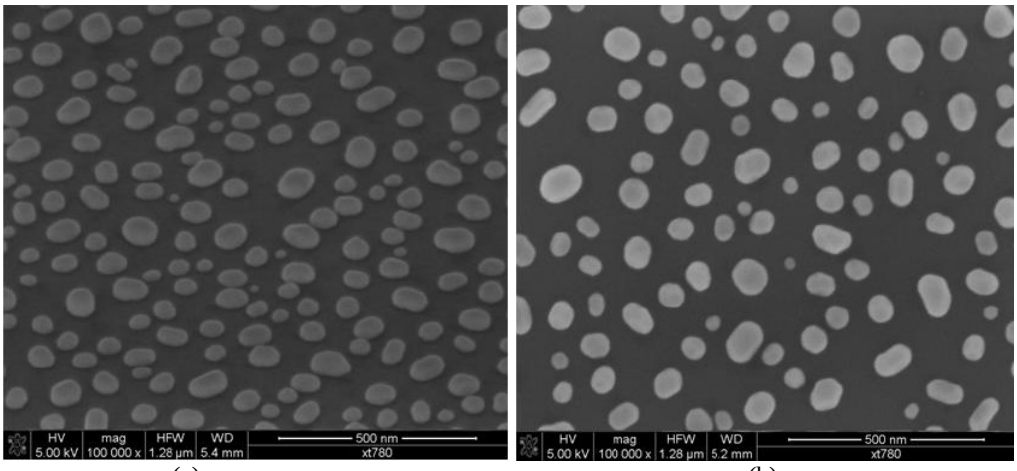

(a) (b)

Figure 1. SEM images of Ni particles after annealing, 700°C; tilt 0° (a) and 56° (b), 30', SiO_2.

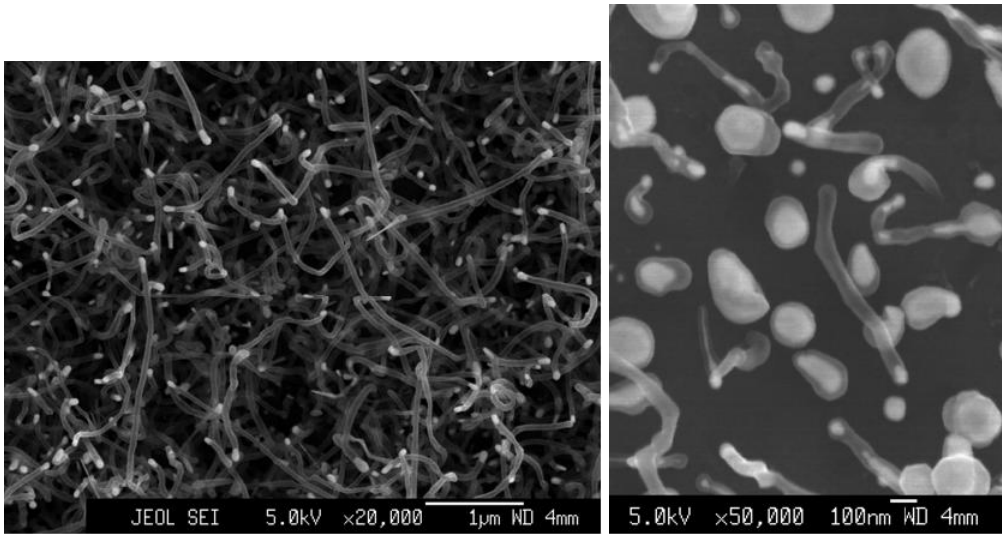

(a) (b)

Figure 2. SEM images after growth, Ni, SiO_2 , 900°C, 30' (a) and 5'(b).

For particles smaller than 100 nm T_m can be further reduced [19,20]. However, strong decrease of T_m (~200 °C) is possible only for very small Ni particles (<10 nm in diam.). Thus bigger particles, even saturated with carbon, should be solid at T< 1000 °C. Moreover, the nucleation occurs usually in the particle central part, expected to be relatively flat. Then apparent partial melting of bigger Ni particles during nanotubes nucleation cannot be attributed directly to curvature-dependent effects.

Further support for the hypothesis of Ni catalyst partial melting during initial stage of the nanotube growth was obtained here in short growth (5 min.) experiments with specially prepared TEM grids, which had the same structure of upper layers: a thin Ni film supported on the SiO_2 layer. Figures 3 show that the catalyst particle elongation and partition, under the present conditions, occurs in a way apparently different from that observed for lower process temperatures and smaller particles [22,23]. Catalyst particles can be seen partly ejected into the nanotubes, forming long (up to 200 nm) protrusions that can be eventually broken in smaller parts. High mobility of the metal catalyst, during the nucleation phase, is evident.

The observed phenomena can be explained considering micro-energetics of the process. Formation of a graphitic layer from C atoms dissolved in a catalyst is an exothermic process [19,24,25]. Experimental evidence of a considerable energy release during catalytic graphitization of amorphous carbon resulting in transition of Fe catalyst nanoparticles into liquid state at a temperature as low as 640° C was reported in Ref. 26. A novel mechanism of MWNT nucleation for the Ni/CH_4 case can now be considered (Figure 4). As methane dissociates on the Ni surface (Figure 4a), carbon starts to accumulate in the particle, with the carbon concentration [C] always higher in the surface layer. When [C] approaches to supersaturation, mobility of the quasi-liquid surface layer increases, so that a flat particle surface becomes unstable and small surface perturbations can occur (Figure 4b). The mechanism of this perturbation in supersaturated metals was first analysed by Mullins and Sekerka [27]. It was shown that the surface became unstable if the radius of perturbation exceeded a critical value, which is reduced with increasing supersaturation.

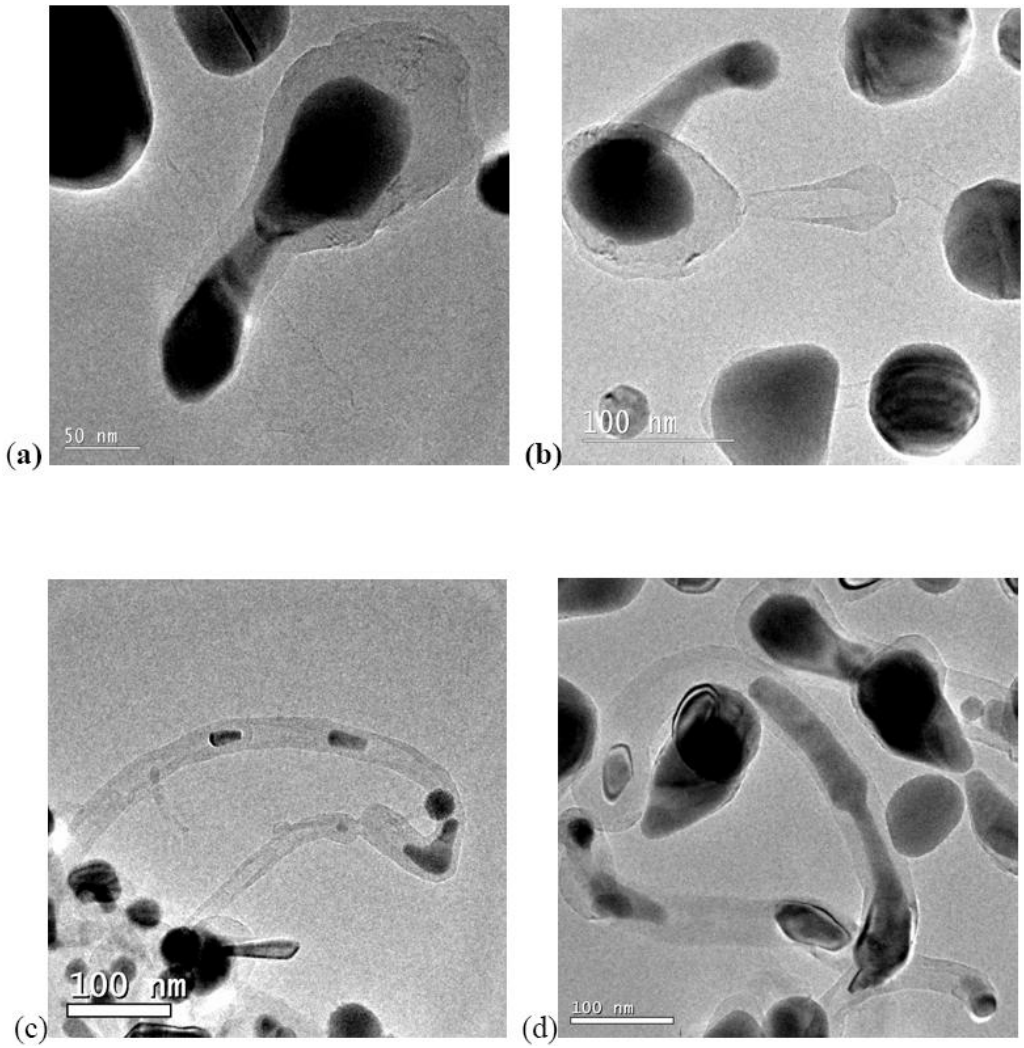

Figure 3. TEM images after growth, 950°C (b), CH_4/H_2=2:1, 5'.

The driving force for the instability is the concentration gradient of the solute. Smaller perturbations are stabilized by the surface tension which tends to reduce the surface area. In other words, these deviations from the flat surface are reversible until the [C] value is under the critical level, but its further increase can start an irreversible process.

Carbon solubility in metals is known to depend on the surface curvature, being the maximum for protrusions (i.e., under convex surfaces), intermediate for flat surfaces and minimum for valleys (negative curvature) [20]. Therefore, when a local surface perturbation (a protrusion surrounded by a circular valley) is formed, carbon atoms may start to precipitate at the bottom around the protrusion, where the [C] value turns out to be above the critical supersaturation level (Figure 4c). The following steps constitute the scenario of a specific surface instability resulting in a nanotube nucleation [13]:

1) At a high enough temperature, the carbon precipitation may form tubular graphitic layers (energetically favorable process) around the protrusion (Figure 4c).

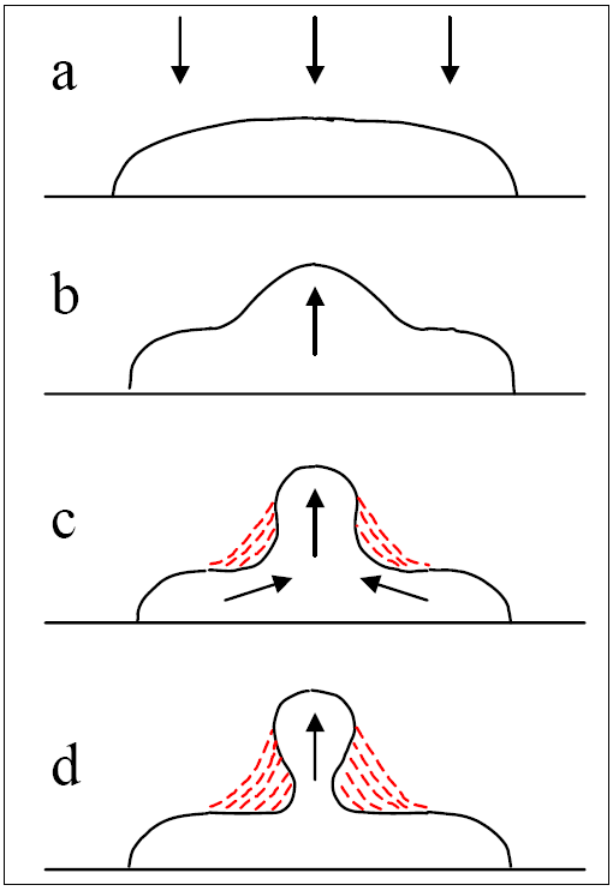

Figure 4. Model of nanotube nucleation. Arrows show flow of carbon (outside and inside the particle).

2) This leads to local heating of the metal in contact with the emerging structure and enhances carbon diffusion in the surrounding area. 3) Since the [C] value in this area is reduced after the initial precipitation, a strong concentration gradient is formed which accelerates the carbon influx from adjacent regions. 4) New portions of C atoms coming to the precipitation site from outer parts of the particle contribute to the further growth of the tube, releasing more heat, and so on. Note that carbon atoms are in interstitial positions in nickel, and their segregation from the catalyst particle results in considerable increase of the total volume of a carbon/metal system, as compared with the case of a carbon-metal solution. Therefore, formation of graphitic layers around the growing protrusion may result in its squeezing near the bottom (where the the surface curvature is negative and carbon solubility is minimum), formation of a narrow neck, and finally, partition of the particle (Figure 4d). The nucleation process can be successful, if the particle ejected to the tip of a nanotube, is small enough to provide fast diffusion of carbon through it. In the case of slow diffusion (big particle, low process temperature), the nanotube growth will stop because of excessive deposition of carbon on the front face of the catalyst particle and, eventually, its encapsulation. If the initial particle is small enough, its partition does not occur, and the whole particle can be ejected to the tip of a growing nanotube.

Further, the process of carbon graphitization leads to a strong local overheating of the particle [28]. Assuming that: (i) carbon atoms corresponding to 10 at. % of Ni-C solution form graphitic layers, (ii) the energy released in graphitization from a Ni-C solution is 0.5 eV per C atom [25], (iii) the energy release is instantaneous (thus neglecting heat dissipation), a simple estimate for the temperature rise gives ΔT exceeding 150 K. The molar heat capacity c_p(Ni) = 26 J/mol K was used. Heat dissipation due to radiation and heat conduction will result in somewhat lower ΔT. On the other hand, the initial carbon content can be much higher than 10at.%. Thus the local overheating can be strong enough to promote at least partial metal melting and a "pulsed" segregation/extrusion of carbon, accumulated in the particle during the incubation period. The catalyst area from which carbon is extracted during nucleation is limited by diffusion. If the particle diameter exceeds 0.2-0.3 μm, formation of a number of multi-walled nanotubes (i.e., nucleation sites) from a single metal particle [29]. This shows that the nucleation process involves carbon accumulated in and extracted from a certain volume of the catalyst. It is important that the metal heating due to graphitic layers deposition becomes much weaker for the stationary phase of growth (due to radiation losses and reduced carbon supply occuring now through a small area of the front particle surface, Figure 4d), as compared with the pulsed heat release during the nucleation process. This can result in significant slowing down of the nanotube growth rate soon after nucleation [17].

In separate experiments, the carbon precursor gas CH_4 was admitted in the chamber for a short time (1-1.5 min.), which is slightly shorter than that required for nanotubes nucleation (in this case, 2 min.), at 950° C. Then, the samples were cooled down in H_2 atmosphere in aproximately 30 min. It can be expected that carbon dissolved in the particles (at a nearly critical level of supersaturation), will be segregated during the cooling stage at a somewhat lower (by 100-200° C) temperature. Instead of a normal nanotube nucleation at the particle top, in this case multiple nucleation "petals"-like sites along the particle circumference can be seen for big catalyst particles (Figure 5a) [28]. Tilted SEM images (Figure 5b) reveal that carbon segregation occurs at the particle bottom (probably, the area of the highest curvature corresponding to the highest solubility of carbon just before the segregation). Along with graphitic carbon, some amount of probably amorphous carbon can be also seen in Figure 5b at the bottom of nanoparticles. TEM images of similar samples obtained in specially prepared multilayer TEM grids reveal that carbon segregation occurs in a way very much different from a normal nucleation process, with graphitic layers being parallel to the metal surface (Figure 6) [28]. For longer exposure time, i.e., at higher carbon concentration, the volume of each graphitic "petal" is bigger (as expected), and the number of nucleation sites for particles of the same size tends to be smaller, as compared with the case of shorter exposure (not shown). The number of sites decreases fast with the particle diameter. For smaller particles (with diameters < 50 nm) single tubules can be seen (Figure 5a). The fact that under the present conditions, carbon segregation and graphitization do not occur uniformly around the particles, indicates the development of another kind of surface instability, with a characteristic period in the range of 30-50 nm. In contrast to the "global" MS-type instability where the whole particle is involved in a nucleation of nanotube, this is a smaller scale or "local" instability. In the global instability, the volume of dissolved carbon that participate in the process and the energy released in graphitization are much greater making possible the particle reshaping.

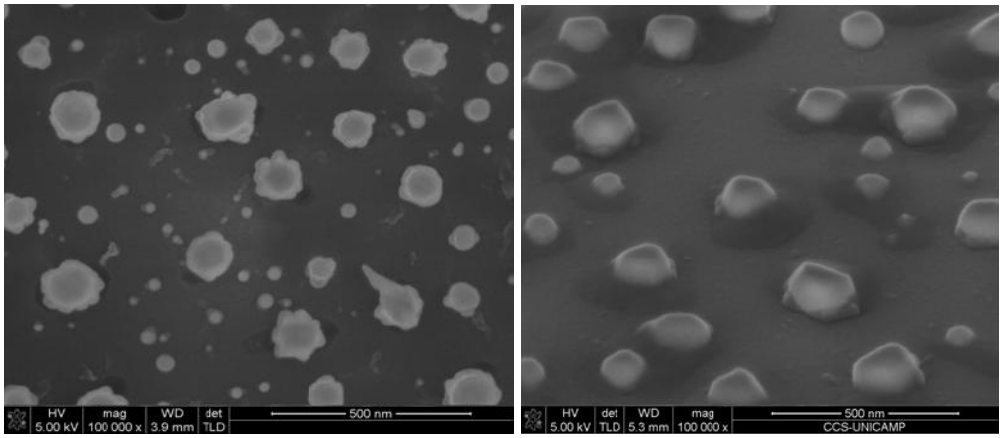

(a) (b)

Figure 5. SEM images after short exposure to CH_4, 900°C , tilt 0° (a) and 56° (b), 1.5', Ni; SiO_2.

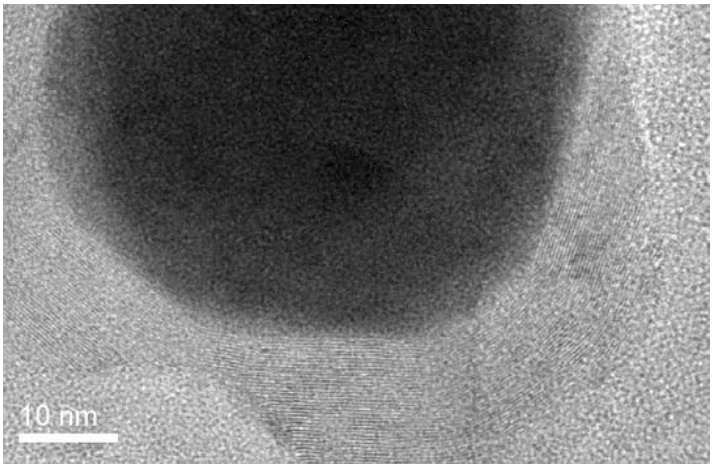

Figure 6. TEM image after short exposure to CH_4, 900°C , Ni; 1.5' , SiO_2.

The global mechanism does not work in this case probably as the ambient temperature at the moment when segregation starts, is reduced (and so, the diffusion of carbon and the particle mobility), so that the MS instability (formation of a protrusion) cannot be developed. In the local instability, smaller regions of the supersaturated catalyst particle are involved, less energy is released and significant particle reshaping does not occur. Nevertheless, considerable effect of the local heating due to graphitization must be invoked, as otherwise uniform carbon deposition around the particle should be expected. Interestingly, in Figure 5a it can be seen, that some particles start to form bigger filaments/protrusions, in a process that apparently involves bigger particle fractions, at the expence of neigbouring nucleation sites. This is a direct indication that before the cooling the particle was very close to the supersaturation level necessary for nucleation of nanotube in a global mechanism.

Some estimates of the process characteristic times can be now made. Supposing that the carbon segregation for the case shown in Figure 5a occurred at a relatively high temperature (800-850°C), with the corresponding carbon diffusion coefficient in Ni estimated as $D \sim 10^{-11}$

m^2/s [17,30], we can evaluate the minimum time necessary for carbon diffusion to the precipitation site. Using the relation $\tau = \lambda^2/4D$ between the characteristic diffusion time τ and length λ (λ ~30 nm), the estimate can be done for $\tau \sim 10^{-5}$ s. As graphitization is much faster process (it has a nanosecond scale) [30,31], this estimate gives the time scale for the development of a local instability.

For nanotube nucleation at 900-950°C, the diffusion coefficient must be about an order of magnitude higher, however the diffusion length (the region involved in the global instability) also may be bigger, up to 100 nm. Then, the time scale for MWNT formation through the MS-type mechanism can be estimated in the range of 10^{-6}-10^{-5} s.

Another important question is related to the problem of heat dissipation. The characteristic time for this process is difficult to estimate for nanostructured materials [32]. In the case of instantaneous heat release, the temperature decay $\Delta T(t)/T_0$ with time *t* due to heat redistribution is determined basically by the term proportional to $\mathrm{erf}[-x/\sqrt{(4\alpha t)}]$, where erf is the error function and α is the thermal diffusivity. The heat redistribution is known to be very fast for solid metals, but can be significantly reduced for alloys and liquid metals, and is much smaller for insulators like SiO_2. Rough estimates of times required to reach $\Delta T(t)/T_0 \approx 0.05$ in a process of heat dissipation through 20 -50 nm layer of solid crystalline Ni and 100 nm of underlying SiO_2 layer give values of 10^{-9} - 10^{-8} and 10^{-6} s, respectively. This means that characteristic time of heat dissipation through the oxide layer may be comparable with the time required for nanotube nucleation, determined basically by carbon diffusion in a catalyst particle. Considering also that: (i) the directions of heat flux and carbon diffusion in the particle are opposite and (ii) the catalyst particle is saturated with carbon, the time of heat dissipation in the catalyst particle may be considerably higher than the estimated above values in the range of 10^{-9} - 10^{-8} s.

Finally, we can now formulate, in more general terms, the critical parameters that determine the result of a nucleation process (nanotube or nanofiber) under supersaturation conditions in metal-carbon (Me-C) nanoparticle:

(a) high self-diffusivity (mobility) of Me-C solution (depends on the temperature and carbon density) is required for development of Mullins-Sererka instability, forming a "template" for formation of a *tubular* structure;
(b) high diffusion coefficient (*D*) of carbon in a metal (depends on the temperature and Me-C interaction) is required for pulsed graphitization starting formation of a nanotube;
(c) high energy released during carbon segregation and graphitization, in the case of Ni/C this energy is as high as 0.5 eV per C atom. If conditions a-c) are not fulfilled, formation of nanofibers rather than nanotubes should happen.

The highest *D* values are reported for carbon in metals like Ni and Fe. It is interesting to note that in the case of silicon nanowires formation using Au catalyst [33], the *D* values are indeed several orders of magnitude smaller than those for the Ni-C case, under the process temperatures.

CONCLUSIONS

The work presents the results of a study of multi-wall carbon nanotubes nucleation and growth in thermal CVD using methane and nickel catalyst, at atmospheric pressure and temperatures of 800-950° C. Experimental evidences have been obtained to reveal the crucial role of additional catalyst heating (up to 100 K or more) occurring due to energy released in fast graphitization during the nucleation phase. This pulsed heating can explain the liquidlike state (enhanced mobility and diffusivity) of the catalyst particle, apparently formed under the present conditions when the nanotube starts to grow. The nucleation from a big catalyst particle is considered here as a specific surface instability with the initial step described by the well-known Mullins-Sekerka mechanism (impurity segregation from metals under critical supersaturation conditions). The proposed model of nanotube nucleation can be called VSLS (vapor-solid-liquid-solid), in contrast to the VLS model, emphasizing that the catalyst may be found in a mixed solid-liquid (or liquidlike) state during nucleation and unstable phases of nanotubes growth.

ACKNOWLEDGMENTS

The work was supported by CNPq, NAMITEC, FAPESP and FINEP. The electron microscopy work was performed with FEG-SEM JSM-6330F and HRTEM-JEM 3010 URP microscopes, LME/LNLS, Campinas, Brazil.

REFERENCES

[1] A.-C. Dupuis, *Prog. Mat. Sci.* 50 (2005), 929.
[2] A. Moisala, A. G. Nasibulin, and E. I. Kauppinen, *J. Phys.: Condens.Matter* 15 (2003), S3011.
[3] P. J. F. Harris, *Carbon* 45 (2007), 229.
[4] G. G. Tibbetts, *J. Cryst. Growth* 66 (1984), 632.
[5] S. A. Moshkalyov, A. Moreau, H. Guttiérrez, M. A. Cotta, and J. W. Swart, *Mater. Sci. Eng. B* 112 (2004), 147.
[6] R. Seidel, G. S. Duesberg, E. Unger, A. P. Graham, M. Liebau, and F. Kreupl, *J. Phys. Chem. B* 108 (2004), 1888.
[7] M. Chhowalla, K. B. K. Teo, C. Ducati, N. L. Rupesinghe, G. A. J. Amaratunga,C. Ferrari, D. Roy, J. Robertson, and W. I. Milne, *J. Appl. Phys.* 90, (2001) 5308.
[8] A.C. Wright, Y. Xiong, N. Maung, S.J. Eichhorn, R.J. Young, *J. Mater. Sci. Eng. C* 23 (2003), 279.
[9] R. L. V. Wal, T. M. Ticich, and V. E. Curtis, *Carbon* 39 (2001), 2277.
[10] T. de los Arcos, M. G. Garnier, P. Oelhafen, D. Mathys, J. W. Seo, C. Domingo, J. V. Garcia-Ramos and S. Sánchez-Cortés, *Carbon* 42, (2004) 187.
[11] E. F. Kukovitsky, S. G. L'vov, N. A. Sainov, V. A. Shustov, and L. A. Chernozatonskii, *Chem. Phys. Lett*. 355 (2002), 497.

[12] A. R. Harutyunyan, T. Tokune, E. Mora, J.-W. Yoo, and A. J. Epstein, *J. Appl. Phys*. 100 (2006), 044321.
[13] S. A. Moshkalev, C. Verissimo, *J. Appl. Phys*. 102 (2007) 044303.
[14] F. Ding, A. Rosén, K. Bolton, *Chem. Phys. Lett*. 393 (2004), 309.
[15] Dai H, Rinzler AG, Nikolaev P, Thess A, Colbert DT, Smalley RE., *Chem Phys Lett*. 260, (1996) 471.
[16] R. T. K. Baker, *Carbon* 27, (1989), 315.
[17] K. Bartsch, K. Biedermann, T. Gemming, A.J. Leonhardt, *J. Appl. Phys*. 97 (2005) 114301.
[18] A. Gorbunov, O. Jost, W. Pompe, A. Graff, *Carbon* 40 (2002) 113.
[19] O.A. Louchev, T. Laude, Y. Sato, H. J. Kanda, *J. Chem. Phys.* 118 (2003) 7622.
[20] A. G. Nasibulin, P. Queipo, S. D. Nasibulin, D. P. Brown, H. Jiang, P. V. Pikhitsa, O. V. Tolochko, E. I. Kauppinen, *J. Nanosce. Nanotechnol*. 6 (2006) 1233-45.
[21] A. Gorbunov, O. Jost, W. Pompe, A. Graff, *Appl. Surf. Sci*. 197-198 (2002) 563.
[22] S. Helveg, C. Lopez-Cartes, J. Sehested, P.L. Hansen, B.S. Clausen, J.R. Rostrup-Nielsen, F. Abild-Pedersen, J.K. Norskov, *Nature* 427(2004) 426.
[23] S. Hofmann, R. Sharma, C. Ducati, G. Du, C. Mattevi, et al, Nano Lett. 7 (2007) 602.
[24] R.E. Smalley, B.I. Yakobson, *Sol. State Comm*. 107 (1998) 597.
[25] M. Eizenberg, J.M. Blakely, *Surf. Sci*. 82 (1979) 228.
[26] O.P. Krivoruchko, A.N. Shmakov, V.I. Zaikovskii, *Nucl. Instr. Methods Phys. Res*. A 470 (2001) 198.
[27] W.W. Mullins, R.F. Sekerka, Morphological stability of a particle growing by diffusion or heat flow, *J. Appl. Phys*. 34 (1963) 323.
[28] C.Verissimo, M.R. Aguiar, S.A. Moshkalev, *J. Nanosci. Nanotechnol*., 9, 6, 4459-4466, 2009.
[29] M.S. Wong, K.W. Cheng, C.H. Shee, Y.R. Ma, J.C. Wu, Y. Liou, Y.D. Yao, *J. Appl. Phys.* 95 (2004) 7291.
[30] A. G. Nasibulin, P. Queipo, S. D. Shandakov, D. P. Brown,H. Jiang, P. V. Pikhitsa, O. V. Tolochko, and E. I. Kauppinen, *J. Nanosci. Nanotechnol*. 6, 1 (2006).
[31] F. Ding and K. Bolton, *Nanotechnology* 17, 543 (2006)
[32] Zh. M. Zhang, *Nano/microscale heat transfer*. McGrow Hill, New York (2007).
[33] S. Hofmann, R. Sharma, C. T. Wirth, F. Cervantes-Sodi, C. Ducati, T. Kasama, R. E. Dunin-Borkowski, J. Drucker, P. Bennett and J. Robertson, *Nature Mater*. 7, 372 (2008).

Smart Nanocomposites
Volume 1, Issue 1.
ISSN: 1949-4823

SELF ASSEMBLY OF SILICON NANOISLANDS ON CRYSTALLINE SILICON UNDER A PHOTOACTIVE LAYER

Ragnar Kiebach*[a], Mariano Aceves-Mijares[a], Zhenrui Yu[a], Karim Monfil[a], Jacobus Willibrordus Swart[b] and Guilherme Osvaldo Dias[b]

[a]INAOE, Departments of Electronics, Apdo. 51, Puebla, Pue. 72000, México
[b]Center for Semiconductor Components, State University of Campinas, Campinas – São Paulo – Brazil

ABSTRACT

Silicon Rich Oxide (SRO) is an interesting candidate for optoelectronic devices due to its light emitting properties, but until now it was not possible to combine silicon nano structures, as connecting part between the substrate and the deposited film, with the existence of photoluminescence (PL). In this work, a multi-layer approach was used to combine the structural and electrical properties of high silicon content SRO with the optical properties of low silicon content SRO. The formation of silicon nano islands (Si nIs) in the silicon rich layer can be controlled by the stoichiometry and thickness. Additionally, the optical properties of the second layer can be optimized independently from the first layer. The samples were synthesized by low pressure chemical vapor deposition (LPCVD) and characterized by transmission electron microscopy (TEM), PL measurements and Rutherford backscattering spectroscopy (RBS).

Keywords: Si nano crystal, nanostructured materials, luminescence, silicon rich oxide, RBS spectroscopy, TEM.

1. INTRODUCTION

The development of nano sized structures is crucial for micro electronics future progress. In the last decade, a large number of publications dealing with all types of III-V, IV and II-VI

* Corresponding author: rkie@inaoep.mx, Tel: +52 (222) 266-31-00, Fax:+52 (222) 247-05-17, INAOE, Apdo. 51, Puebla, Pue. 72000, México

semiconductor nano materials has been released [1-5]. The main focus is on the development of Si based nano structures since they are compatible with state of the art silicon technology [6]. To obtain regular arrays of silicon nano particles with quantum effects at room temperature sizes of less then 10 nm are necessary [7], and even for new approaches like high resolution lithography this is a challenge [8].

Self-organization is one promising fabrication method to produce structures with the dimensions needed for applications, such as Si quantum dots [9] or quantum wires [10]. Self-assembled nanostructured materials offer a number of advantages over conventional technologies in a wide range of sectors.

We already reported [11] that Si nanoislands (nIs) can be synthesized by self assembly of Si during the annealing process of SRO. SRO is a multiphase material which consists of SiO_2, Si and SiO_x [12]. An easy way to obtain SRO is LPCVD, a method which is compatible with IC technology. Besides the interesting structural features like Si nIs and silicon nano crystals (Si nCs), SRO have remarkable electronic and optical properties, such as charge trapping [13], negative differential conductivities (NDC) at room temperature [14], the emission of visible light under UV illumination (photoluminescence) [15] and a tunable optical band gap [16]. While the presence of Si nC is crucial for the charge trapping and NDC, high amount of Si nC extinguishes the PL [15]. For the design of optoelectronic nano devices, it is necessary to combine all of theses properties in one material.

In this paper, we report the presence of regular silicon nano structures and high PL in the same sample. To do so, a multi-layer approach was used. First, a thin layer with high silicon content was deposited in order to get Si nano structures, followed by a thick layer with a low silicon excess in order to obtain high PL. This structure allows the self assembly of Si nIs at the Si/SRO interface and simultaneously high luminescence in the top layer. In addition, the samples were characterized by TEM, RBS and PL measurements.

The Si nIs in the bottom can be used to fabricate nano scaled electronic devices (such as transistors), while the top layer can be used to prepare optical components.

2. EXPERIMENTAL

Sample Preparation

SRO layers were deposited on c-Si (100) substrates using LPCVD. Silane (SiH_4) and nitrous oxide (N_2O) were used as the reactive gases, and the partial pressures ratio (Ro = P_{N2O}/P_{SiH4}) of 5, 20 and 30 were used to obtain layers with a stoichiometry of $SiO_{1.25,}$ $SiO_{1.65,}$ $SiO_{1.72}$, respectively. A hot wall reactor was used as a reaction vessel and the pressure was controlled by mass flow controllers and a Baratron pressure sensor. The substrate temperature during the deposition was 700 $^{\circ}$C. Two different sets of samples with a double layer structure were synthesized. For the first sample (S1), a thin (70 nm) SRO layer with $SiO_{1.25}$ was deposited first, followed by the deposition of the second SRO layer with $SiO_{1.65}$ (650 nm). The second sample (S2) contains a $SiO_{1.25}$ layer (8 nm), followed by a $SiO_{1.72}$ layer (70 nm). The samples S1 and S2 were annealed at 1100 °C in N_2 for 120 and 180 min, respectively.

TEM

A HRTEM Tencai F30 operated with an acceleration voltage of 300 kV and a line resolution of 0.2 nm was used to characterize the samples microstructure in a cross-section view.

Photoluminescence

PL was carried out with a Perkin Elmer luminescence spectrometer model LS50B at room temperature. The samples were excited using a 300 nm radiation. PL emission was scanned between 400 and 900 nm (3.1–1.37 eV) with a resolution of 2.5 nm.

Rutherford Back Scattering (RBS)

A beam of 2.2 MeV He^{+} ions from a 5SDH Pelletron-Tandem electrostatic accelerator was used for the RBS analysis of the silicon and oxygen content in our double layers SRO deposited samples, annealed at 1100°C. The energy of the scattered He^{2+} ions was measured with the detector positioned at a 120° backscattering angle.

3. RESULTS AND DISCUSSION

Figure 1 presents the electron diffraction pattern and the cross-section TEM images of S1. In the pictures with low resolution (Figure 1B and Figure 1C) the two different layers are clearly observable. The thicknesses of the layers are 70 nm for the $SiO_{1.25}$ layer and 650 nm for the $SiO_{1.65}$ layer, respectively. In the $SiO_{1.25}$ layer, a high density of silicon nano structures is found. Two different kinds of Si nano structures are observed: Si nIs at the boundary Si-substrate/$SiO_{1.25}$ (Figure. 1B and Figure 1D) and Si nCs within the SiO_2 matrix of the $SiO_{1.25}$ layer. The distribution and the shape of the Si nIs are irregular. While the width of the Si nIs seems to have a constant value around 10 nm, significant variations in the height between 4 nm and 15 nm are found (Figure 1D). Besides the Si nIs, a large number of crystalline Si agglomerates in the $SiO_{1.25}$ layer is found. The shape and size of these Si nCs differs strongly (Figure 1D), also the crystalline orientation varies compared with the Si nIs, which grows epitaxial on the substrate. In the corresponding diffraction pattern (Figure 1A), the bright spots in the upper right corner are a weak indication of the crystallinity of the Si nano structures. To achieve a more regular distribution in size and shape of the Si nano structures, layer thicknesses and the stoichiometry for S2 were changed. The thickness of both layers was reduces by a factor of 10 (8 nm for the $SiO_{1.25}$ bottom layer and ~ 70 nm for the $SiO_{1.72}$ top layer). Since the $SiO_{1.25}$ layer contains a sufficient amount of excess Si for the formation of the desired nano structures, the Si content was kept constant. However, the stoichiometry for the top layer was changed to $SiO_{1.72}$, reducing the amount of excess Si. The higher difference in the Si excess between the two layers leads to a sharp interface between the two layers after the diffusion produced by the annealing.

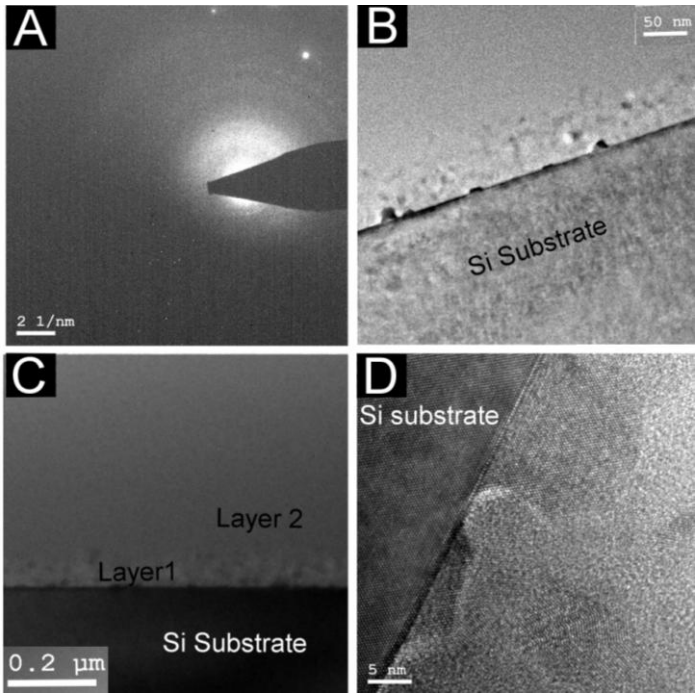

Figure 1. Electron diffraction pattern (A) and cross-section TEM images of S1 after thermal annealing, where (B) and (C) were taken with low resolution, while (D) was taken with higher resolution.

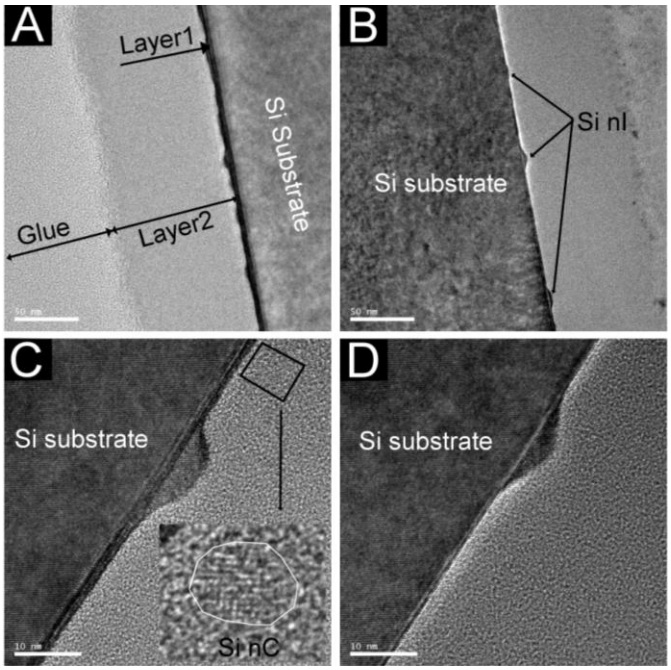

Figure 2. Cross-section TEM images of S2 after thermal annealing, where (A) and (B) were taken with low resolution, while (C) and (D) were taken with higher resolution.

In Figure 2 the cross section TEM images of S2 are shown. After the annealing the majority of the excess Si is found near to the substrate. The slightly undulated layer of $SiO_{1.25}$ grown on the substrate is observable in Figure 2A. Also a regular array of Si nIs is found (Figure 2A and Figure 2B). Please note that the contrast in the middle of the image is due to the sample preparation and corresponds to the interface of the $SiO_{1.72}$/glue.

In Figure 2C and 2D (high resolution) single Si nIs are shown. The shape of these islands is uniform, the width of 10 nm is identical with the one in S1, but no big variation in the height (~ 4 nm) is found. The amount of Si nCs in S2 is significantly reduced, and only small agglomerates can be observed in the SiO_2 matrix (inlet in Figure 2C).

To obtain the stoichiometry of the each layer, the samples were characterized by RBS. In Figure 3, the RBS spectra and the corresponding fit for S1 is presented. A Si:O ratio of $SiO_{1.25}$ for the first and of $SiO_{1.65}$ the second layer were found. The stoichiometry of second layer in the sample S2 has an estimated value of $SiO_{1.72}$.

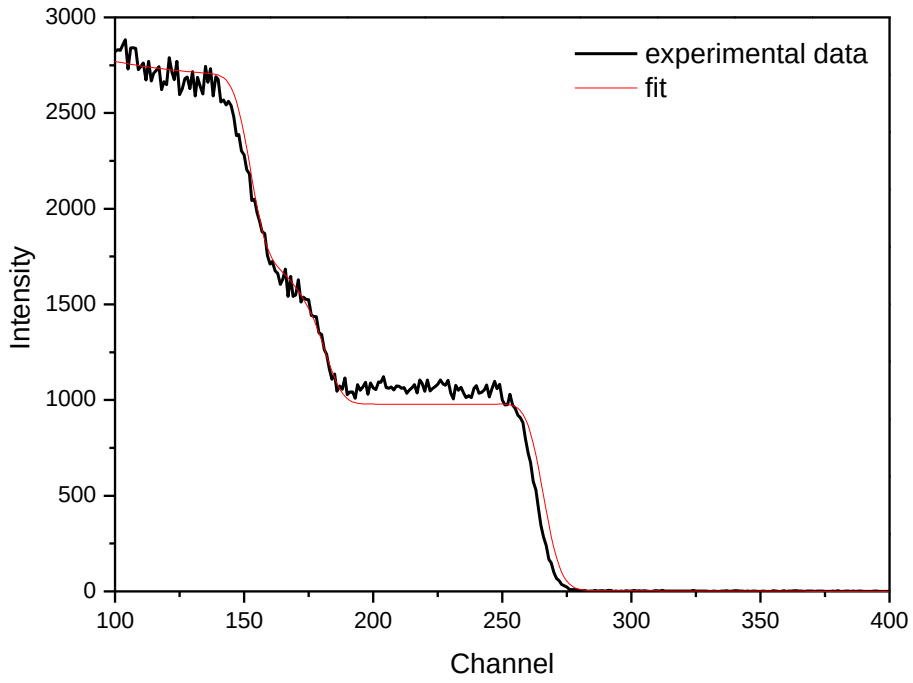

Figure 3. RBS spectra of S1 after annealing (black) and fit for a double layer structure (red).

Nevertheless the results should be regarded carefully, because SRO is multi phase material and therefore not homogenous [12].

The emission found in the PL spectra of S1 and S2 (Figure 4) is similar to the one of single layers with similar Si content (second layer), intensity, peak position and shape are comparable to values already published [12,15]. In both samples the strongest emission is found at 720 nm. While the peak shape is similar, the intensity of S2 is 50 % lower compared to S1. This result is not surprising since the thickness of the layer in the samples differs strongly.

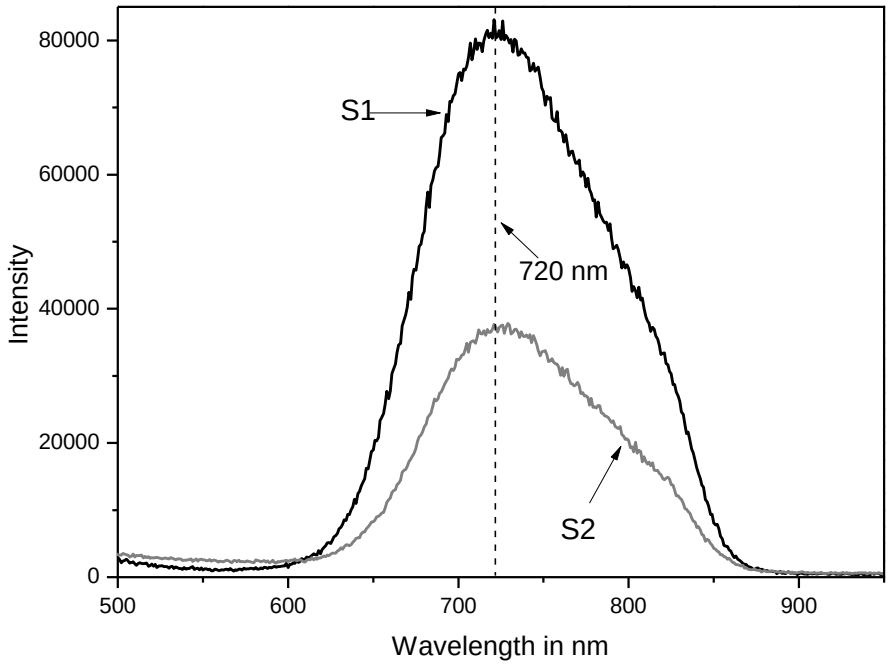

Figure 4. PL spectra of S1 and S2 after annealing for 30 min at 1100 °C.

4. DISCUSSION

a) Si Nano Structures

If the silicon excess is higher than 12% ($SiO_{1.25}$ [11]), even for thin layers around 8 nm the formation of the Si nIs can be observed. From a kinetic point of view, the formation of the Si nIs is reasonable. After the deposition process the excess Si is regularly distributed in small, amorphous agglomerates [16]. Due to the high amount of surface atoms and dangling bonds these Si atoms are in an energetically unfavorable state. While Si atoms in the SiO_2 matrix (Si 1 in Figure 5) can only conglomerate to Si nCs (Oswald ripening) during the annealing process, atoms near the substrate (Si 2 in figure 5) also can grow epitaxially on the Si surface and form Si nIs to achieve an energetically more favorable state (scheme in Figure 5, right). Due to the high number of Si nIs compared to Si nCs in S2 (Figure 1c,2c), it can be assumed that the formation of Si nIs is energetically favored over the formation of Si nCs.

b) Optical Properties

The thickness and micro structure of the bottom layer do not have influence on the emission and PL of the top layer. For both samples a high PL is found after annealing at 1100°C. On the other hand, the excess Si in the top layer has no influence on the formation of the Si nIs. The sharp interface found in S2 excludes an interlayer diffusion and oxidations processes between the two layers.

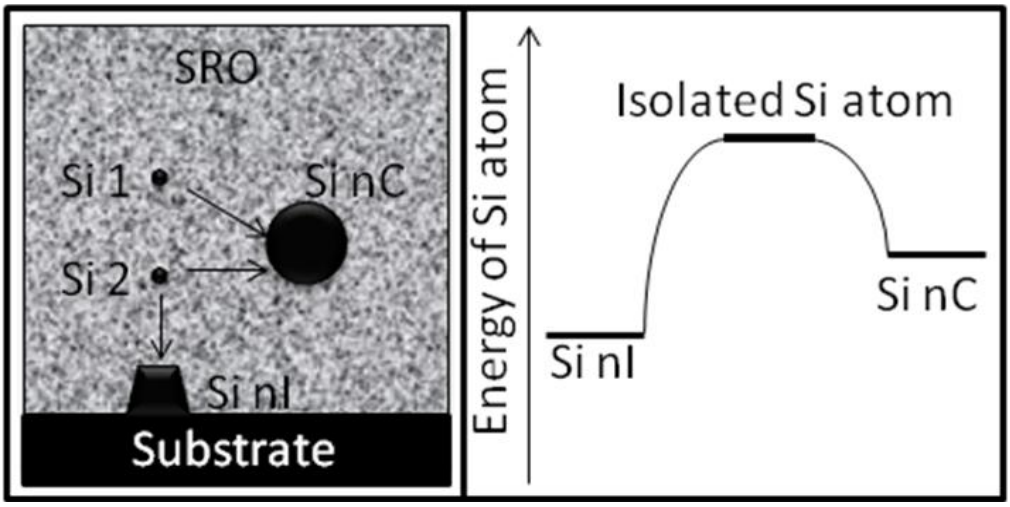

Figure 5. Schematic representation of the diffusion of Si atoms (left) and energy of Si atoms in different agglomerations (right).

Based on our data it should be possible to design each layer individually for the desired application. The peak position at 720 nm and the peak shape are similar, indicating that the micro structure of the emission centers is similar in both samples. This allows the variation of the Si:O ratio in this layer over a certain range. The possibility to design the properties of each layer individual is important for possible future applications. The density and shape of the Si nIs can be influenced by the layer thickness and the amount of excess Si within this layer, while the intensity of the PL can be controlled by the thickness of the second layer.

CONCLUSION

Using a multi-layer approach it was possible to synthesize SRO films which can combine the interesting optical and electrical properties of this material. The formation of Si nIs can be controlled by the stoichiometry and thickness of the first silicon rich layer, by varying this parameters it is possible to achieve a regular array of Si nano structures. Near the Si substrate the formation of Si nIs at the substrate/film boundary seems be to favored over the formation of Si nCs in the SiO_2 matrix. The first layer has no influence on the optical properties of second photoactive layer. The emission found is comparable with single layers with similar stoichiometry. This gives the possibility to design the properties of each layer individually, an important step forward to the fabrication of Si based optoelectronic nano devices.

ACKNOWLEDGMENT

The Deutsche Forschungs Gemeinschaft (DFG) and CONACyT are acknowledged for financial support. We also appreciate the sample preparation by the technicians of the INAOE microelectronics laboratory, especially Pablo Alarcón.

REFERENCES

[1] M. S. Gudiksen, L. J. Lauhon, J. Wang, D. C. Smith, and C. M. Lieber, "Growth of nanowire superlattice structures for nanoscale photonics and electronics," *Nature*, vol. 415, no.7, pp. 617-620, 2002.

[2] W. Liu, W. T. Zheng, and Q. Jiang, „First-principles study of the surface energy and work function of III-V semiconductor compounds ," *Phys. Rev. B*, vol. 75, pp. 235322, 2007.

[3] A. Wilk, A. R. Kovsh, S. S. Mikhrin, C. Chaix, I. I. Novikov, M. V. Maximov, Yu. M. Shernyakov, V. M. Ustinov, and N. N. Ledentsov, "High-power 1.3μm InAs/GaInAs/GaAs QD lasers grown in a multiwafer MBE production system," *J. Crystal Growth*, vol. 278, no. 1, pp.335-341, 2005.

[4] H.Yang, B. Zhang, X. Wang, X. Wang, T. Li, S. Xie, and X. Yao, "Sol–gel synthesis and optical properties of size controlled Indium Arsenide nanocrystals embedded in silica glasses," *J. Crystal Growth*, vol. 280, no. 3-4, pp. 521–529, 2005.

[5] M. Herrera, M. Chi, M. Bonds, N. D. Browning, J. N. Woolman, R. E. Kvaas, S. F. Harris, D. R. Rhiger, and C. J. Hill, "Atomic scale analysis of the effect of the SiO_2 passivation treatment on InAs/GaSb superlattice mesa sidewall," *Appl. Phys. Lett.*, vol. 93, pp. 093106, 2008.

[6] R. Negishi, M. Suzuki, and Y. Shigeta, "Study of photoelectron spectroscopy from extremely uniform Si nanoislands on Si(111) 7×7 substrate," *J. Appl. Phys.*, vol. 96, no. 9, pp.5013-5016, 2004.

[7] M. Ieong, B. Doris, J. Kedzierski, K. Rim, and M. Yang, "Silicon Device Scaling to the Sub-10-nm Regime," *Science*, vol. 306, pp. 2057-2060, 2004.

[8] D. Natelson, " Nanofabrication - Best of both worlds", *Nature materials*, vol. 5, pp 853-854, 2006.

[9] R. Turton, *The Quantum Dot: A Journey into the Future of Microelectronics*, Oxford University Press, New York, USA, 1995.

[10] R. P. Andres, J. D. Bielefeld, J. I. Henderson, D. B. Janes, V. R. Kolagunta, C. P. Kubiak, W. J. Mahoney, and R. G. Osifchin, "Self-assembly of a two-dimensional superlattice of molecularly linked metal clusters", *Science*, vol. 273,no. 5282, pp. 1690–1693, 1996.

[11] Z. Yu, M. Aceves-Mijares, A. Luna-López, J. Du, D. Bian, "Formation of silicon nanoislands on crystalline silicon substrates by thermal annealing of silicon rich oxide deposited by low pressure chemical vapour deposition", *Nanotechnology*, vol. 17, no 19, pp.4962-4965, 2006.

[12] A. Morales, C. Dominguez, J. Barreto, ; M. Rievera, M. Aceves, J.A. Luna, Z. Yu, R. Kiebach, Spectroscopical analysis of luminescent silicon rich oxide films, *Rev. Mex. Fis.*, vol. 53, no. 7, pp. 279-282, 2007.

[13] Z. Yu, M. Aceves, J. Carrillo, F. Flores, "Charge trapping phenomenon in Al/SRO/Al on Si structure by lateral electrical stress", *Superficies y Vacío*, vol. 16, no.4, pp. 25-29, 2003.

[14] Z. Yu, M. Aceves, F. Wang, J. Carrillo, R. Kiebach, K. Monfil, "Room temperature quantum tunneling and Coulomb blockade in silicon-rich oxide", *Physica E*,vol. 41, no. 2, pp. 264-268,2008.

[15] F. Flores Gracia, M. Aceves, J. Carrillo, C. Domínguez, C. Falcony, "Photoluminescence and cathodoluminescence characteristics of SiO_2 and SRO films implanted with Si", *Superficies y Vacío*, vol. 18, no.2, pp. 7-13, 2005.

[16] R. Kiebach, .J.A. Luna-López, G. Osvaldo Dias, M. Aceves-Mijares, J.W. Swart, "Characterization of Silicon Rich Oxides with Tunable Optical Band Gap on Sapphire Substrates by Photoluminescence, UV/Vis and Raman Spectroscopy", *J. Mex. Chem. Soc.*, vol 52, no. 3, pp. 212-218, 2008.

Smart Nanocomposites
Volume 1, Issue 1.
ISSN: 1949-4823

SYNTHESIS OF LIGHT EMITTING SIO_X LAYERS WITH CALCULABLE OPTICAL PROPERTIES – A FIRST STEP TO CONTROLLED INTEGRATION OF PHOTOLUMINESCENTE ACTIVE COMPOUNDS IN SILICON BASED DEVICES

***Ragnar Kiebach*[*a], *Alfredo Morales*[b], *Karim Monfil*[a], *Zhenrui Yu*[a], *Enrique Quiroga*[c] *and Mariano Aceves-Mijares*[a]**

[a]INAOE, Apdo. 51, Puebla, Pue. 72000, México
[b]IMB–CNM (CSIC), Campus UAB. 08193, Bellaterra, Barcelona, España
[c]Christian Albrechts Universität zu Kiel, 24118 Kiel, Germany

ABSTRACT

Silicon Rich Oxide (SRO) is an interesting candidate for use in optoelectronic devices due to its light emitting properties. Until now, most experiments are try-and-error and no models exist to calculate the optical properties of this interesting class of material. Here, the investigated samples were synthesized by low pressure chemical vapor deposition (LPCVD) and their photoluminescence (PL) and absorption in the infrared (IR) were analyzed. All samples studied show an intense PL in the region of red light (~ 725 nm).

The observed intensity increases with increasing layer thickness and decreasing Si excess. In the IR spectra a peak shift to higher wavenumbers for increasing layer thickness is found. Based on this data for the PL as well as for IR, a model has been developed which explains observed results. With these models it is possible to predict and calculate the optical properties of SRO and therewith to design these materials with specific characteristics.

Keywords: Si nano crystals, nanostructured materials, luminescence, silicon rich oxide, IR spectroscopy.

[*] Corresponding author: rkie@inaoep.mx, Tel: +52 (222) 266-31-00, Fax:+52 (222) 247-05-17, INAOE, Apdo. 51, Puebla, Pue. 7200, México

1. INTRODUCTION

An interesting candidate for light emitting devices currently attracting much attention are silicon nano crystals (Si nc), which can be obtained isolated in solution [1-2] or embedded in a SiO_2 matrix (SiO_x x<2 (sub-stoichiometric silicon oxide)) [3-6]. SiO_x is of special interest, because such systems are appropriate for the integration of optical and electronic data processing circuits on the same chip, so called optoelectronic circuits (OEC). Moreover the fabrication process is compatible with the present large scale integration technologies [7,8]. The Si nc in these systems have an enlarged band gap with respect to the bulk material and already at room temperature an intense visible photoluminescence (PL) is observed. The PL consists of intense emission peaks in the near infrared, visible and near ultraviolet regions. It was established that blue and green PL are caused by various emitting centers in the silicon oxide, while the nature of the more intense PL in orange-red region is still discussed [9,10,11].

In order to obtain SiO_x, a large variety of techniques has been proposed: ion implantation of Si into SiO_2 [12,13], magnetron sputtering of Si and SiO_2 [14,15], laser ablation of Si targets [3,16], molecular epitaxy, thermal evaporation of SiO [17,18], plasma enhanced chemical vapor deposition (PECVD) and LPCVD. In our days many papers have been published describing different optical properties of SiO_x (x<2), depending on the synthesis technique and the reaction parameters [3-6,19-22]. Until now these experiments are try-and-error and it is not possible to predict the physical properties or to design these optically active films with certain characteristics. Another need for using this material for application is a fast, cheap and reliable method to check the quality of the devices in the production line.

In the here presented publication it is shown that both needs can be fulfilled. Firstly, a model has been developed, which makes it possible to estimate the PL depending on the reactant gases ratio and the layer thickness. Additionally this model allows a calculation of the maximal achievable PL for a certain stoichiometry. Secondly, we show how the thickness or the stoichiometry of samples can be checked quite easy with IR spectroscopy by evaluating the peak shifts using our second model.

2. EXPERIMENTAL

SRO films with different thicknesses were deposited on n type (100) Si wafers. A hot wall reactor was used as reaction vessel and the pressure was controlled by mass flow controllers and a pressure sensor. A silane (SiH_4) and nitrous oxide (N_2O) mixture at 700 °C was used with different partial pressure ratios (Ro) according to:

$$Ro = \frac{p[N_2O]}{p[SiH_4]} \quad .$$

Samples with two different Ro and therewith different *stoichiometry (*Ro = 20 ($SiO_{1.38}$), Ro = 30 ($SiO_{1.58}$)) were synthesized. After deposition, SRO films were thermally annealed at 1100 ºC for 60 minutes in N_2 atmosphere.

PL at room temperature was carried out with a Perkin Elmer luminescence spectrometer model LS50B, which is controlled by computer. The samples were excited using 230 nm and 250 nm radiation. PL measurements were scanned between 400 and 900 nm (3.1–1.37 eV) with a resolution of 2.5 nm.

Infrared measurements were done using a FTIR BRUCKER Vector 22 spectrometer. The scanned range was between 350 cm^{-1} and 3500 cm^{-1} with 2.5 cm^{-1} of resolution.

The thickness and refraction index of the SRO films were measured using a Gärtner L117 ellipsometer with incident laser wavelength of 632.8 nm.

3. RESULTS

3.1. Photoluminescence

In Figure 1a,b the PL spectra for Ro = 20 and Ro = 30 for different layer thicknesses are shown. In general, the PL spectra consist of one broad band, peaked at 1.7 eV (725 nm) called red band (R-Band). As expected, the observed PL intensity increases with increasing layer thickness. The intensity for Ro = 20 compared to Ro = 30 is around 2-3 times higher. Interestingly the increase of the PL intensity with increasing thickness strongly depends on the stoichiometry in the investigated samples. For Ro = 30 an almost linear increase is found (Figure 1b), while the PL intensity of the silicon richer Ro = 20 (Figure 1a) sample seems to reach a maximum. For Ro = 20 no significant change in the intensity between a layer thickness of 197.5 nm and 485.2 nm is observed, whereas a change from 107.4 nm to 197.5 nm leads to a doubling of the PL intensity. All samples were excited with 230 nm and 250 nm wavelength but no significant change in the results for these experiments was found.

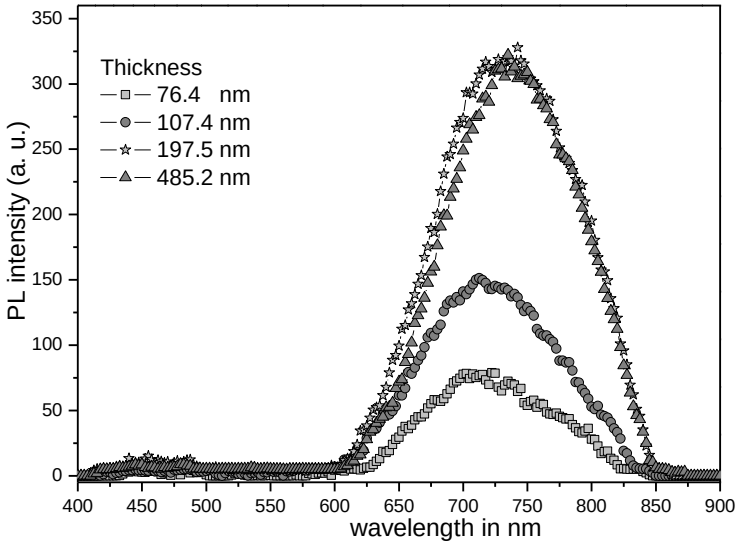

Figure 1a. PL spectra of Ro = 20 for different layer thicknesses.

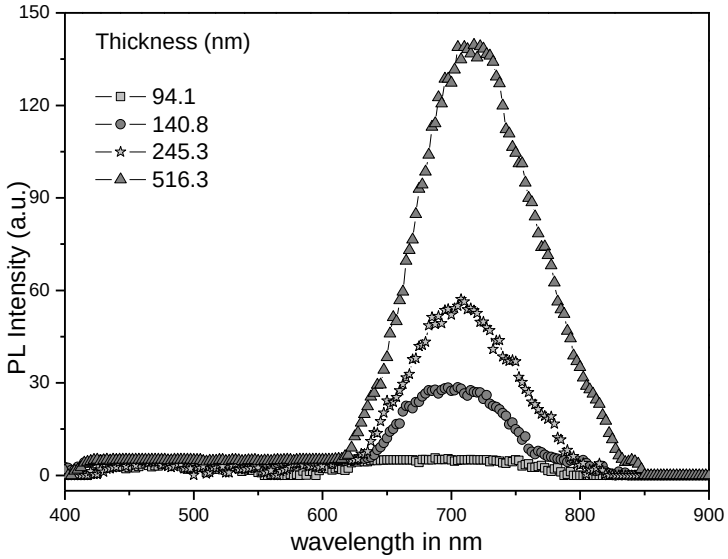

Figure 1b. PL spectra of Ro = 30 for different layer thicknesses.

3.2. Infra Red Spectroscopy

In Figure 2a and 2b the IR absorbance spectra for Ro = 20 (a) and Ro = 30 (b) are shown in the region from 350 cm^{-1} to 3500 cm^{-1}. In all spectra three modes are observable which are related to the presence of amorphous SiO_2.

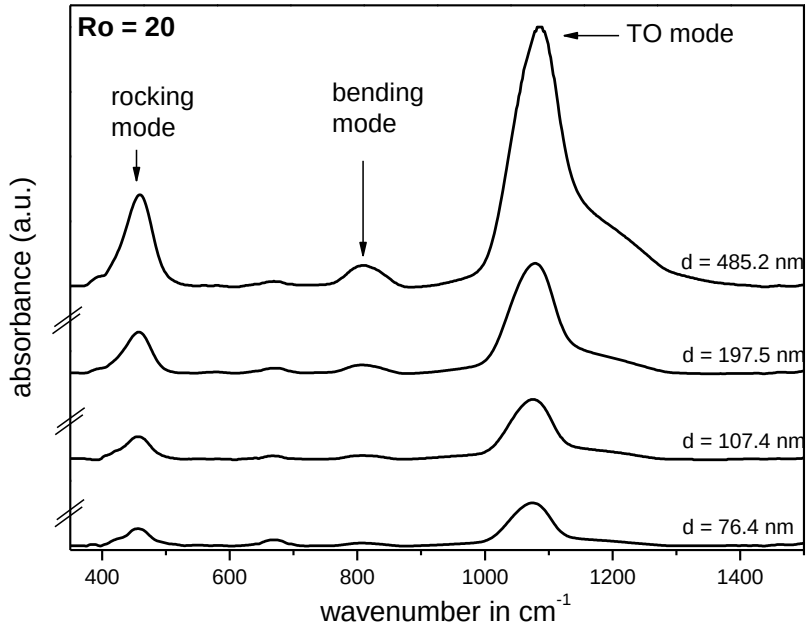

Figure 2a. IR spectra for Ro 20 for different layer thicknesses.

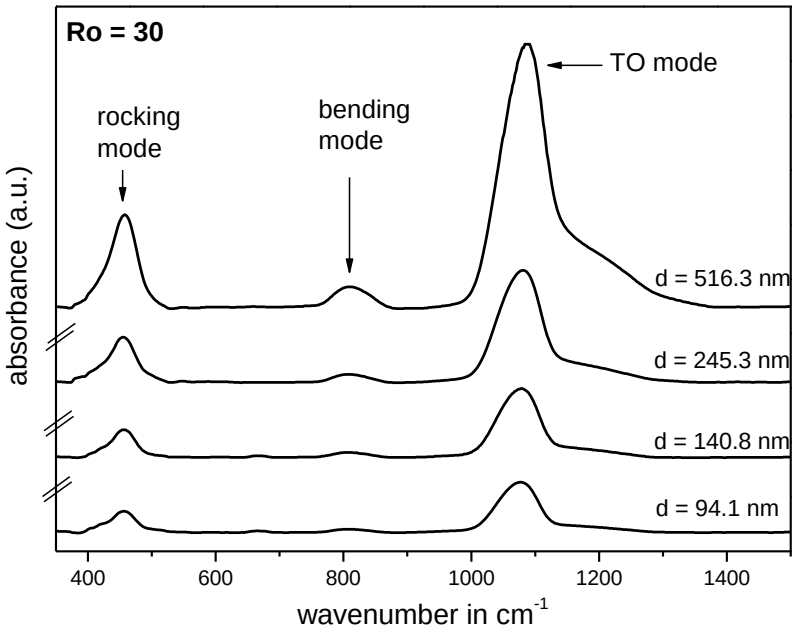

Figure 2b. IR spectra for Ro = 30 for different layer thicknesses.

The first mode occurs around 480 cm-^{1} and can be assigned to the Si-O rocking mode, the second, less intense, mode around 820 cm^{-1} is related to the Si-O bending mode. The most intense mode is the TO mode (transverse optic mode) around 1076 cm^{-1}, which is associated with the asymmetric stretch motion of the bridging oxygen atom.

As shown in Figure 2, the peak position of the TO mode shifts with increasing film thickness to higher wavenumbers. Additionally a shoulder around 1200 cm^{-1} appears for thicker samples. As expected the peak intensities increase almost linearly with the layer thickness of the SiO_x films. For an accurate determination of the peak position, the TO mode and the shoulder were fitted separately using Gaussian profiles.

4. DISCUSSION

To understand the PL and its emission process in these systems, several factors have to be considered. The first factor influencing the optical properties is the synthesis technique. The results of here investigated samples, for example, differ from the results where other deposition methods were used [3]. Also important is the origin of the PL, but especially for the intense PL in orange-red region the model of excitonic recombination in quantum confined Si nc does not explain experimental results satisfactorily and other radiative channels are still discussed [5,9-11,21,22]. In the here presented results, the peak position of the R-band does not change significantly, so it can be assumed that for all experiments the mechanisms of the PL, the radiative channels and the emission centers, are the same. For further discussion the kind of micro structure (emission centers) responsible for the PL is assumed to be identical, independently from the reactant ratio of the investigated thin films. While the radiative channels are the same, the number of channels or number of defects seem

to depend on the stoichiometry, explaining the different intensities for Ro = 20 and Ro = 30. For a homogenous composition, which has been observed by TEM spectroscopy before [23], one would expect a linear increase of the intensity with the layer thickness. The data for Ro = 30 could satisfy this expectation on the first look, but for Ro = 20 no linear trend is observed. To explain this non linear trend, absorption effects must be considered. Recently we published the absorption coefficients of different Ro for different excitation wavelengths [24]. Taking those results in consideration, we propose the following model to calculate the PL intensity for different Ro in dependence of the layer thickness:

According to *Lambert Beer* Law the incoming excitation beam with wavelength λ_{ex} and initial Intensity I_0 will reach the emission centers found at depht d_i with the following intensity:

$$I_{ex} = I_0 e^{-\alpha_{ex} d_i} \tag{1}$$

where α_{ex} is the absorption coefficient of the film with the stoichiometry Ro for the excitation wavelength λ_{ex}.

Comparable is the emission progress; the emitted light with the wavelength λ_{em} and Intensity I_{em} will reach the detector with following intensity I_{obs}:

$$I_{obs} = I_{em} e^{-\alpha_{em} d_i} \tag{2}$$

where α_{em} is the absorption coefficient for the emission wavelength. The intensity of the excitation beam and the intensity of the emission centers of certain depth in the film are linked by:

$$I_{em_i} = C_{eff} I_0 e^{-\alpha_{ex} d_i} \tag{3}$$

in which the conversion efficiency C_{eff} is:

$$C_{eff} = n_i c_{eff} \tag{4}$$

where n_i is number of emission centers at certain depth and c_{eff} the conversion rate of one emission center. The observed intensity coming from the emission centers of depth d_i can be described as:

$$I_{obs} = C_{eff} I_0 e^{-\alpha_{ex} d_i} e^{-\alpha_{em} d_i} = C I_0 e^{-d_i (\alpha_{ex} + \alpha_{em})} \tag{5}$$

The total observed emission at the wavelength λ_{em} from a film with the thickness d is then given by:

$$I_{\lambda_{em},obs} = C_{eff} I_0 \int_0^d e^{-x\ \alpha_{ex} + \alpha_{em}}\ dx = \frac{C_{eff} I_0}{\alpha_{ex} + \alpha_{em}} \left[1 - e^{-d(\alpha_{ex} + \alpha_{em})}\right] \tag{6}$$

According to eq.6, the maximum intensity which can be observed from a film with unlimited thickness d_∞ is:

$$I_{\lambda_{em},obs_{\max}} = \frac{C_{eff} I_0}{\alpha_{ex} + \alpha_{em}} \tag{7}$$

and the percentage of the maximum possible intensity reached after certain thickness d can be calculated by:

$$\%I_{\lambda_{em},obs_{myx}} = 1 - e^{-d\ (\alpha_{ex} + \alpha_{em})} \times 100 \tag{8}$$

In Figure 3a and Figure 3b $\%I_{\lambda_{em},obs_{myx}}$ calculated with eq. 8 over d for Ro = 20 and Ro = 30 is compared with the observed PL (scaled). It is clearly shown that the intensity I_{em} is growing, as described in our model, with the layer thickness, proving that it is possible to calculate the PL for a certain reactant ratio and layer thickness with accuracy.

As expected, the stoichiometry has a significant influence on the absorption properties, which is already indicated by the value of the absorption coefficients (for Ro = 20 $\alpha_{250\ nm}$= $4.8 \cdot 10^4$ cm^{-1} and for Ro = 30 $\alpha_{250\ nm}$= $9 \cdot 10^3$ cm^{-1} [24]). While for Ro = 30 after a 500 nm only 40 % of the possible maximum intensity in the PL is reached, for Ro = 20 already more than 80 % of the maximum is reached. An important consequence of these results for application is that due to absorption effects (here especially for Ro = 20) a maximum PL (calculable with eq.7) is reached after a certain thickness and by further increasing no significant change in observed PL will be found.

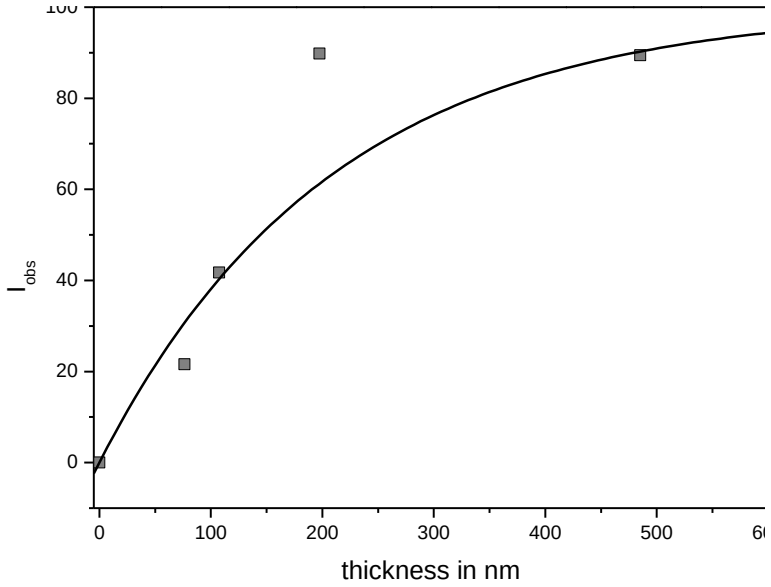

Figure 3a. Calculated Intensity (straight line) and observed PL (squares, scaled) for different layer thicknesses for Ro = 20.

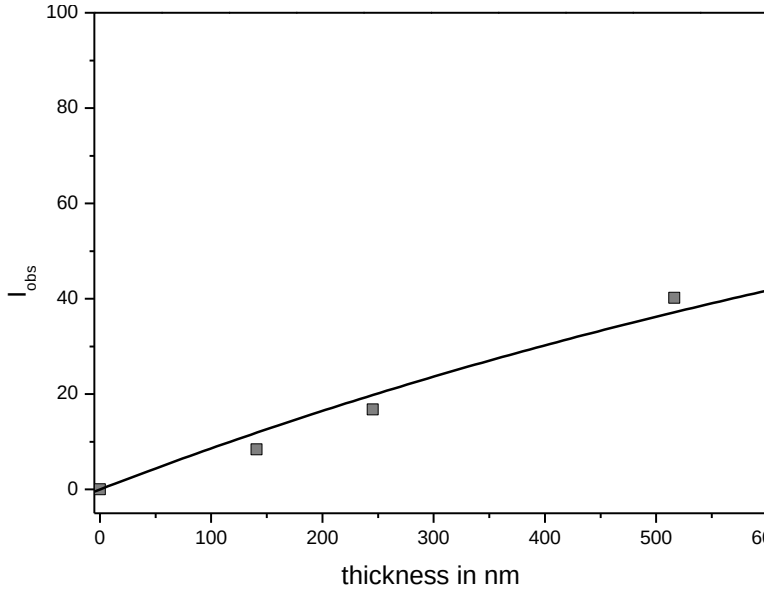

Figure 3b. Calculated Intensity (straight line) and observed PL (squares, scaled) for different layer thickness for Ro = 30.

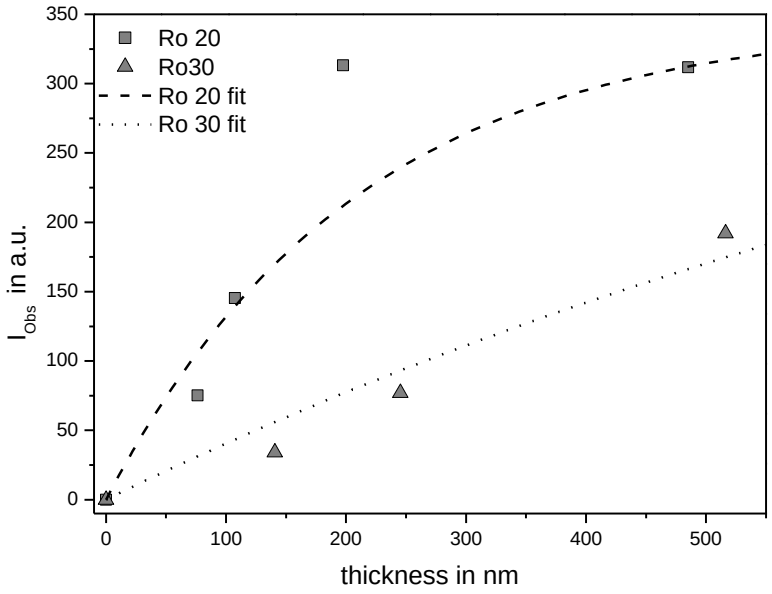

Figure 3c. Comparison of the calculated intensities (doted lines) and observed PL (symbols) for different layer thicknesses for Ro = 20 and Ro = 30.

Another possibility is to fit the data of the PL with eq. 6 (Figure 3c). As the result, from these fits it is possible to compare C_{eff}, from the term:

$$\frac{C_{eff} I_0}{\alpha_{ex} + \alpha_{em}}$$

In our case the intensity I_0 is the same for all experiments, and the absorption coefficients are known, so a direct comparison of C_{eff} for the different stoichiometries Ro = 20 and Ro = 30 is possible. As described above it is very likely, that the mechanism and type of emission centers responsible for the PL are identical. In this case c_{eff} in eq. 4 should be constant. This gives the interesting opportunity to compare the relation of the density of emission centers in the different samples. In our case in films with Ro = 20, the density of emission centers is 3.6 times higher than in films with Ro = 30, showing that by varying the reactant ratio a broad intensity spectra can be reached.

In the IR spectra for all films the vibrational frequency of the TO is shifted to lower wavenumbers compared with bulk α-SiO_2 (1090 cm^{-1}), a discrepancy which is known for thermal grown silicon oxides, in which the TO modes typically appear around 1076 cm^{-1} [4,5,25], comparable with the here presented results. Besides this discrepancy, which has not been discussed in detail, a significant blue shift occurs in our films with increasing layer thickness (Figure 4).

Two factors have to be taken into consideration to explain this observation. The first one is the presence of defects which comes along with the presence of a sub-stoichiometric silcon oxide.

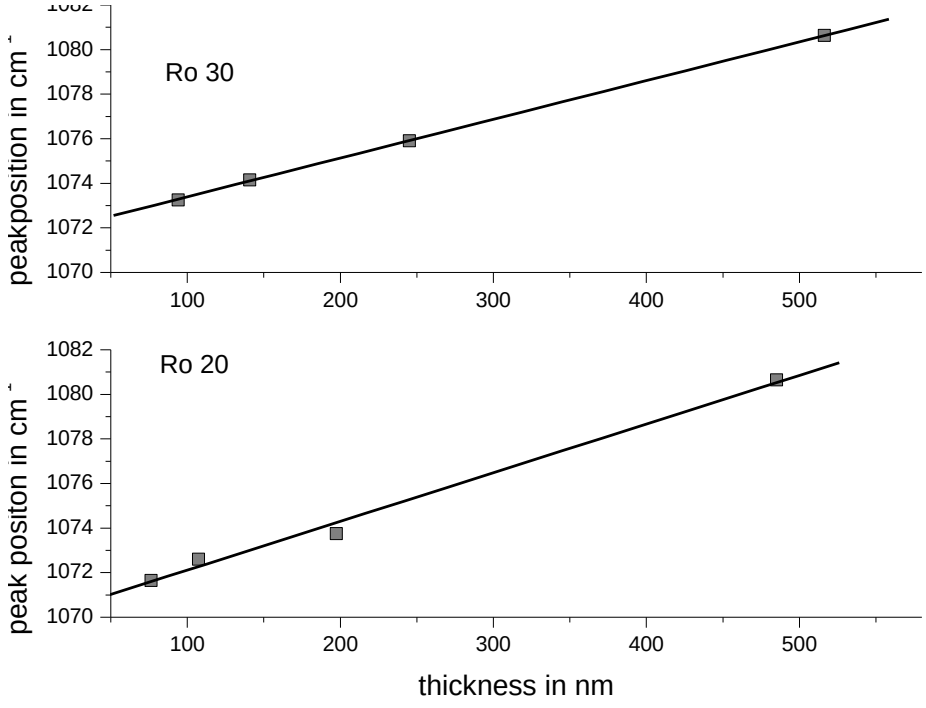

Figure 4. Peak shift of the TO mode for different thicknesses in Ro = 30 and Ro = 20.

At least two different defect structures are associated with these shifts in IR in literature. The first are the so called dangling bonds or *E`* centers (O≡Si·) [26], the second are oxygen-deficient centers (or neutral oxygen vacancy (NOV)) O≡Si-Si≡O [27]. It has been shown for pure SiO_2 films that these defects exist in the interface between the Si substrate and the grown SiO_2 film, and that in ultra thin films (< 10 nm) they cause a shift to lower wavenumbers. For SRO it can be assumed that the amount of suboxide is much higher than in pure SiO_2 films, because the defect containing interlayers between Si/SiO_2 do not occur only at the boundary of the substrate with the film but also around Si agglomerates (like Si nano crystals), which are distributed within the film. Based on this assumption, the difference in the peak position between different Ro can be explained. For Ro = 20 the values for the peak position for the same layer thickness compared with Ro = 30 are ~ 2 cm^{-1} lower. Taking the higher Si excess of Ro = 20 into consideration, the amount of Si aglomerates and therewith the ratio of defects/SiO_2 is higher, which causes a shift to lower wave numbers compared to Ro = 30.

Previously reported IR shifts [28] caused by annealing can also be explained in this way. It is known that annealing leads to a healing of defect structures, meaning that the amount of defects in annealed samples is significantly lower which leads to a shift towards higher wavenumbers (blue shift).

While a different ratio of defects/SiO_2 of a defect-rich suboxide layer can explain a peak shift for different concentration in the Si excess, it does not explain the correlation between peak shift and layer thickness (Figure 4). As the ratio of defects/SiO_2 is constant in a film independently of its thickness, no peak shift is expected at varying the thickness.

Excluding defects as the reason for thickness depending peak shift, other possibilities must be considered. The absorption frequency (ω) in the central and noncentral force approximation of TO mode is given by Eq. 3

$$\omega_{TO} = \left[\frac{2}{m_0} \left(\alpha \sin^2 \frac{\Theta}{2} + \beta \cos^2 \frac{\Theta}{2} \right) \right]^{\frac{1}{2}} \tag{9}$$

where Θ is the Si-O-Si angle between adjacent SiO_4 tetrahedra, m_0 is the mass of the oxygen atom and α and β are the central and noncentral force constants. As clearly seen in Eq. 3, no dependence of the layer thickness is given which could explain the peak shift in TO Mode (Figure 2).

Martinet and Devine [29] explained a peak shift in SiO_2 films with comparable thicknesses to here presented samples using a classic approach for a multiple reflection of beams incident on a thin film. In this approach, the different transmission coefficients at the boundaries SiO_2/air and $SiO_2/Si_{substrate}$ and the thickness dependency are considered (for more details compare [29]) and it has been shown that the overall transmission coefficient is correlated with the layer thickness *d*. Under the assumption that the Si excess is evenly distributed in the SiO_2 forming a homogenous layer with consistent transmission coefficient, which has been proven by TEM measurements, and that the amount of defect free SiO_2 in the matrix is huge compared with the one in the sub-oxide layers, the model from Martinet and Devine can be used as basic principle to explain the observed peak shift in our samples.

By comparison the influence of the two factors leading to a phase shift (first the concentration of the Si excess, second the layer thickness) is more or less equal. Reducing the

Si excess (for the same layer thickness) from 5.6 % (Ro = 20) to 3.4 % (Ro = 30) leads to a blue shift of 1.7 cm^{-1} while doubling the layer thickness from 1000nm to 2000 nm is accompanied with a blue shift of 1.8 cm^{-1}.

Summarizing the results it is possible to calculate a peak position in the here investigated range by using equation 10:

$$\omega_{d,Ro} = \left(P_{SiO_2} - \phi_{Ro}\right) + dB \tag{10}$$

where ω_{d,R_o} is the peak position depending on layer thickness *d* and Ro, P_{SiO_2} the peak position for a "pure" SiO_2 film, ϕ_{Ro} a constant for the peak shift caused by Si excess and *B* constant scaling factor for the layer thickness, depending on the Ro. An interesting feature of this formula is, that ϕ_{Ro} is related to the ratio of defects/SiO_2, which gives the possibility to compare the defect density of different samples, synthesis techniques or thermal treatments simply by IR spectroscopy. A larger ϕ_{Ro} implies a larger ratio of defects/SiO_2.

With the models developed here, SRO get more interesting for applications; firstly, its predictable and calculable PL makes it possible to design thin films with specific optical characteristics and secondly, with simple IR spectroscopy it is possible to monitor the synthesis process easily.

CONCLUSION

Based on experimental data from PL and IR spectroscopy, we were able to develop two models. The first one explains the intensity development in the PL for samples with different stoichiometries and different thicknesses. Even if the origin of the PL is still discussed, the model explains the correlation of film thickness and PL, taking absorption processes into consideration. Furthermore, this model allows calculating the maximum PL reachable for every stoichiometry. Also the comparison of the conversion efficiency between different samples is possible. The second model explains the shift in the TO mode found in the IR spectra. Considering defects and different transmission coefficients at the boundaries SiO_2/air and $SiO_2/Si_{substrate}$ it is possible to calculate the shift in IR spectra for different film thicknesses and stoichiometries. Using these two models, the properties of SRO deposited by LPCVD are much more predictable; a first step towards the design of an optical active layer has been done, bringing this class of material closer to application.

ACKNOWLEDGMENT

The Deutsche Forschungs Gemeinschaft (DFG) and CONACyT are acknowledged for financial support. We also appreciate the sample preparation by the technicians of the INAOE microelectronics laboratory, especially Quim. Pablo Alarcón.

REFERENCES

[1] Belomoin G, Therrien J, Smith A, Rao S, Twesten R, Chaieb S, Nayfeh MH, Wagner L, Mitas L. Observation of a magic discrete family of ultrabright Si nanoparticles. *Appl. Phys. Lett.* 2002;80(5):841-843.

[2] Nayfeh MH, Rao S, Nayfeh OM, Smith A, Therrien J. UV photodetectors with thin-film Si nanoparticle active medium. *IEEE Trans Nanotech* 2005;4(6):660-668.

[3] Gracia FF, Aceves M, Carillo J, Dominguez C, Falcony C. Photo- and cathodo - luminescence characteristics of SiO_2 and SRO films implanted with Si. *Superficies y Vacio* 2005;18(2):7-13.

[4] Khriachtchev L, Novikov S, Lahtinen J. Thermal annealing of Si/SiO_2 materials: Modification of structural and photoluminescence emission properties. *J. Appl. Phys.* 2002;92(10):5856-5856.

[5] Fernandez BG, Lopez M, Garcia C, Perez-Rodriguez A, Morante JR, Bonafos C, Carrada M, Claverie A. Influence of average size and interface passivation on the spectral emission of Si nanocrystals embedded in SiO_2. *J. Appl. Phys*. 2002;91(2):798-807.

[6] Cha D, Shin JH, Song IH, Han MK. Enhanced formation of luminescent nanocrystal Si embedded in Si/SiO_2 superlattice by excimer laser irradiation. *Appl. Phys. Lett*. 2004;84(8):1287-1289.

[7] Sui GG, Wu XL, Gu Y, Boa XM. Ultraviolet and blue emission from crystalline SiO_2 coated with $LiNbO_3$ and $LiTaO_3$. *Appl. Phys. Lett*. 1999;74(13):1812-1814.

[8] Tamura H, Ruckschloss M, Wirschem T, Veprek S. Origin of the green/blue luminescence from nanocrystalline silicon. *Appl. Phys Lett*. 1994;65(12):1537-1539.

[9] Kenyon AJ, Trwoga PF, Pitt CW, Rehm G. The origin of photoluminescence from thin films of silicon-rich silica. *J. Appl. Phys*. 1996;79(12):9291-9300.

[10] Lin GR, Lin CJ, Lin JK, Chou LJ, Chueh YL. Oxygen defect and Si nanocrystal dependent white-light and near-infrared electroluminescence of Si-implanted and plasma-enhanced chemical-vapor deposition-grown Si-rich SiO_2. *J. Appl. Phys*. 2005;97:094306.

[11] Chen XY, Lu YF, Wu YH, Cho BJ, Liu MH, Dai DY, Song WD. Mechanisms of photoluminescence from silicon nanocrystals formed by pulsed-laser deposition in argon and oxygen ambient. *J. Appl. Phys*. 2003;93(10):6311-6319.

[12] Koch F, Petrova-Koch V. Light from Si-nanoparticle systems - a comprehensive view. *J. Non-Cryst Solids* 1996;198-200(2):840-846.

[13] Kohon K, Osaka Y, Toyomura F, Katayama H. Photoluminescence of Si Microcrystals Embedded in SiO_2 Glass Films. *Jpn J. Appl. Phys*. 1994;33(1):6616-6622.

[14] Kanzawa Y, Kageyama T, Takeoka S, Fujii M, Hayashi, Yamamoto K. Size-dependent near-infrared photoluminescence spectra of Si nanocrystals embedded in SiO_2 matrices. *Solid State Commun* 1997;102:533-537.

[15] Patrone L, Nelson D, Safarov VI, Sentis M, Marine W, Glorico S. Photoluminescence of silicon nanoclusters with reduced size dispersion produced by laser ablation. *J. Appl. Phys.* 2000;87(8):3829-3837.

[16] Sachenko AV, Kaganovich EB, Manoilov EG, Svechnikov SV. Kinetics of exciton photoluminescence in low-dimensional silicon structures. *Semiconductors* 2001;35(12):1383-1389.

[17] Kahler U, Hofmeister H. Silicon nanocrystallites in buried SiO_x layers via direct wafer bonding. *Appl. Phys. Lett*. 1999;75(5):641-643.

[18] Rinnert H, Vergnat M, Marchal G, Burneau A. Strong visible photoluminescence in amorphous SiO_x and SiO_x:H thin films prepared by thermal evaporation of SiO powder. *J. Lumin.* 1999;80(1-4):445-448.

[19] Brongersma ML, Polman A, Min KS, Boer E, Tambo T, Atwater HA. Tuning the emission wavelength of Si nanocrystals in SiO_2 by oxidation. *Appl. Phys Lett*. 1998;72(20):2577-2579.

[20] Yamani Z, Gurdal O, Alaql A, Nayfeh MH. Correlation of diffuse scattering with nanocrystallite size in porous silicon using transmission microscopy. *J. Appl. Phys.* 1999;85(12):8050-8053.

[21] Jeong JY, Im S, Oh MS, Kim HB, Chae KH, Whang CN, Song JH. Defect versus nanocrystal luminescence emitted from room temperature and hot-implanted SiO_2 layers. *J. Lumin*. 1999;80(1-4):285-289.

[22] Khomenkova L, Korsunska N, Sheinkman M, Stara T, Torchynska TV, Hernandez HV. Radiative channel competition in silicon nanocrystallites. *J. Lumin*. 2005;115(3-4):117-121.

[23] Morales-Sánchez A, Barreto J, Domínguez-Horna C, Aceves-Mijares M, Luna-López JA. Sensors and Actuators A, to be published.

[24] Luna-Lopez A. Aceves-Mijares M, Malik O, Pedraza J, Falcony C. In: *International Commission for Optics* - 20 Conference 2005;6029:0602-29.

[25] Queene KT, Herbots N, Shaw JM, Atluri V, Chabal YJ. Infrared spectroscopic analysis of an ordered Si/SiO_2 interface. *Appl. Phys. Lett*. 2004;84(4):493-495.

[26] Nagai N, Yamaguchi Y, Saito R, Hayashi S, Kudo M. IR and EPR Study of the Na Ion-Implanted SiO_2/Si System. *Appl. Spectrosc* 2001;55(9);1207-1213.

[27] Zhang JY, Bao XM, Li NS, Song HZ. Photoluminescence study of defects in Si^+ ion implanted thermal SiO_2 films. *J. Appl. Phys*. 1998;83(7):3609-3613.

[28] Morales A, Domínguez C, Aceves M, Barreto J, Riera M. Compositional study of Silicon Rich Oxide films. In: *3rd International Conference on Electrical and Electronics Engineering Proceedings* 2006:278.

[29] Martinet C, Devine RAB. Analysis of the vibrational mode spectra of amorphous SiO_2 films. *J. Appl. Phys*. 1995;77(5):4343-4348.

Smart Nanocomposites
Volume 1, Issue 1.
ISSN: 1949-4823

PREPARING FILMS OF ZINC OXIDE WITH VARYING POROSITY BY SOL-GEL METHOD

Ekaterina Yanchinskaya, Kirill L. Levine*, Marina Tcaregorodceva, Sergey E. Sholkin, Anastasiya Speshilova, Elena Bogut and Anastasia Plotnikova

St. Petersburg State Polytechnical University
Department of Technology and Materials Research
St. Petersburg, Russia

ABSTRACT

Zinc oxide and its composites were under close focus of investigators in the last few years due to their unique properties. Development of nanotechnologies has initiated creating nanocrystals and nanostructures of zinc oxide, such as nanowires, nanotubes, and nanofilms, nanorings, that are promising in micro- and opto- electronics, in microsensors, photocatalysts, piesoconverters. This paper describes nanostructured films of zinc oxide, the influence of processing parameters on porosity of films is discussed.

INTRODUCTION

Zinc oxide and its composites were under close focus of investigators in the last few years due to unique properties of this material. Among its interesting physical and chemical properties are anisotropy of crystalline structure, semiconducting properties and large bandgap at the same time (3.37eV), luminescent properties [1,2] photoconductivity [3], high reflectance in visible and high absorbance in UV spectral range [4,5] lasing and electrooptic properties [6,7] strong piezo and piro electric properties [8,9] high heat conductivity [10,11]. Altogether makes this material very attractive for further investigations. Development of nanotechnologies initiated creation nanostructures of zinc oxide, such as nanofilms, nanowires, nanotubes, nanofilaments, nanorings [12], promising for micro and optoelectronic applications, microsensors, photocatalytic devices, and piesotransducers. Zinc oxide films are utilized in display devices [13] (light emitting diodes [38], transparent conductors), solar cells [14], fuel cells, gas detectors [15,16,17], devices utilizing surface acoustic waves [18,19,20]

* Author for correspondence. Email: levinkl@hotmail.com

The scope of this project was to investigate the influence of processing parameters on porous structure of zinc oxide films. These films with nanoporous structures are highly demanded in different areas of science for gas sensor and separating membrane applications.

Among different methods of growing ZnO films there are thermal evaporation method, [21] molecular beam epytaxy [22,23] nebulization at constant current [24,25], radiofrequency magnetron sputtering [26,27], reactive sputtering, [28], laser sputtering [29,30], in particular femtosecond and nanosecond sputtering [31]. All these methods, however, are expensive.

At industrial scale ZnO films are obtained by chemical condensation from gaseous phase [32,33,34,35]. This technology allows high speed of the process and high production rate. Drawback is the requirement to advance this process in camera with low pressure ($p = 10^{-3}$ Pa), that requires expensive equipment.

Films of rather large area is possible to obtain by relatively simple and cost-effective method of cathodic electrodeposition [36,37,38]. This method allows obtaining ZnO films from aqueous and non-aqueous solutions using salts $Zn(NO_3)_2$ and $ZnC1_2$ dissolved in propylene carbonate.

PREPARING NANOCOMPOSITES BY SOL-GEL METHOD

Majority of publications cite method of obtaining ZnO nanopowder suggested by Spanhel [39]. Recommended precursor was dehydrate zinc acetate ($C_4H_6O_4Zn{\cdot}2H_2O$), ethanol was used as a solvent, and lithium hydroxide as a stabilizer.

Based on this technology with minor modifications different groups have obtained ZnO films [40,41]. In [40] luminescent films were fabricated. Bahneman [42] modified this method using 2-propanol as a stabilizer for NaOH. Based on colloid solution obtained by this method thin ZnO films were synthesized from colloid solution.

Other researchers report synthesis of thin ZnO layers using zinc acetate dehydrate as a precursor and different alcohols as a solvent, such as 2 methoxyethanol [43,44,45] isopropanol [46], ethanol [47,48,49] and monoethanolamine as stabilizer (MEA).

MATERIALS AND METHODS

Samples Preparation

Sol-gel technology consists from few steps:

- Hydrolysis of metal salt at elevated temperature; partial salt neutralization followed by formation of a stable hydrosol containing nanoparticles of hydrated oxide;
- Complete neutralization of metal salt followed by rinsing and peptisation of the residual, and formation of a stable hydrosole;
- Hydrolysis of metal-organic compounds.

Obtaining ZnO gel

Zinc oxide gel was obtained by the following procedure. 3.10 g of ($Zn(CH_3OO)_2 \cdot 2H_2O$) was dissolved in 15 ml of isopropanol with the addition of 0.86 MEA and two drops of water. Obtained mixture was kept at 1 h at 60ºC, at the conditions of constant stirring, and then left overnight at room temperature.

The purpose of reagents is described in Table 1.

Table 1. Reagents and their purpose

Reagent	Formula	Purpose
Zinc acetate hydrous,	$Zn(CH_3OO)_2 \cdot 2H_2O$	Precursor
Isopropanol	$CH_3CH(OH)CH_3$	Solvent
Monoethanolamine (MEA)	C_2H_7NO	Stabilizer
Distilled water	H_2O	

As a substrate, panels from stainless steel of 3 x 3 cm size were used. Before the deposition they were degreased for 2.5 min at 60-70ºC in a mixture containing Na_2CO_3 30-40(g/l), and NaOH 10-15 g/l [50]. After degreasing, panels were rinsed by dipping in hot water for 1 min at 60-80ºC followed by rinsing in cold water for 1min.

Obtained gel was next day deposited onto cleaned panels by dipping. After that samples were treated thermally by drying for 10 min at 250ºC followed by sintering for 1 hour at different temperatures (350, 400, 450, 500, 550 ºC). Samples at different steps of this process are shown in Figure 1.

Figure 1. Left: panel with deposited gel prior to drying, Middle: panel with ZnO film after drying at 250ºC; Right: panel with ZnO film after sintering at 550ºC.

Thermal treatment was carried out in thermostat TC – 16A and high temperature oven ТУ 16-531.

Average thickness of ZnO films obtained by this method was 5μm.

Samples Analysis

Methods

X Rays Diffraction Analysis

X rays diffraction (XRD) analysis was carried out on DRON - 2 diffractometer at FeK_{α} radiation. Multicristalline (powder) method was used. Applied voltage and current were 30 KV and 20 mA, with slit sizes 1 and 0,5 mm at angular velocity 2 degrees/min in angle interval $\Theta = 7\ldots40^{o}$. Data was analyzed using databases PC PDF WIN.

Surface Area Measurements

Surface area was determined by low temperature desorption method at Sorbtmetr-M instrument by method of dynamic measurements. Carrier gas was helium, gas adsorber was nitrogen.

Electron Microscopy

Morphology was studied on scanning electron microscope (SEM) JEOL JSM– 6060.

Electrochemical Impedance Spectroscopy

Method of Electrochemical impedance spectroscopy (EIS) is based on measurements of the electrochemical dependence of impedance on frequency of alternating current. Similar to the resistance at constant current, impedance characterizes resistance to AC current in AC circuits.

Cell Design

Figure 2 shows schematic of the experiment. One-compartment cell contained three electrodes: working electrode, reference electrode, and counter electrode. Cell was placed in electrically conducting grounded Faraday cage in order to improve stability of measurements, and protecting from electro-magnetic interferences. Counter electrode was a platinized metallic grid fixed at platinized metallic rod. Measurement were taken in aqueous 0.1 M solution of sodium sulfate.

Measurements were taken at PC3 Potentiostat manufactured by Gamry Instruments.

RESULTS AND DISCUSSION

X-Ray Diffraction Analysis

Figure 3 displays curves of X-rays diffraction analysis. Peaks related to planes with indexes (100), (002), (101), (102), (110), (103), (112) were identified. The most intensive were three peaks related to planes (100), (002), (101) proving that there was no preferential direction of orientation in the films. Increasing sintering temperature resulted in the appearance of a preferential direction of orientation, and crystallinity of films that resulted in increased intensity of the reflections and decreased peaks half-widths on difractograms.

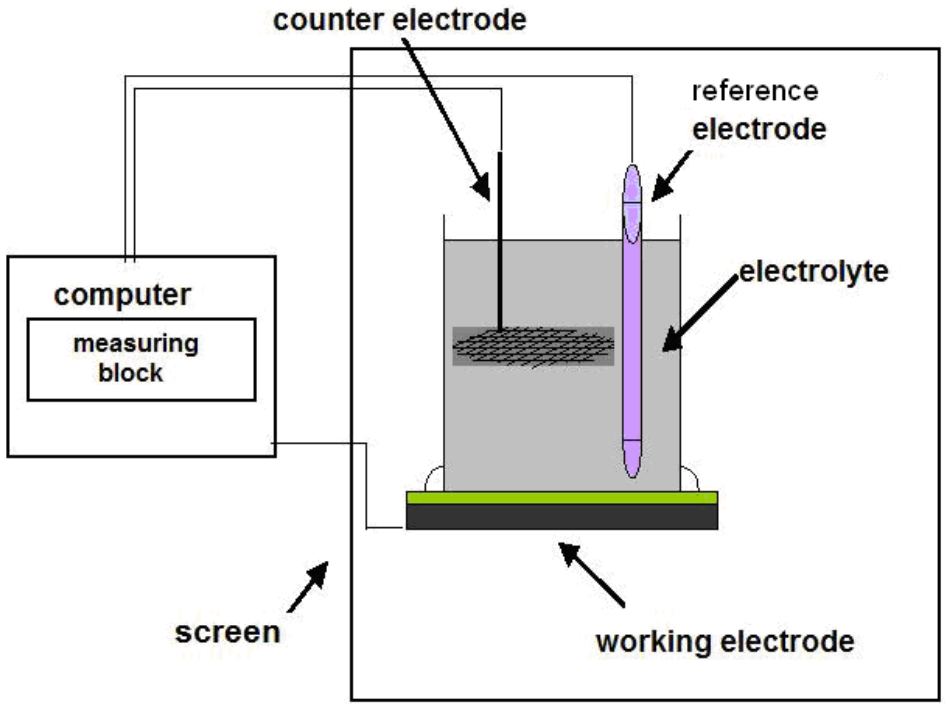

Figure 2. Schematic of the electrochemical experiment.

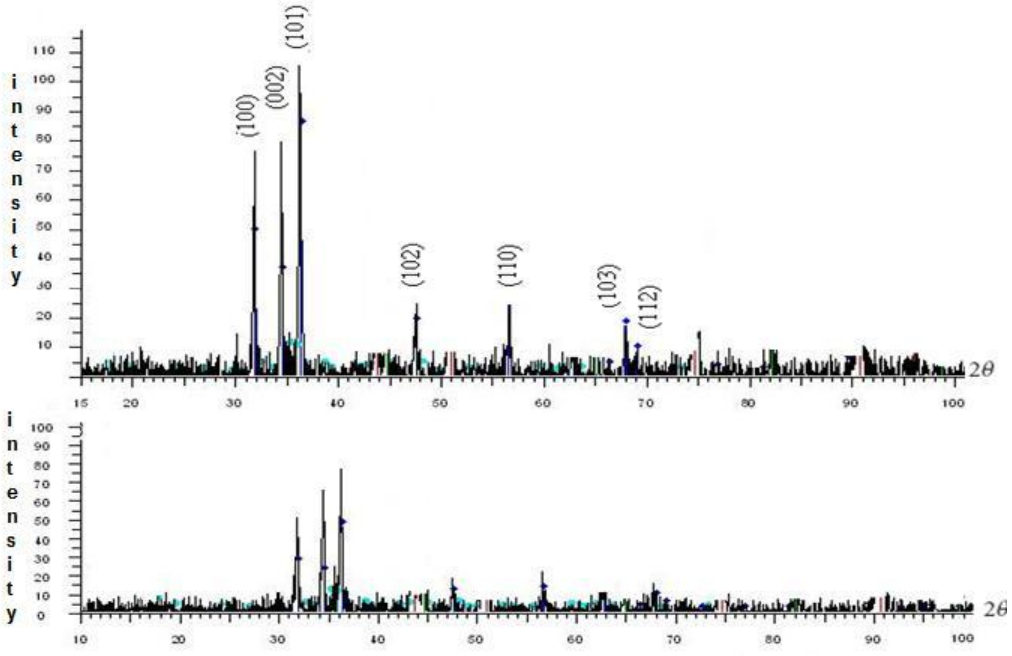

Figure 3. XRD curves of films with different temperature of sintering: top curve 350 ºC, bottom curve 550 ºC.

Lattice constants estimated from XRD data are shown in Table 2.

Table 2. Lattice constants

Sample	a, Å	b, Å	c, Å
1 (Tsint ºC)	3.25330	3.25330	5.20720
2 (Tsint ºC)	3.25682	3.25682	5.21251
3 ZnO (Wurtzite)	3.2501	3.2501	5.2071

Comparison shows that lattice constants for studied samples were close to a Wurtzite (polycrystalline hexagonal) form of zinc oxide.

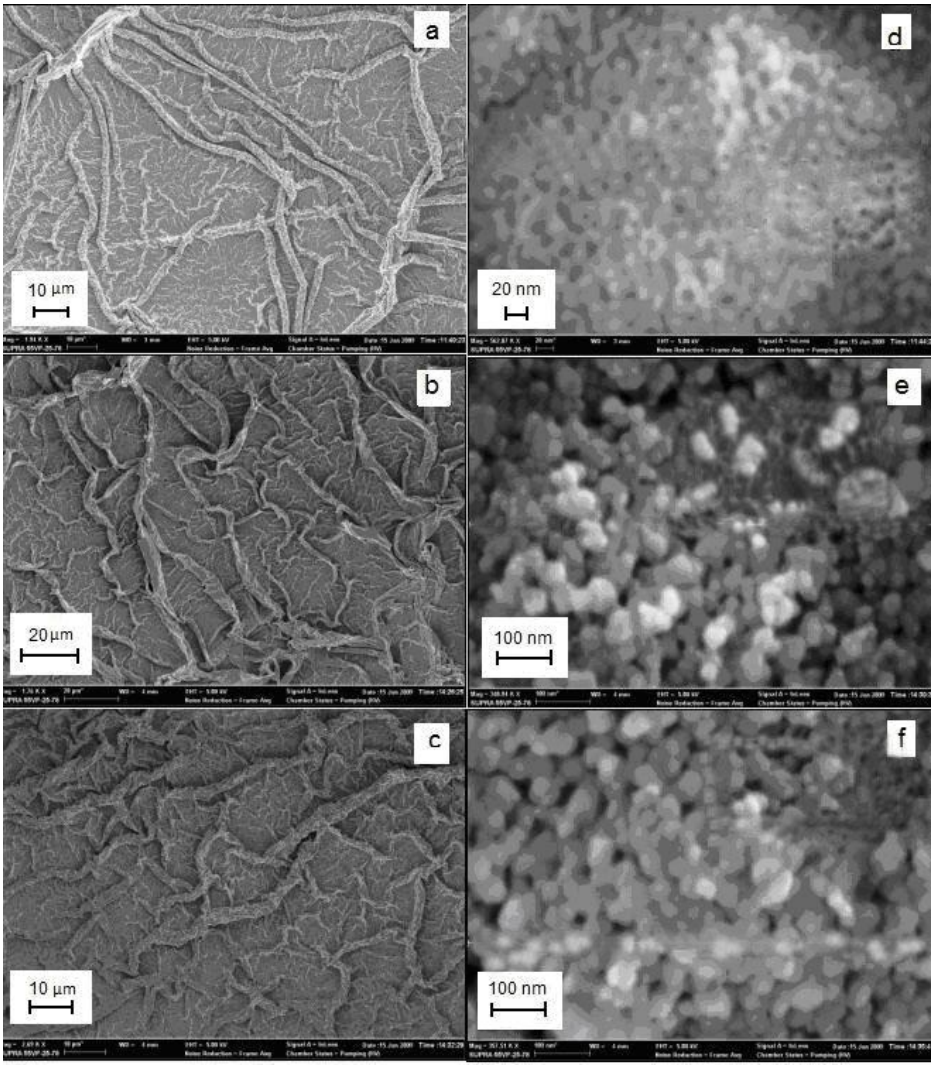

Figure 4. SEM image of ZnO films with different sintering temperature. a, d) T_{sint}=350 ºC ; b,e) T_{sint}=450 ºC ; c,f) T_{sint} =550ºC.

Surface Area Measurements

Surface area of two samples sintered at different temperatures was measured as:

Sample 1 (T_{sint}=350 ºC) - 4.812m^2 /g

Sample 2 (T_{sint}=550 ºC) - 6.91m^2 /g

Increasing sintering temperature increased surface area, therefore amount of pores increases. Using films as gas sensors requires high surface areas [51].

Scanning Electron Microscopy

SEM images (Figure 4) show fold-like structure with folds of various size. Their formation can be linked with thermal stresses occurring at the stage of thermal treatment. At larger magnifications it is clear that the film is composed from spherical particles. Size measurement data shows that average size depends on sintering temperature: when sintering temperature increases, average diameter (d) also increases.

Sample №1 (sintering temperature 350ºC) d≈15nm.

Sample №2 (sintering temperature 450ºC) d≈33nm.

Sample №3 (sintering temperature 550ºC) d≈47nm.

All the obtained samples can be characterized by porous structure. It can be suggested that pores are interlinked, possess different size and length, and form network of channels of different shape. SEM analysis only allows estimating surface average pore size that was found to be equal to 10-20 nm.

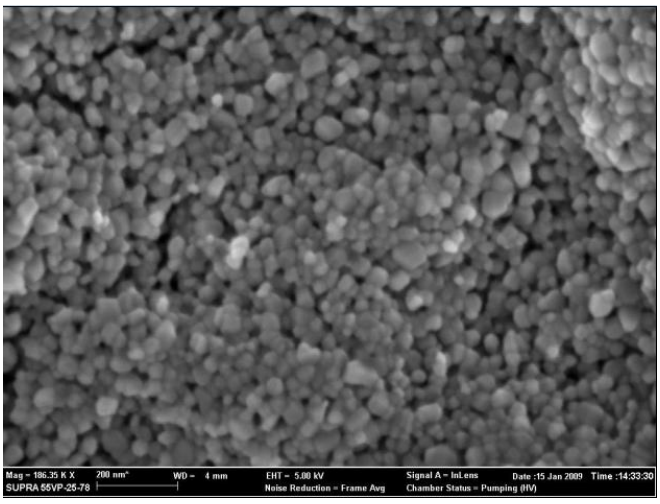

Figure 5. SEM image of ZnO film sintered at 550ºC.

ELECTROCHEMICAL IMPEDANCE SPECTROSCOPY (EIS)

Three sets of samples of the same composition, but different sintering temperature were studied by EIS. Modeling has revealed that all the obtained spectra can be relatively precisely described with the model of insulating coating shown in Figure 6.

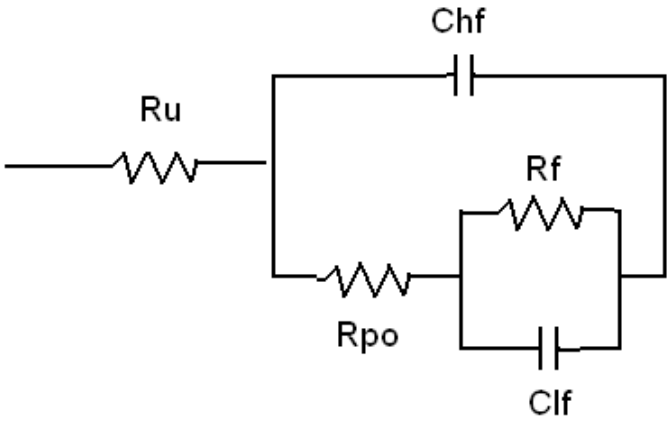

Figure 6. Equivalent electrical scheme for the model of insulating coating.

In this figure R_{p0} is charge transfer resistance, C_{hf} is high frequency capacitance formed by the Electrical double layer at the electrode/solution interface; R_f is specific resistance – resistance of electrolyte in pores; C_{lf} is low frequency capacitance, pseudocapacitance related to the electrochemical process of electron exchange at the electrode, and R_u – electrolyte resistance.

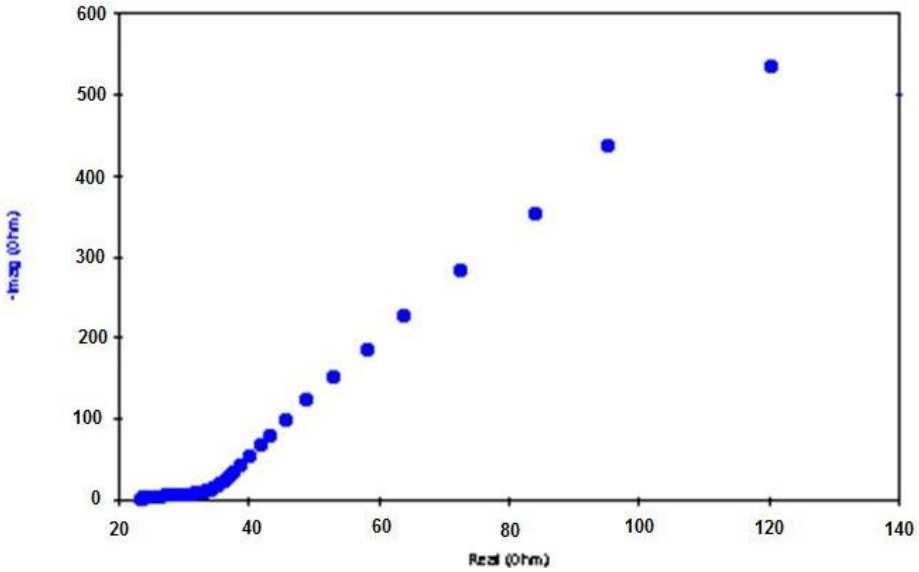

Figure 7. Nyquist plot for sample N 1, sintering temperature 350ºC.

Curvature in (Nyquist plot) shows two regimes. High frequency area – area of kinetics control. Characteristic semicircle is almost coinciding with abscissa that is a feature of the presence of a relaxation time. Low frequency part – contains semicircle with signs of a diffusion control mechanism characteristic to electrolyte diffusion through pores.

Numeric modeling was done by matching the parameters of equivalent circuit shown in Figure 6. Results of fitting are shown in Table 3.

Table 3. Results of numeric modeling

№	R_{p0}, Ohm	C_{hf}, F	$R_{f,}$ Ohm	C_f, F	R_u, Ohm
1	17.60	$1.4 \cdot 10^{-4}$	1274.62	$3.38 \cdot 10^{-3}$	10.61
2	22.75	$3.6 \cdot 10^{-4}$	1196.77	$1.7 \cdot 10^{-3}$	31.64
3	26.28	$7.4 \cdot 10^{-4}$	405.1	$3.4 \cdot 10^{-3}$	22.57
4	30.82	$1.1 \cdot 10^{-4}$	1255	$1.9 \cdot 10^{-3}$	22.8
5	62	$1.8 \cdot 10^{-4}$	1802	$3.7 \cdot 10^{-3}$	20.81

The dependence of specific resistance on sintering temperature resembles a curve with a minimum at 450ºC (Figure 8).

The presence of this minimum is possibly related to a simultaneous action of two processes. Decreasing of the specific resistance at sintering temperature below 450ºC is possibly due to the damage of a surface zinc hydroxide. Samples sintered at these temperatures contain small amount of zinc hydroxide that affects specific resistance. Increasing sintering temperature transfers hydroxide to oxide and the dependence changes. Above 450ºC, growth of the specific resistance is related to film morphology. Particle size growth (according to SEM analysis) results in changed pore parameters, causing difficulties in ion trespassing through pores.

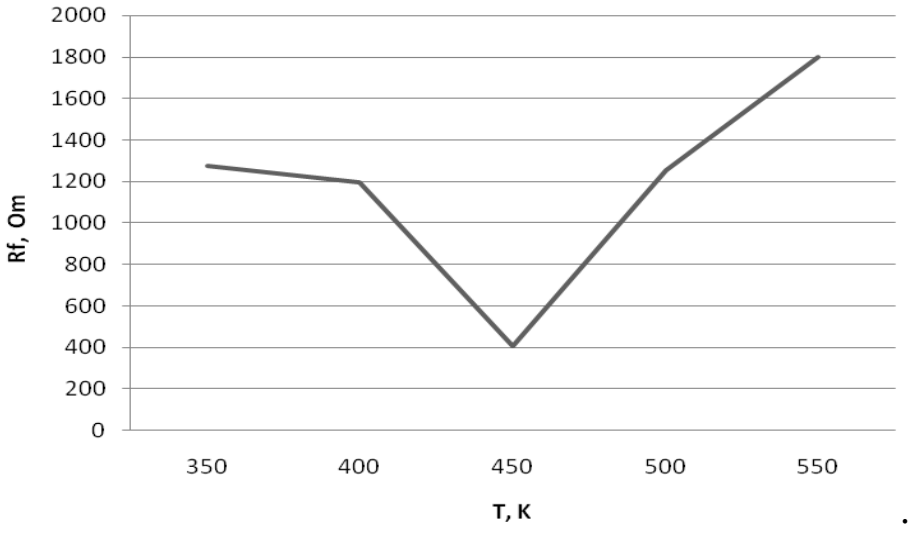

Figure 8. Dependence of the specific resistance on sintering temperature.

The diffusion coefficient was estimated from EIS data utilizing equivalent circuit model containing Warburg element [52]. For numerical fitting was used model of the insulated coating shown in Figure 9.

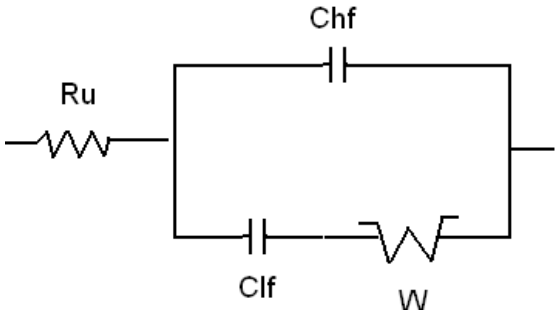

Figure 9. Electrical equivalent circuit of insulating coating with a diffusion control.

In this figure W is stated for Warburg – electrochemical diffusion element assuming capacitances and resistances connected in series, frequency dependent. This element describes mass transfer processes, including diffusion. Pores in our film were involved in charge transfer process. Numerical modeling results based on the model of insulating coating are shown in Table 4.

Table 4. Results of numerical fitting

Sintering temperature	W	C_{hf}, F	R_u, Ohm	C_{lf}, F
350°C	108.78	0.0009	23	0.0042
400°C	198.44	0.0008	23	0.0040
450°C	207.52	0.009	37	0.0197
500°C	295.54	0.0065	38	0.0038
550°C	538.16	0.00011	86	0.0086

To estimate the low frequency capacitance (C_{LF}) from at Nyquist plot, was determined an imaginary component of a complex resistance Zim at low frequency, and the dependence ZIm=F(f^{-1}) was plotted, as shown in (Figure 10). Values of the effective diffusion coefficient are shown in Table 5, and plotted in Figure 11.

Table 5. Values of the effective diffusion coefficient for different samples

№	σ_w	C_{LF}, F	T_{sint}, K	Deff, m^2/s
1	108.78	196.25	350	$6.86 \cdot 10^{-19}$
2	130.5	223.61	400	$3.69 \cdot 10^{-19}$
3	257.52	119.82	450	$3.27 \cdot 10^{-19}$
4	295.54	280.46	500	$4.55 \cdot 10^{-20}$
5	538.16	277.44	550	$1.43 \cdot 10^{-20}$

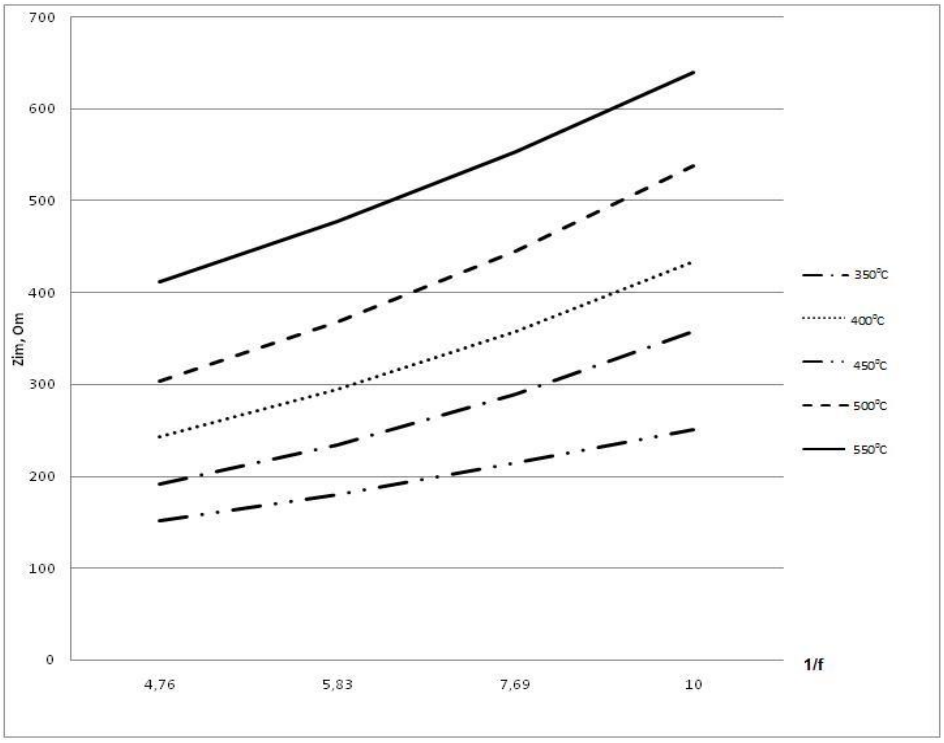

Figure 10. Imaginary part of the impedance as a function of reciprocal frequency.

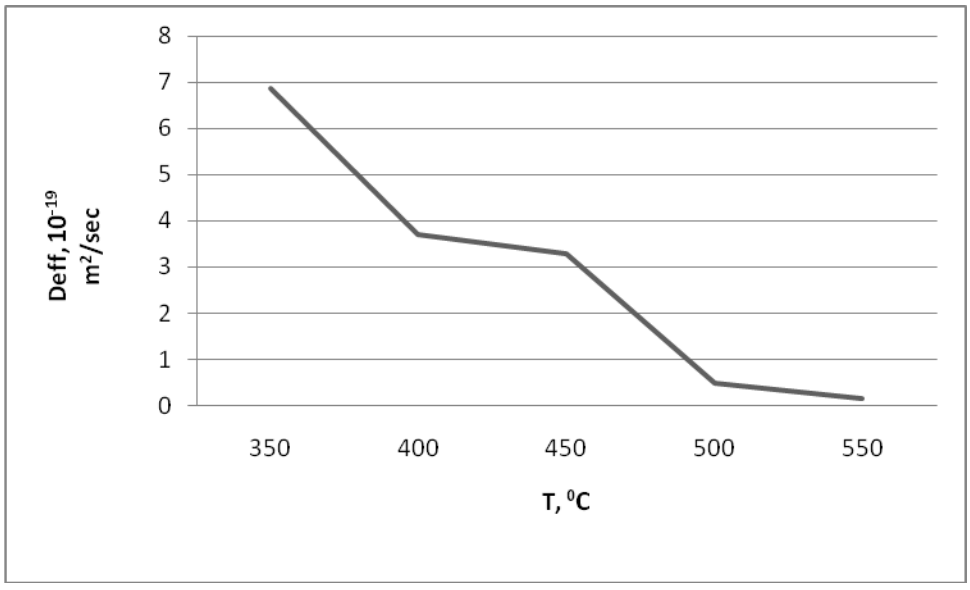

Figure 11. The dependence of the effective diffusion coefficient on samples sintering temperature.

Obtained data show that with the increase of a sintering temperature, the effective diffusion coefficient decreases. It is possibly due to the increase of the size of grains composing the film that is confirmed by SEM data. When sintering temperature increases,

and particle size changes, morphology of pores also changes in the direction of decreasing their diameter, therefore diffusion slows down.

CONCLUSIONS

Zinc oxide films obtained by sol-gel method possess porous morphology with an average pore size of 10 – 20 nm. The influence of sintering temperature on average particle size and surface area was determined. Electrolyte resistance in pores was determined by numeric fitting, and the effective diffusion coefficient was found. Sintering temperature affected parameters mentioned above. The electrolyte resistance decreased until sintering temperature reached 450ºC, than increased due changes in pore morphology. The effective diffusion coefficient decreased throughout the whole temperature range of sintering that was possibly due to decreased pore size. Membrane and catalytic properties of obtained films require further investigation.

ACKNOWLEDGMENTS

Authors express their sincere appreciation to Mr. Alexey Veselkov, for his help, and Dr. Evgeny Alexandrov for valuable discussions.

REFERENCES

[1] A.Georgibiane, A.N. Gruzincev, E.E. Yakimov, Spontaneous and stimulate ultraviolet luminescence ZnO :N at temperature 77K, *Phys. Techn. Semicond*., 39, (2005), 6.

[2] V.M. Masalov, E.N. Samarov, G.I. Volkodav, Ultraviolet luminescent ZnO filtered in opal matrice, *Phys. Techn. Semicond*., 38, (2004), 7.

[3] M. Dutta and D. Basak, p-ZnO/n-Si heterojunction: Sol-gel fabrication, photoresponse properties, and transport mechanism, *Appl. Phys. Lett*. 92, (2008), 2743-2747.

[4] A.N. Gruzincev, V.T. Volkov, K.Barthou, Spontaneous and forced radiation in thin-film nanoresonators ZnO-SiO2-Si, obtaining the method of magnetic evaporation, *Phys. Techn. Semicond*., 36, (2002), 6.

[5] A.N. Gruzincev, V.T. Volkov, E.E. Yakimov Photoelectric properties the films of ZnO, alloyed the acceptor impurity Cu и Ag, *Phys. Techn. Semicond*., 37, (2003), 3.

[6] A.N. Gruzincev,A.N. Redkin, Z.I. Makovei, Random vertical ZnO nanorods obtained by laser radiation, *Phys. Techn. Semicond*., 41, (2007), 6.

[7] A.N. Gruzincev,A.N.Redkin, E.E. Yakimov, Edge luminescence of ZnO nanorods under high power optical excitation, *Phys. Techn. Semicond*., 42, (2008), 9.

[8] Keming Zhanga, Ya-pu Zhaoa, Fa-quan Hea, Dong-Qing Liu, Piezoelectricity of ZnO Films Prepared by Sol-Gel Method, *Chin. J. Chem. Phys*., 20, (2007), 6.

[9] Huan Tonga, Bo-Lin Wangb, Zhong-Can, Ou-Yang, Electric potential generated in ZnO nanowire due to piezoelectric effect, *Thin Solid Films*, 516, 9, (2008), 2708-2710.

[10] M. W. Wolf, J. J. Martin, Low temperature thermal conductivity of zinc oxide, *Phys. Stat. Sol*. (a), 17, 1, (2006), 476-482.
[11] U. Özgür , X. Gu, S. Chevtchenko, Thermal Conductivity of Bulk ZnO after Different Thermal Treatments, *J. Electron. Mater*. , 35, 4, (2006).
[12] Lubomir Spanhel, Colloidal ZnO nanostructures and functional coatings: A survey, *J. Sol-Gel Sci. Techn*. 39, (2006).
[13] D.-G. Yoo, Fabrication of the ZnO thin films using wet-chemical etching processes on application for organic light emitting diode (OLED) devices, *Surf. Coat. Technol*., 202, 22-23, (2008), 5476 – 5479.
[14] V.Y. Rud, Polarizational photo sensitivity of solar elements ZnO/CdS/ Cu(In,Ga)Se2 *Phys. Techn. Semicond*., 33, 4, (1999).
[15] X. L. Cheng, H. Zhao, L. H. Huo, ZnO nanoparticulate thin film: preparation, characterization and gas-sensing properties, *Sensors and Actuators B: Chemical*, 102, 2, (2004), 248-252.
[16] S Jiaqiang Xua, Qingyi Panb, Yu'an Shuna and Zhizhuang Tian, Grain size control and gas sensing properties of ZnO gas sensor, *Sensors and Actuators B: Chemical* 66, 1-3, (2000), 277-279.
[17] P. Mitra, A. P. Chatterjee1 and H. S. Maiti , ZnO thin film sensor, *Mater. Letts*. 35, 1-2, (1998).
[18] V.I. Anisimkin, Analysis of air and induction surface processes with the help of surface acoustic waves, *J. Techn. Phys*., 68, 2, (1999).
[19] Ph. Luginbuhi, Acoustic Wave Device for the Translation of Microparticles, *Proc. SPIE,* 2978.
[20] H.P. Lobl, Materials for bulk acoustic wave (BAW) resonators and filters, *J. Europ. Ceramic Soc*., 21, (2001), 2633-2640.
[21] Y. Panfilov, Using the nanomaterials. *Nanoindustries*, 6, (2007).
[22] Y. Chen, D. M. Bagnall, et al. Plasma assisted molecular beam epitaxy of ZnO on c-plane sapphire: Growth and charactercterization. *J. Appl. Phys*., 84, (1998), 3912-3918.
[23] V. Tudose, P. Horvath, M. Suchea, Correlation of ZnO thin film surface properties with conductivity, *J. Appl. Phys*. A, 89, (2007), 57–61.
[24] Z.Z. Ye, H.H. Chen, R.Liu et al. Structure and PL spectrum of ZnO films prepared by DC reactive magnetron sputtering, *Chin. J. Semicond*., 22, (2001), 1015-1018.
[25] Y.F. Chen, F.Y. Jiang, L Wang, et al. Structural and luminescent properties of ZnO epitaxial film grown on Si (111) substrate by atmospheric-pressure MOCVD. *J. Cryst. Growth*, 275, (2005), 486－495.
[26] V. A. Krivchenko, D. V. Lopaev, UV Detectors Based on Nanocrystalline ZnO Films, *Techn. Phys*., 53, 8, (2008), 1065–1069.
[27] P.H. Hsieh, Y.C. Chen, C.M. Wang, Structural and photoluminescent characteristics of ZnO films by room temperature sputtering and rapid thermal annealing process, *Appl. Phys.* A 84, (2006), 345–349.
[28] L.L. Yang, Z.Z. Ye, L.P. Zhy, Y. J. Zeng, Fabrication of p-Type ZnO Thin Films via DC Reactive Magnetron Sputtering by Using Na as the Dopant Source, *J. Electron. Mater*., 36, 4, (2007).
[29] A.N. Gerihin, A.I. Hudobenko, Laser evaporation of films on silicon and sapphire carriers, *Quant. Electron*., 33, 11, (2003).

[30] A. Vincze, Preparation and properties of ZnO layers grown by various methods, *Appl. Surf. Sci.*, 255 (2008), 1419-1422.
[31] Yifa Yang, Femtosecond laser deposited zinc oxide film and its optical properties,*Vacuum*, 83, (2009).
[32] A. Djellou, R. Rabadanov, Thermochemical and Green Luminescent Analysis of Zinc Oxide Thin Films Grown on Sapphire by Chemical Vapor Deposition, *J. Phys*, 28, (2004).
[33] A. A. Engelbrecht, K. T. Roro, and R. Swanepoe, Infrared characterization of ZnO films on Si substrates, *Phys. Stat. Sol*. C, 5, 2, (2008).
[34] J.D. Ye, S.M. Gu, Substrate temperature dependence of properties of ZnO thin films deposited by LP-MOCVD, *Appl. Phys*. A 78, (2004).
[35] D. Ye, S. Guf, MOCVD growth and properties of ZnO films using dimethylzinc and oxygen, *Appl. Phys*. A, 81, (2005).
[36] K. Levine, J. Iroh and P. Kosel, "Synthesis and properties of the nanocomposite of zinc oxide and poly(amic acid)", *Appl. Surf. Sci*., 230, (2004), 224.
[37] T. Pauporte, Electrodeposited Mesoporous ZnO Thin Films as Efficient Photocatalysts for the Degradation of Dye Pollutants, *J. Phys. Chem*. C, 111, 21, (2007).
[38] M. Izaki, Room-temperature ultraviolet light-emitting zinc oxide micropatterns prepared by low-temperature electrodeposition and photoresist, *Materials Research Society Symposium - Proceedings*, (2001), 668.
[39] Lubomir Spanhel and Marc A. Anderson, Semiconductor Clusters in the Sol-Gel Process: Quantized Aggregation, Gelation, and Crystal Growth in Concentrated ZnO Colloids, *J. Am. Chem. SOC*., 113, (1991), 657-662.
[40] J. Zhang , H. Feng, W. Hao and T. Wang, Blue-emitting ZnO sol and film obtained by sol-gel process, *J. Sol-Gel Sci. Technol*. (2006).
[41] P. Hoyert and H. Weller, Potential-Dependent Electron Injection in Nanoporous Colloidal ZnO Films, *J. Phys. Chem*, 99, (1995).
[42] D. Bahnemann, C. Kormann, and M.Hoffmann, Preparation and Characterization of Quantum Size Zinc Oxide: A Detailed Spectroscopic Study, *J. Phys. Chem*., 91, (1987).
[43] B. Choi, D. Hoon, C. Yung, S. Yoon, Optical characterization of ZnO thin films deposited by Sol-gel method, *J. Mater. Sci*.: *Mater. Electron*. 17, (2006).
[44] Z. Xu, H. Deng, Juan Xie, Y. Li , Photoconductive UV Detectors Based on ZnO Films Prepared by Sol-Gel Method, *J. Sol-Gel Sci. Technol*. 36, (2005).
[45] J. Huang, Influences of ZnO sol-gel thin film characteristics on ZnO nanowire arrays prepared at low temperature using all solution-based processing, *J. Appl. Phys*. 103, (2008).
[46] H. Bahadur, A. Srivastava, R. Sharma, Morphologies of Sol–Gel Derived Thin Films of ZnO Using Different Precursor Materials and their Nanostructures, *Nanoscale Res. Letts.*, 2, (2007).
[47] J.Wang, Y. Qi, Z. Zhi, J. Guo, A self-assembly mechanism for sol–gel derived ZnO thin films, *Smart Mater. Struct*. 16, (2007).
[48] V. Musat, A.M. Rego, R. Monteiro, E. Fortunato, Microstructure and gas-sensing properties of sol–gel ZnO thin films, *Thin Solid Films* 516, (2008), 1512-1515.
[49] L. Znaidi, Preparation of ZnO Thin Films with Preferential Orientation by a Soft Chemistry Route, *J. Sol-Gel Sci. Technol*., 26, (2003).
[50] M.A. Shluger, Galvanic coatings in industry, *Nauka*, (1985).

[51] V. Antonenko, A.Vasiliev, I.Olihov, Semiconductor gas sensor, *Electronic*, 4, (2001).
[52] E.G. Tolstopyatova, S.N. Sazonova, V.V. Malev, V.V. Kondratiev. Electrochemical impedance spectroscopy of poly(3-methylthiophene) and poly(3-octylthiophene) film electrodes, *Electrochimica Acta*, 50, (2005), 1565 – 1571.

Smart Nanocomposites
Volume 1, Issue 1.
ISSN: 1949-4823

STRUCTURAL AND PHYSICO-CHEMICAL CHARACTERISTICS OF SHUNGITE NANOCARBON AS REVEALED THROUGH MODIFICATION

N. N. Rozhkova*[1], G. I. Emel`yanova[2], L. E. Gorlenko[2], A. Jankowska[3], M. V. Korobov[2] and V. V.Lunin[2]

[1]Institute of Geology, Karelian Research Centre RAS, Petrozavodsk, Russia
[2]M.V.Lomonosov Moscow State University, Department of Chemistry. Moscow, Russia
[3]Wroclaw University of Technology, Institute of Chemistry and Technology of Petroleum and Coal, Wroclaw, Poland

ABSTRACT

Shungites could be regarded as a natural source of nanocarbons. Basic structural units (BSU) of shungite carbon (ShC) is smaller than 1 nm in size and has a form of curved graphene cups that stack together under the influence of surface forces composing globular aggregates > 6 nm. Changes in packing of BSU in aggregates provide difference in activity of ShC (surface area, porosity and surface properties) depending on natural and artificial processes undertaken. Thermal activations with steam and ozonization at room temperature applying to ShC increase its total porosity.

Micro- and mesopores were mainly developed under steam treatment, otherwise ultramicropores and mesopores predominantly increase on ozonization. Structural reconstruction of ShC was observed in both cases. The most pronounced effect of ShC activation, namely releasing of the BSU, was reached when it was transferred into the form of stable aqueous dispersion.

Keywords: Nanocarbon, Shungite, Microporosity, Activation.

1. INTRODUCTION

A steady interest in carbon from shungite rocks shown by scientists for over two centuries is due to the importance of the study of new structural forms of carbon and its discussable origin. Precambrian shungite rocks that contain one of the oldest noncrystalline

* Corresponding author: Natalia N. Rozhkova. Institute of Geology, Karelian Research Centre RAS, Petrozavodsk, Russia; Tel: 007 8142 780189. Fax: 007 8142 780602. e-mail:rozhkova@krc.karelia.ru

carbon, dated at ~2 Ga, are widespread in Karelia (Russia). Shungite carbon penetrates practically all rocks of the region over an area in excess of 9000 km^2, and its resources are estimated at $25 \cdot 10^{10}$ t [1].

Based on the percentage of carbon, which varies from less than 1% to 98 wt.%, shungite rocks were subdivided into five types [2], types I and III being the most interesting. Type I of shungite rocks that occurs in the Shunga deposit (Sh-1Sh) contains almost pure vitreous carbon (96—98 wt.%) with traces of other elements (0.1—0.5% H, 0.6—1.5% O, 0.7—1.0% N and 0.2—0.4 % S). Rocks of this type occur as small veins and inclusions. They are of no commercial value, but are widely used in research as a standard of shungite carbon (ShC). Shungite rocks of type III that contain about 30 wt.% of carbon (Sh-III) are most common. The Zazhogino and Maksovo shungite deposit are of commercial value and are now being mined. In addition to carbon and a mineral phase (quartz and alumosilicates), shungite rocks typically contain admixtures of catalytically active compounds of metals of I and VIII groups, and a small quantity of dissolvable organic matter represented by aliphatic-series compounds, primarily saturated, branched-structured ketones and ethers with traces of aromatic compounds. The organic matter extracted from shungite of type III has a yield of 0.011—0.025 wt % [3]. Data obtained by the X-ray and electron diffraction methods show that multi-layered globular or ellipsoid particles, from 6-10 nm in size, with an internal cavity form the structure of ShC. In the general case, domains of coherent scattering correspond to those of a single-type arrangement of layeres of globular elements, and layers with considerable distortion that provide a link between the globules form an arbitrary net [4, 5].

ShC complex organization at a nanoscale of 1-100 nm has been recognized recently by summarizing results of different methods (HRTEM, SAXS, AFM, SANS) applied to ShC study [5, 6, 7]. Since the characteristic units in the form of curved graphene stacks 0.5-1.0 nm in size were registered in both original and treated ShC samples, it was confirmed that the units were not synthesized under treatment. They were regarded as the basic structural unit (BSU) that participated in construction of the structural levels of ShC (Figure .1).

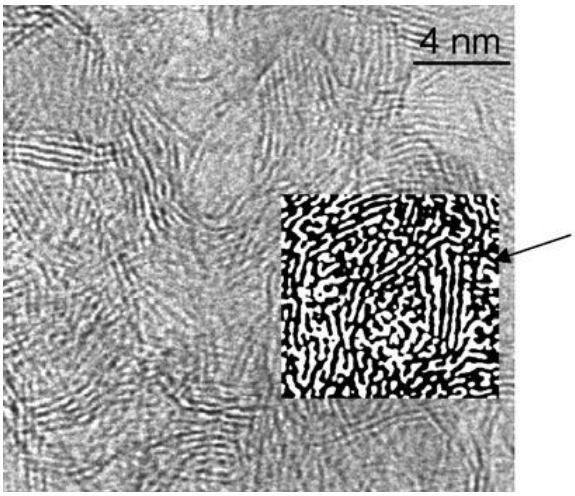

Figure 1. TEM image shows packing of ShC globules and their fragments. Contrast imprint of the image by HRTEM (insertion) arrow points to a pore between carbon stacks (basic structural units) filled with non-structured fractal carbon.

The revealing of fullerenes in shungite rocks by HRTEM and mass-spectrometry methods provided a new impetus to the study of ShC [8]. Extraction experiments were conducted using conventional organic solvents, but they did not shed light on the occurrence and concentration of fullerenes in shungites [9]. It should be noted that all the above studies were based on the assumption that fullerene bonds in ShC have a molecular pattern. A great attention has been given lately to the study of covalent and donor-acceptor fullerene compounds that result from interaction with nucleophilic molecules. It should also be noted that trace amounts of C_{60} are extracted from ShC by the colloid extraction method using polar solvents [10]. In this connection, the problem of the conditions of formation and conservation of fullerenes and fullerene-like structures in a natural environment arose again [11, 12]. For example, a globule of ShC was found to be morphologically similar to that of fullerenes in having an internal cavity and a two-dimensional hexagonal cell of carbon atoms with a characteristic anisotropy of distortions, which reduces its symmetry to trigonal [13].

ShC is a nongraphitized carbon (it is not graphitized at 2800 °C). However, the restructuring-modification of nanostructural elements observed in the case of external effects shows that ShC is metastable. As a result of thermal treatment and fine grinding, globules murge to form large, empty, predominantly polyhedral particles [14,15]. The restructurings described for carbon soot particles are similar, but they occur at higher temperatures (1200 and 2800 °C for ShC and soot, respectively) [16]. Nanodimensional carbon particles (giant fullerenes, onions and nanotubes) that occur as layered structures with a distance of 0.35 nm between graphite-like planes have been revealed in ShC powder [15]. Multi-layered, spheroidal carbon particles, 100 nm in diameter, form carbon chains on the surface of the quartz grains of lydite (shungite rock with 3 wt% of carbon). These aggregated nanoparticles were separated by autoclave dissolution of quartz in lydite and displayed high activity [17].

In spite of structural similarity, shungites from different deposits differ in bulk morphology [14]. It should be noted in this connection that shungites of type I from different deposits are subdivided into highly porous (Nigozero and Maksovo deposits) and poorly porous (Shunga and Chebolaksha deposits).

Scientists are not unanimous as to the origin of ShC and its structural constituents [2, 18]. This problem could be approached by assuming that a difference in morphology reflects a difference in the conditions of one or another variety formation, in particular the environment in which ShC was formed. Available geological evidence suggests that the shungite complex has arisen from large-scale hydrothermal activity but under relatively mild conditions: at a temperature of not more than 450 °C and a pressure of 700 MPa [19].

The structure of shungites is distinctive in that because the interphase boundary between carbon and silica, the main constituents of shungite rock, is highly developed, these phases form interpenetrating nets. Therefore, each micron particle of the powder from shungite rock of type III has carbon and mineral constituents [20].

As ShC is a highly porous and highly durable substance with a well-developed surface, it is used for many purposes [21]. Owing to its high chemical resistance, typical of glassy carbon, and activity, characteristic of coke, ShC can replace various carbon materials. However, shungite treatment regimes, in which stable properties characteristic of glassy carbon and/or coke can be obtained, have not yet been determined. The main obstacle is connected with the unsolved task on stability of the basic structural unit (BSU) of ShC which predetermines its reactivity and structural organization (Figure 1).

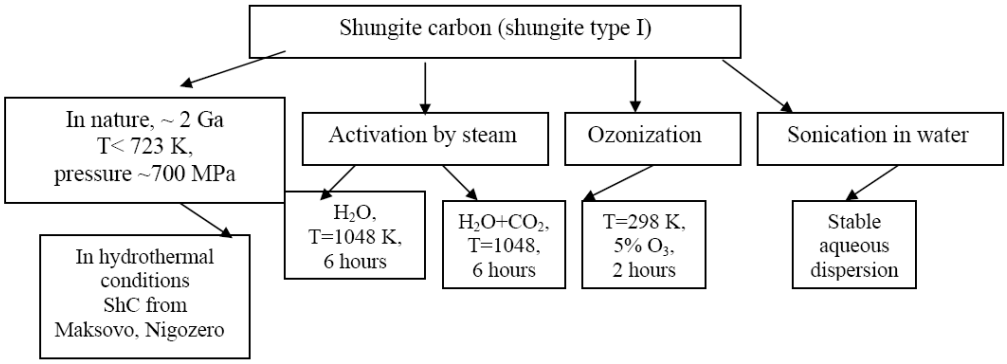

Figure 2. Scheme of shungite carbon modification.

Assessing the activity of ShC as an adsorbent, catalyst and filler, it should be noted that if the maximum achievable dispersity of ShC (average size of particles) depends on the size of the BSU and its aggregates (globules), then specific surface and the number as well as distribution of functional groups on the surface can be varied by selecting corresponding treatment conditions. Thermal treatment in inert atmosphere does not change the structural parameters of ShC and does not affect the specific surface and concentration of paramagnetic centres up to a temperature of 1000 °C [22]. At the same time, thermal treatment in an oxidative or reducing atmosphere and hydrothermal treatment of ShC are efficient. Of special interest are some methods used to nonconventionally modify the properties of carbon materials, such as low temperature ozone oxidation and disintegration in aqueous media under ultrasonic treatment. The results and use of the above methods to modify the properties of ShC are discussed in the present paper.

2. EXPERIMENTAL

To conduct the study, we collected carbon-rich shungite rock samples with 90-98 wt% carbon from several deposits: shungite rocks of type I from the Shunga deposit, 96-98 %C (ShI-Sh), and the Maksovo deposit, up to 90 %C (Sh-IM). Both fine shungite powders (with particles size less than 50 μm) and coarse grains (3-6 mm) were prepared by dry grinding. The characteristics of carbon from the above deposits are described in detail in [4, 5, 7]. Their composition and some physicochemical parameters are presented in Table I. The scheme of the possible ways of ShC modification is shown in Figure 3.

Thermooxidative activation of ShC by overheated steam was conducted under flow conditions in the temperature range of 1048—1198 K. Steam flow intensity was 2.5 10^{-5} $m^3/(m^2$ sek). Steam volume was 240 g/h and (169 m^3/h + 129g/h) for H_2O and the mixture (H_2O+CO_2), respectively. The effect of steam treatment conditions on the extent of burning-out, surface area and porosity of ShC was determined.

Oxidation of shungite samples by ozone was carried out at flow rate 5-12 l/hour and 20-60 ^{0}C. Ozone was synthesized under barrier electrical discharge from oxygen (high purity). Ozone content in the mixture was 2-5 vol%.

Table 1. Composition and some properties of shungites type I

Parameters	Sh-ISh	Sh-IM
Carbon content, %	96—98	90
H/C, at. fraction	0.034—0.063	0.102—0.110
Bulk density, g/cm^3	1.90	1.79—1.85
Porosity, %		
open	4.7	18.8
closed	8.1	6.6
microporosity	67	96
Specific surface area (BET), m^2/g	2—5	180—240
Pore size, nm	4—6	3

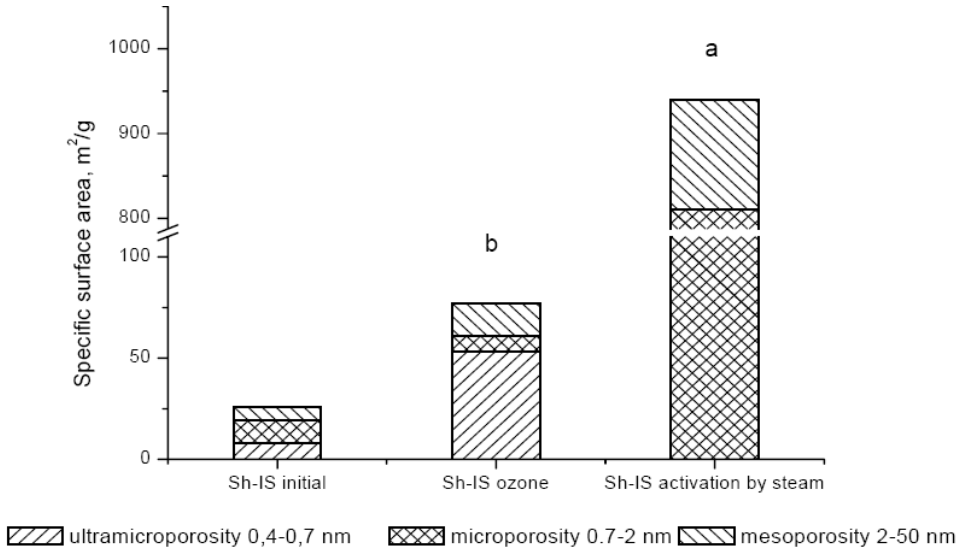

Figure 3. Bar chart of porosity of shungite carbon: activation by steam at 1173 K, ozonization at 293K for 2 h.

Aqueous dispersion was prepared from a powder (with particles <40 μm in size) of shungite type I (Shunga deposit) using ultrasonic treatment as described elsewhere [10].

Surface area of the samples was determined by BET (nitrogen desorption) method before and after modification. Electron microscopy and electron diffraction were used to determine structural characteristics of modified ShC. Electron micrographs were made in the transmission mode and selected-area electron diffraction (SAED) was carried out using a *TlCl* standard on the EM-25 electron microscope as reported elsewhere [5].

To assess the effect of treatment on the adsorptrive properties of shungites, adsorbates (benzene, CO_2 and water) that differed in characteristics were used. Measurements were taken using vacuum gravimetric apparatus at 298 K. The parameters characterizing the porosity of shungites were determined from the adsorption isotherms as described in [23,24]. Time-stable aqueous dispersions were analyzed before and after treatment by dynamic light scattering (DLS) using a PhotoCor-SP photon correlation spectrometer. Control for admixtures in aqueous dispersions was carried out using atomic absorption spectrophotometer Perkin-

Elmer, 703. Small angle X-ray scattering (SAXS) was carried out to estimate influence of treatments on dimensions of ShC structural elements using an automated Rigaku Geigerflex diffractometer with D-Max system equipped over the range of scattering angles 0.5-10^o as elsewhere [6].

2.1. Thermooxidative Activation of Shungite Carbon by Steam

A high conversion (high activation) of Sh-1Sh under steam treatment (Table 2) suggests a substantial contribution of hydro-activation to this process whereas ShI-M underwent hydrothermal influence in nature. One can see that as a result of activation, the specific surface of shungite Sh-1Sh increases by 25.7 times whereas that of shungite Sh-1M increases by 3.4 times. The maximum specific surface values, obtained by thermal oxidation of shungites from these deposits (548 m^2/g for Sh-1Sh and 587 m^2/g for Sh-1M), are comparable with the maximum specific surface values of natural shungite samples from the Nigozero deposit (450—600 m^2/g), which seems to have exposed thermooxidative activation under natural conditions. Addition of carbon dioxide to the oxidizing mixture makes ShC burn out more intensely and does not have a considerable effect on the value of specific surface. Thus, as a result of treatment of Sh-1Sh at 1048 K for 6 h by a steam-CO_2 mixture, the specific surface area has increased to 544 m^2/g, whereas treatment by steam under the same conditions has increased the specific surface to 502 m^2/g.

Thermooxidative activation resulted in increase of total porosity and mesoporosity of ShC whereas microporosity increased slightly (see bar chart in Figure 3a). Increase in mesoporosity was supported by TEM images of activated ShC (Figure 4a). Many particles after hydrothermal activation have spherical ~100 nm pores extrinsic for initial ShC. But only in ShC treated with the H_2O+CO_2 steam a homogeneous nondefective film 20-30 nm in thickness (Figure 4b), which SAED parameters corresponded to ShC, was detected (Table 3). Two different in properties structures were observed in ShC after thermooxidative activation.

Table 2. Effect of steam activation on the surface area of shungites

Treatment conditions	Sh-ISh		Sh-IM	
	Yield, %	*S*, m^2/g	Yield, %	*S*, m^2/g
H_2O-1048 K, 300 min	42.8	<2.7/437.6**)	46.0	185.6/634.0**)
*) 1098 K, 120 min	67.8	370	60.5	504
*) 1148 K, 120 min	12.5	548	37.4	587
*) 1198 K, 120 min	0	-	5.7	207
H_2O-1048 K, 360 min	58.9	380		
H_2O-1098K, 360 min	26.9	502		
CO_2+H_2O-1048K,300 min	84.4	171		
CO_2+H_2O-1098K,300 min	37.3	544.3		

*) Consecutive heating of the same sample.

**) initial sample/ after treatment.

Surface area was determined by iodine adsorption.

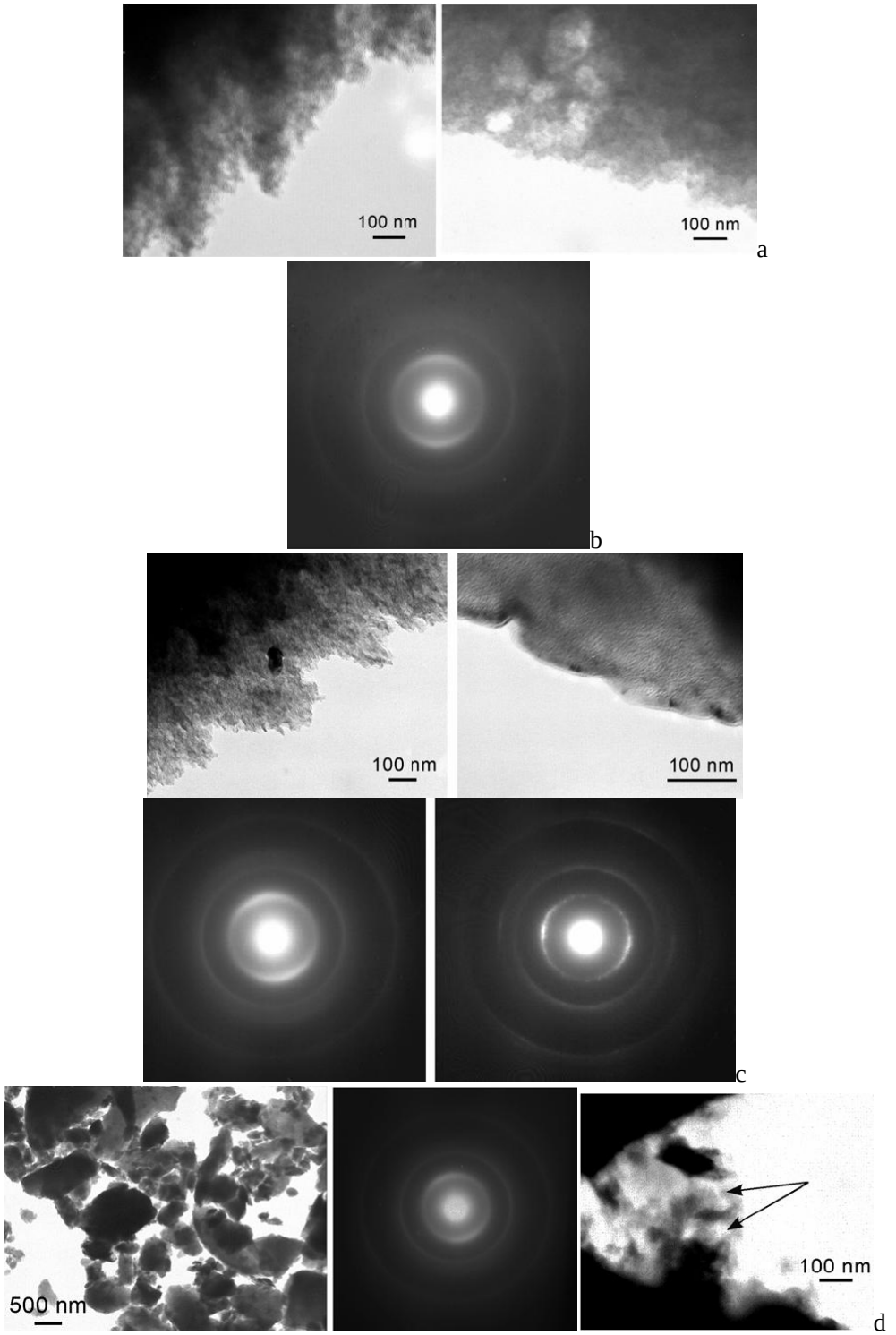

Figure 4. TEM images and corresponding SAED patterns of ShC microstructures: a). initial sample; b). ShC after activation in steam at 1048 K; c). a film detected after steam (H_2O+CO_2) at 1048 K treatment. d). ShC after ozonization.

Table 3. Changes in structural parameters of shungite carbon under treatment

Initial ShC		ShC after steam (CO_2+H_2O, 775ºC) treatment		ShC after steam (H_2O, 775ºC) treatment		ShC after ozonization	
d(Å)	FWHM	d(Å)	FWHM	d(Å)	FWHM	d(Å)	FWHM
3.51	7.2	3.49/3.44*	7.0/5.0	3.49	7.5	3.50	8.7
2.08	6	2.11/2. 10 1.74/1.71	6.0/5.5	2.12	5.0	2.07 1.71	5.2
1.21	-	1.23/1.22	11/10-	1.225	9.0	1.21	

FWHM- apparent full width at half maximum.
*) two phases: the main/the film.

Shungite modified by steam at 1048 K is characterized by the presence of particles, from 50 nm- to more than 3 μm in size, and SAED parameters are shown in Table 3. Typically edges of the particles are not uniform that differs them from original samples and is an evidence of a significant surface transformation (Figure 4 c). Some particles have spherical pores up to 100 nm that are not observed in original shungite but are similar to the pores that formed under ozonization (Figure 4d).

Development of pore structure of modified ShC was studied by SAXS. SAXS curves of shungites were discussed in [6,7]. The first peak on the diffraction curve ($2\theta_{Br}$ =13.23^o corresponding to 0,389 nm) is maximum for steam treatment, weaker on ozonized shungite and is practically absent upon treatment by H_2O+CO_2 mixture. This size coincides with that of the ultramicropores produced on modified samples by adsorption methods (Table 4).

Activation of ShC changes its fractal dimension considerably and gives rise to a volumetric pore network that penetrates the ShC structure (fractal dimension 1.88 and 1.74). The results obtained are in good agreement with the data determined by adsorption methods and electron microscopy.

Table 4. The sizes of clusters for modified shungite carbon determined by SAXS method

Samples and treatments	Fractal dimension (D)	BSU, nm	Size of the clusters, nm
ShungiteI (original)	2.20	0.51	6.0-4.5., 13.0; ≥30.2;
Shungite I (ozonized)	2.19	0.507	0.39, 2.6, 4.5-5.8, 25.0-26.5
Activated in steam (H_2O)	1.88	0.507	0. 39, 2.2, 4.5-5.2, 30.5
Activated in H_2O +CO_2	1.74	0.507	2.2, 4.5-5.2, 25.0-26.5
Dried Aqueous dispersion		Thin layer Thick layer	4.7; 9.4; 7.7; >30.1 7.7; >30.1

2.2. Low Temperature Ozone Modification of Shungite Carbon

The specific kinetic curves obtained on ShCI–Sh and ShCI-M ozone oxidation are typical for the oxidation of ShC powders: a rapid transition to a stationary ozone consumption conditions, ozone being almost completely absorbed, and the non-stationary oscillation

kinetics of CO_2 formation uncommon to any other carbon materials oxidation [25]. The amplitudes of oscillation differ from one shungite to another, and depend on the particle sizes and macrokinetic parameters, such as contact time, ozone concentration and temperature. The development of the oscillation mode is assumed to be related to the distinctive structure and properties of ShC, which obviously catalyses the oxidation of the CO, formed on the surface, to CO_2 [26].

Such kinetic self-oscillations of the rate of CO oxidation on Pd/zeolitic catalysts are related to the periodic oxidation and reduction of active centres on the surface of the catalyst. The aperiodicity of oscillations often arises from deceleration upon the intradiffusional control of the reaction. This seems to be the most probable reason for the effect observed, considering the morphological characteristics of ShC [27].

The effective rate constants estimated for the conditions close to ideal displacement (reaction first-order in ozone), at 293 K were 0.1 10–3 mol/(s·•cm3) for Sh-1M and 5.5•10–3 mol/(s•cm3) for higher-carbon Sh-1Sh. The activation energy of the process is 33±2 κJ/mol. Depending on experimental conditions (temperature, ozone concentration) and the type of the shungite, the quantity of the carbon, which does not react with ozone, is about 20%. The loss of activity was most likely related to the formation of the structurally ordering of ShC which sterically hindered the further penetration of ozone. It could be compared to the nondefective film that was detected after H_2O+CO_2 steam activation on the ShC surface (see Figure 4c).

Note that freshly prepared ShC powders are highly reactive towards ozone, and the kinetics of the reaction has a well-defined oscillatory character. Relaxation processes begin, the kinetics of oxidation becomes more stable and the amplitude of oscillations of the rate formation of CO_2 substancially decreases for ShC powders during a year.

The modification of ShC by ozone is accompanied by changes in its structural and physicochemical characteristics. As a result of ozonization, the specific surface and porosity of shungites increase (Figure 3, Table 5).

Ozonization of shungite powder (Shunga) (Table 4) allowed us to establish increase in ultramicroporosity similar to the values observed by SANS on natural shungite samples from Maksovo [7].

Pores on the second structural level (with a characteristic radius of ca.10 nm) have an internal fractal structure built by particles whose sizes are beyond SANS resolution, ca.1 nm [7]. Scatters of two sizes were determined: at 2.6 nm, 4.5-5.8 nm and one more characteristic range at 25.0-26.5 nm. The coherent scattering domain, controlled for all samples, was 3.4 nm in size. If scatters are understood as pores formed upon ozonization, then the sizes of the scatterers obtained are in good agreement with the data obtained by adsorption methods. The absence of changes in macroporosity shows once more that fractal size remains practically invariable (D = 2.187**)** upon ozonization (Table 4).

Two minimum sizes: a small peak in the range of $2\theta_{Br} = 13.23^o$ corresponding to 0.389 nm and $2\theta_{Br} = 10.14^o$ – to 0.507 nm, are obvious. The first peak on the diffraction curve is maximum for steam treatment, weaker on ozonized shungite and is practically absent upon treatment by H_2O-CO_2 mixture. This size coincides with that of the ultramicropores obtained on modified samples by adsorption methods (Table 5). On the ozonized shungite the second peak is more distinct than the peak observed upon steam treatment and decreases substantially upon activation by the H_2O-CO_2 mixture.

Table 5. Changes in porosity after ozonization of shungite carbon

Samples	Ultra micro-pores, Surface, m^2/g /Volume, cc/g	Micropores Surface, m^2/g/ Volume, cc/g	Mesopores, Surface area, m^2/g /Volume, cc/g					Total porosity Surface, m^2/g/Volume, cc/g	Pores parameters calculated on	
			Pores diameter, nm						BET*	DR **
	<0,4	0,4-2	2-3	3-5	5-10	110-50	2-50			
ShI-Sh initial	8/0.003	11/0.004	1.4/ 0,001	2.0/ 0.002	1.8/ 0.005	1.7/ 0.016	6,9/ 0,024	25.9/ 0.031	11/ 0.004	13/ 0.005
ShI-Sh ozonized	53/0.020	8/0.003	3.4/ 0.002	3.7/ 0.005	5.8/ 0.016	2,9/ 0,028	15.8/ 0.051	76.8/ 0.074	14/ 0.005	60/ 0.023

*- benzene, **- carbon dioxide, DR- Dubinin-Radushkevich.

To assess the effect of ozone treatment on the adsorptrive properties of shungites, adsorbates (C_6H_6, CO_2 and H_2O) that differed in characteristics, were used. The isotherm for H_2O adsorption on initial ShC (Figure 5a) is slightly convex toward the axis of abscissa, which is characteristic of weakly polar surfaces containing micro- and mesopores.

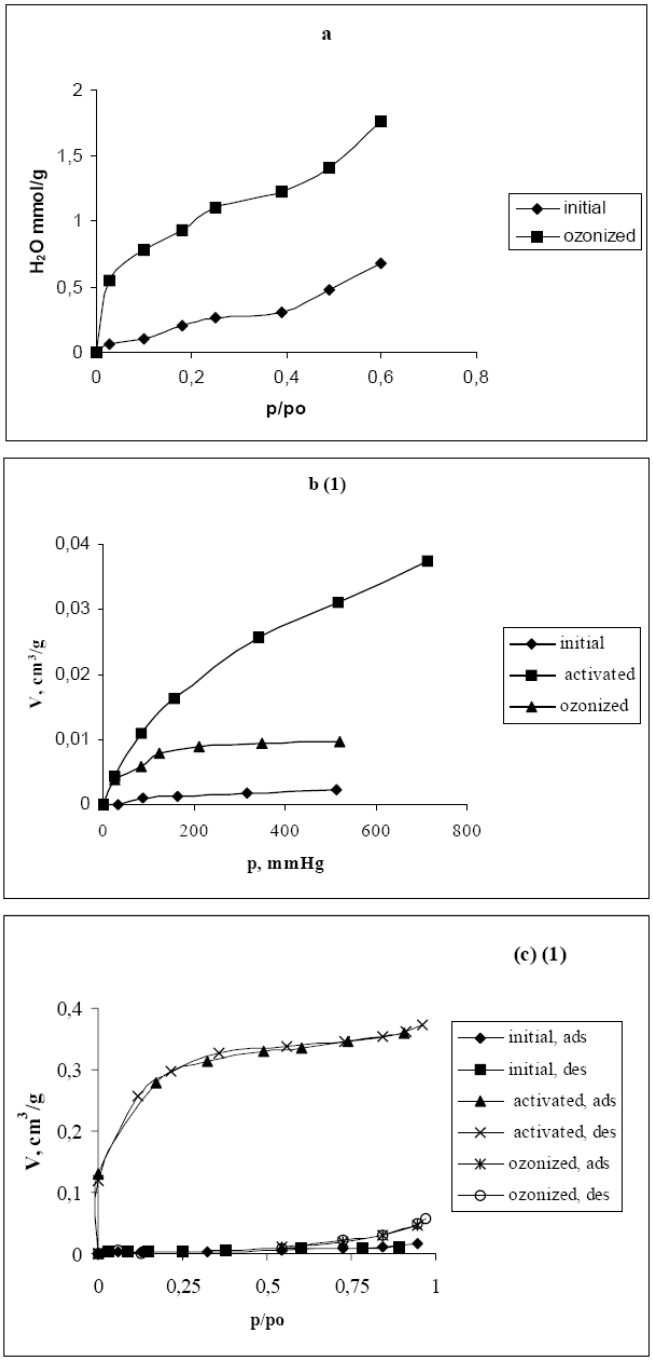

Figure 5. Adsorption-desorption isotherms on the original and treated ShC at 293 K: a). H_2O vapour adsorption on ShC; b). CO_2 vapour adsorption on ShC (1), c). benzene vapour adsorption on ShC (1).

After ozonization the H_2O adsorption value rises rapidly at low pressures and the quantity of micropores on the surface increases. The CBET constant rises from 8.1 for initial samples to 38.0 for ozonized samples.

Total pore volume measured from H_2O and CO_2, adsorption after ozonization is much greater than that estimated from C_6H_6 adsorption (Figure 5 b,c). The quantity of micropores calculated from water adsorption is 3-4 times higher than the initial value, and the quantity estimated from CO_2 adsorption is 6 times the original value (the specific volume of micropores was 0.001cm^3/g initially and 0.006 cm^3/g after ozonization). The latter result shows that along with the growth of the polar properties of the surface, the chemosorption of CO_2 takes place. The quantity of adsorbed C_6H_6 after sample ozonization is twice as much. As a distinctive type of adsorption involving π-bonds is characteristic of benzene, it is obvious that the number of such bonds increases upon ozonization. This result is also supported by IR-spectral data, which show that the number of conjugated C=C and C=O bonds on the surface of ShC increases upon ozonization [25]. The absence of a marked hysteresis loop on the C_6H_6 adsorption isotherm at p/po > 0.6 points to a small contribution of mesopores to the total volume of shungite pores even after ozonization.

Pores of 20-50 nm in size are clearly seen in TEM images of ShC after ozonization (Figure 4d). A diffraction pattern of the ozonated ShC were characterized by broadening of the first diffraction peak (002), i.e. changes in apparent full width at half maximum (from 0.72 to 0.87 nm) [5]. It is indicated the smaller size of the coherent scattering area in direction perpendicular to graphenes layers. In other words, increase in structural porosity at the nanolevel is proved.

Ozonization of ShC resulted in substantial increase in ultramicroporosity (0.4-0.7 nm) and mesoporosity. Pore distribution pattern is shown in Figure 3b.

Thus, the use of ozone as a modifying oxidant is efficient for directional affecting of the structure and physicochemical properties of ShC even at low temperatures.

2.3. Stable Aqueous Dispersion of Shungite Carbon Nanoclusters

Shungite carbon (ShC) could be converted into the form of stable aqueous dispersion without using surfactants (Figure 6). Concentration of the initial dispersions prepared by ultrasound treatment of the original shungite was ~ 0,1 mg/ml. The dispersions after centrifuging contain clusters with characteristic sizes: r = 50 ± 5 nm as determined by DLS method. Serial of ultrasound treatments as well as acid treatment were undertaken to removing of mineral admixtures of shungite carbon and decreasing of an average size of nano-particles. But the first method (the serial of ultrasound treatments) is not accompanied by oxidizing of ShC (table 6).

The removing of admixtures was supported by absence of dotty reflexes in SAED patterns. Morphostructure of precipitates is characterized by predominance of smaller particles 20-100 nm. It was compared to solid phases precipitated from saturated aqueous fullerene dispersions. The globules of the precipitated fullerene dispersions have fairly distinct boundaries with size from 20 to 70 nm (Figure 7a,b). New fullerene-bearing solid phase in the samples after slow evaporation of the aqueous colloidal solutions at ~1^oC was revealed by TEM and SAED methods (Figure 8a,b). The phase displays a finely crystalline

structure and is similar for both fullerene and shungite aqueous dispersions in formation pattern and morphostructure [28].

Table 6. Sizes of particles in aqueous dispersions based on DLS data

Sample	Concentration, mg/ml	Average radius, nm	Polydispersity	pH
Sh I initial	0.09	96.9	0.28	6.4
Sh I (USound 6)	0.07	50.0	0.20	6.2
Sh I* after acid treatment ShC particles aggregated and precipitated				
Sh I* ozonized.2 h, USound treated; In three months	0.16	 95 59	 0.29 0.47	2.31
Sh I* ozonized.4 h, USound treated; In three months	0.26	 86 53	 0.40 0.51	2.29
Sh I* ozonized 15 h, USound treated; In three months	0.72	 79 89	 0.47 0.46	2.19

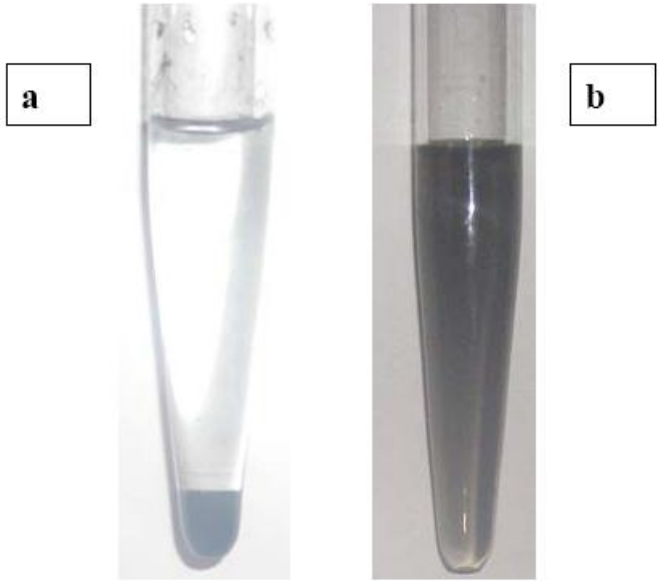

Figure 6. Aqueous dispersion of shungite carbon a) initial, b) stable

The acid treatment and further ozonization of shungite (method 2) resulted in transformation of NP into water and stabilizing them without admixtures of noncarbon crystals. Furthermore, the treatment leads to formation of stable dispersion with higher concentration of nano-particles and prevented from aggregation for several months (Figure 9). However, pH value of the dispersion decreases greatly to 2.19 (Table 6). An average particle size decreases to 79 nm (DLS data) and to 20 nm (TEM data, Figure 9c).

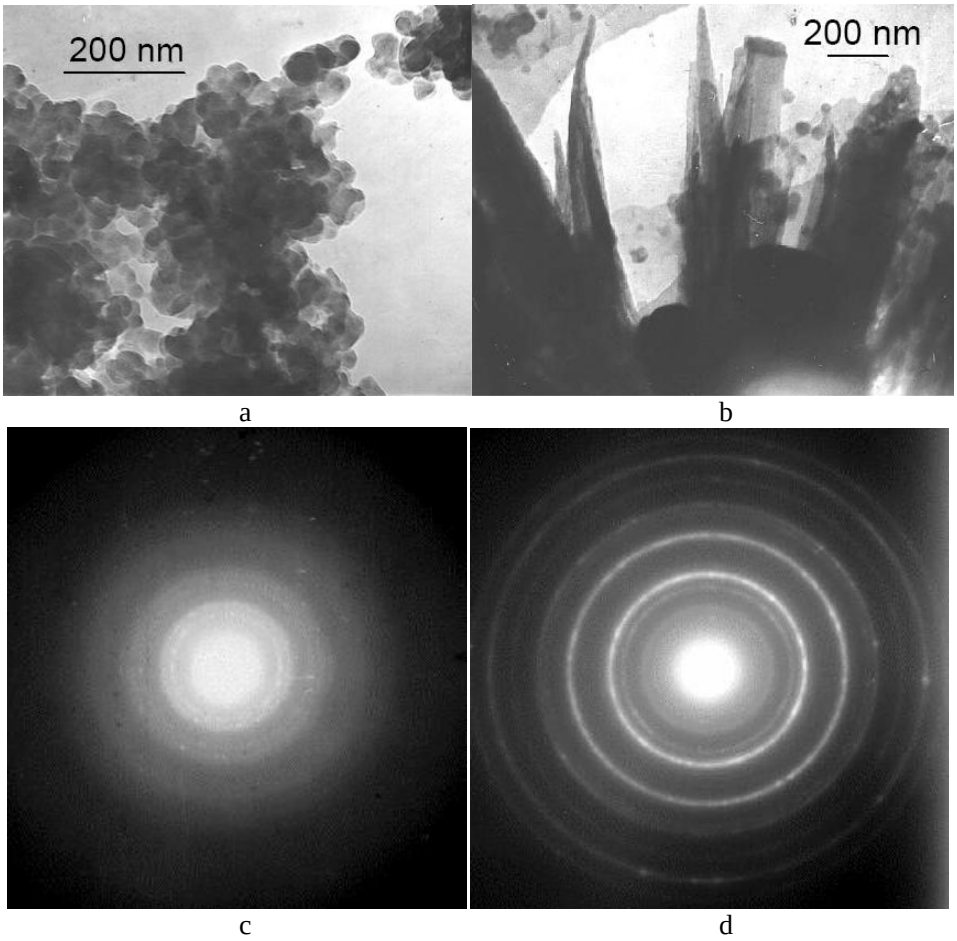

Figure 7. TEM images (a,b) and corresponding selected area electron diffraction (SAED) patterns (c,d) of the microstructures precipitated from aqueous colloidal solution of fullerenes at room temperature (a,b,c,) and at ~1ºC (d).

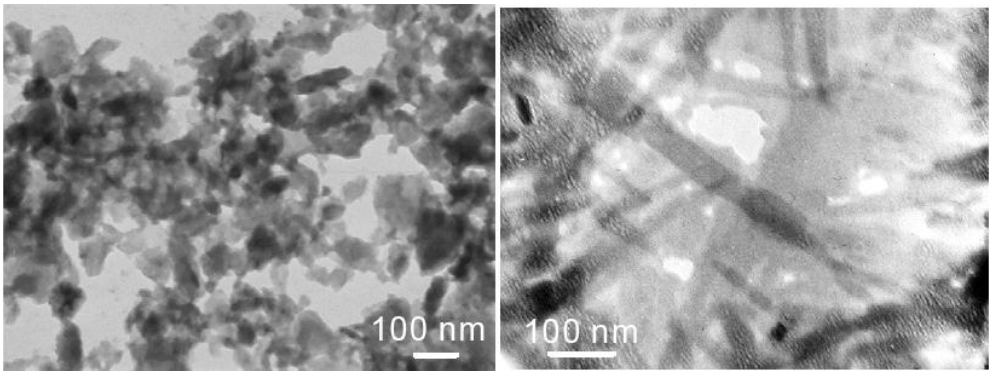

Figure 8. TEM images (a,b) of the typical microstructures of shungite colloid: a-aggregates of ShC nanoparticles, b- whiskers.

The treatments allow to remove admixtures that were supported by absence of dotty reflexes in SAED patterns (Figure 8b). Morphological structure of precipitates is characterized by predominance of smaller particles 20-100 nm (Figure 9c).

Electron diffraction studies have shown that the mineralogical composition of the particles is also fairly homogeneous and is represented by ShC; no crystalline impurities have been observed. The interlayer distances of the precipitated carbon are close to those of original shungite, although, have higher value d_{002}. At the same time, the half-width of the first maximum *(002)* is larger, which shows that coherent scattering domains decrease in size in *"c"*-direction (Tables 7 and 3).

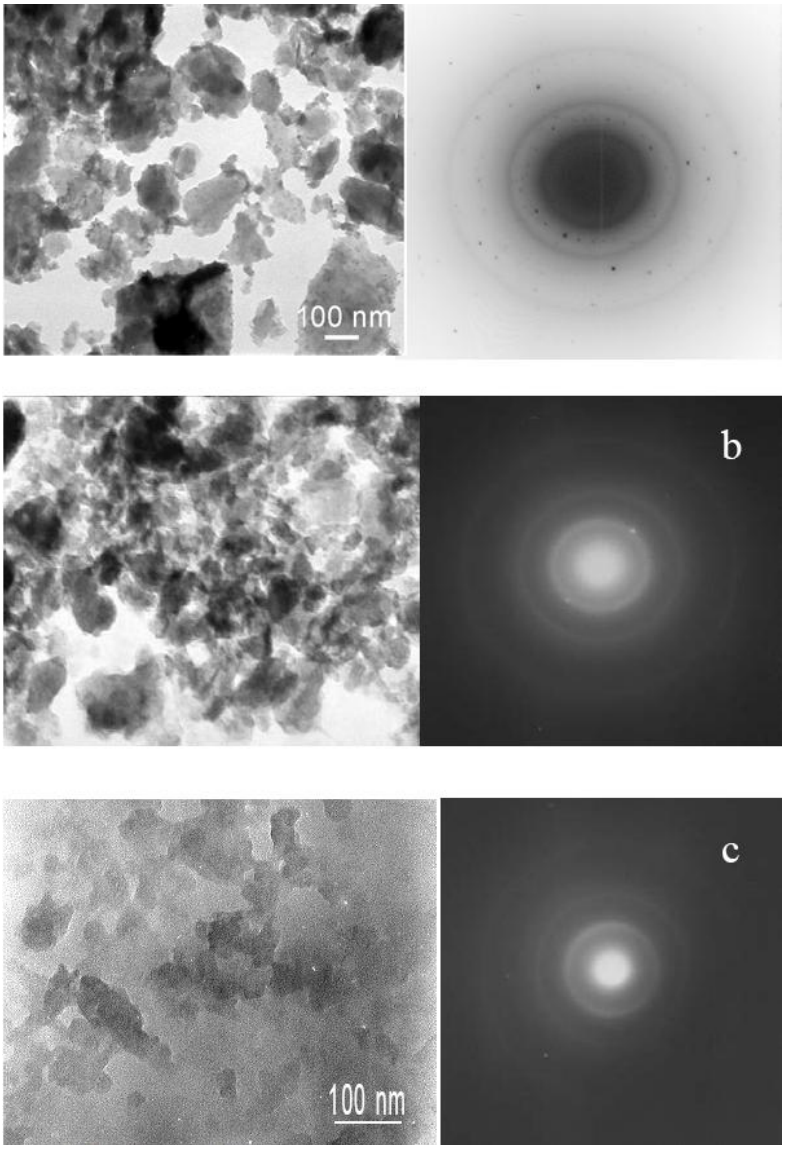

Figure 9. TEM images and SAED pattern of ShC; original (a); of the precipitates of shungite colloid products subjected to ozonization (b) and multiple ultrasound treatment (c).

Table 7. Interlayer distances, FWHM and size of the particles obtained on the precipitated products of aqueous dispersions of shungite

Aqueous colloid of ShC ozonized			Aqueous colloid of ShC treated by ultrasound		
d(Å)	FWHM	Size of the particles (nm)	d_{002} (Å)	FWHM	Size of the particles (nm)
3.52	8.7	20-100	3.52	8.2	20-200
2.11	5.7		2.11	5.6	
1.23			1.23		

Using SAXS method we could distinguish the same characteristic sizes in the nanoscale range (Table 4). Progressive increase in scattered intensity approaching the primary beam could be observed at $2\theta_{Br}=17^{o}$ that supposed to have the origin of BSU of ShC ~0.5 nm [29]. There are two more pronounced sizes: less than 10 nm (4.7; 7.7 nm) characterising globular structural units of shungite [4] and their aggregates (>30 nm) that were revealed by atomic force microscopy [17]. The minimal element of ShC characterizing by nonplanar structure is easily transformed into aqueous dispersions and provides polarity sufficient for complexation with water thanks to its dipole moment μ= 6.5 D [29]. Graphene fragments, released through aqueous dispersion upon concentration, reproduce the adsorptive properties of the active natural ShC that was originated in hydrothermal conditions and displayed both meso- and micro-porosity [31]. Nitrogen absorption measurements showed a remarkable increase in adsorption capacity on the powder prepared from dried aqueous dispersion (Table 8). Surprising similarity in values of surface area (S) and adsorption volume (V) for ShC after aqueous dispersion and the most active of natural ShCs from Nigozero supported the hypothesis of geologists concerning hydrothermal migration of the latter.

Table 8. Specific surface and volume adsorption of shungite carbon samples for nitrogen adsorption

ShC samples, treatment	S, m^2/g	V, cm^3/g at p/p_0 =0.95
ShC (Shunga)	11.0	0.004
ShC (Nigozero)	325.0	0.406
ShC dried after aqueous dispersion	325.4	0.45

CONCLUSIONS

Changes in packing of BSU in ShC aggregates provide difference in its activity depending on processes undertaken. As a result of activation, the specific surface of ShC increases by two orders of magnitude. The main contribution to increase in total porosity is made by microporosity.

TEM and SAED have corroborated a substantial change in structural parameters upon modification of ShC: structural nanoporosity increases upon ozonization (the half-width of the first diffraction peak increases), indicating that coherent scattering fields diminish in size in the direction perpendicular to graphene layers; open nanoporosity increases upon steam

activation (size < 100 nm); a 20- to 30-nm-thick dense, homogeneous film was formed which hinder from further penetration of steam inside ShC.

The fullerene-bearing solid phase in the samples after slow evaporation of the aqueous colloidal solutions at ~1^{o}C was revealed by TEM and SAED methods. The phase displays a finely crystalline structure and is similar for both fullerene and shungite aqueous dispersions in formation pattern and morphostructure.

The SAXS method was used to estimate changes in porosity caused by modifying ShC. Upon ozonization, internal ultramicroporosity increases (0.4 nm), whereas activation by steam and steam-CO_2 mixture gives rise to a network of pores, 2.2- 2.5 nm in size and 1.74 nm in fractal dimension, that pierce the carbon structure. Our results are in good agreement with the data obtained by the adsorption and SANS methods.

Nonplanar basic structural elements of ShC, 0.4-0.7 nm in size, contribute greatly to the stabilization of carbon nanoclusters in water passing readily into aqueous dispersion. Releasing of graphene fragments through water is the way of governing its structural organization and properties.

ACKNOWLEDGMENTS

The authors would like to thank Dr. V.V.Kovalevski for performing TEM and SAED measurements and V.I. Siklitsky and M.Yagovkina for conducting SAXS experiments.

The work was supported by Basic Research Program, RAS, Earth Sciences Section-5 and SI Visby project 00996/2008.

REFERENCES

[1] Sokolov VA, Kalinin YuK and Dyukkiev EF. Shungites: *New Carbonaceous Raw Material.s* Petrozavodsk Karelian Recearch Centre, 1984. (in Russian).

[2] Buseck PR, Galdobina LP, Kovalevski VV, Rozhkova NN, Valley JW, Zaidenberg AZ. Shungites: the C-rich rocks of Karelia, Russia. *Canadian Mineralogist* 1997; 35(6):1363-1378.

[3] Solovieva AB, Rozhkova NN, Glagolev NN, Zaichenco NL and Timashev SF.Organic Matter in Schungite and Its Physicochemical Activity in Polymeric Composites Zh. *Fiz. Khim.* 1999; 73(2): 299—305.

[4] Kovalevski VV, Rozhkova NN, Zaidenberg AZ, Yermolin AN. Fullerene-like structures in shungite and their physical properties. *Mol. Mat*. 1994; 4: 77—80.

[5] Kovalevski VV, Buseck PR, Cowley JM. Comparison of carbon in shungite rocks to other natural carbons: an X-ray and TEM study. *Carbon* 2001;39(2):243-256.

[6] Rozhkova N.N., Golubev E.A., Siklitsky V.I., Baidakova M.V., in *Fullerene and fullerene-like structures*, P.A.Vityaz' and E.M.Schpilevski (Eds), 2005, p. 100 (in Russian).

[7] Avdeev M.V., Tropin T.V., Aksenov V.L., Rosta L., Garamus V.M., Rozhkova N.N. Pore structures in shungites as revealed by small-angle neutron scattering, *Carbon* 2006; 44. P.954-961.

[8] Hettich, RL, Buseck, PR. Concerning fullerenes in shungite. *Carbon.* 1996. 5: 685-687.
[9] Heyman D. Search for anciaent fullerenes in anthraxolite, shungite, and thucolite. *carbon*.1995;33:237-239.
[10] Rozhkova NN, and. Andrievsky GV. Fullerenes in shungite carbon. In *Fullerenes and Fullerene like Struktures*, edited by. Pilipenko VA and Poklonski NA, Minsk: Bel. St. University. 2000: 63-68 (in Russian).
[11] Osawa E. Natural fullerenes – will they offer a hint to the selective synthesis of fullerenes? *Fullerene Science and Technology*. 1999; 7 (4): 637—652.
[12] Novgorodova MI. What are fullerenes and fullerites in the world of minerals? *Geochemistry*.1999; 9: 1000-1008.
[13] Zaidenberg AZ, Kovalevski VV, Rozhkova NN and. Tupolev AG. On fullerene-like structures of shungite carbon. *Zh. Fiz. Khim*. 1996;70: 107-110.
[14] Kovalevski V.V., Rozhkova N.N., Zaidenberg A.Z., Yermolin A.N. Fullerene-Like Structures in Shungite and Their physical properties.//*Mol. Mat.*, 1994, 4:77-80.
[15] Zaidenberg AZ, Rozhkova NN, Kovalevskii VV, Lorents DC. Chevallier. Physical chemical model of fullerene-like Shungite carbon. *J. Mol. Mat.* 1996; 8: 107—110.
[16] Kim Kinoshita, editor. Carbon: Electrochemical and physical chemical properties. N.Y.: John Willey and Sons;1988.
[17] Zaidenberg AZ, Kovalevski VV, Rozhkova NN. Spheroidal fullerene-like carbon in shungite rock. in:*Procceeding of the ECS Fullerene Symp*., Reno.1995. NJ: 24—27.
[18] Rozhkova N.N., Golubev E.A., Siklitsky V.I., Baidakova M.V. Shungite as aggregates of carbon nanoparticles. *Abstr.of Int. conf. on Carbon*. Carbon'03 Oviedo (Spain), 2003; 104-106.
[19] Zaidenberg A.Z., Kovalevski V.V, Rozhkova N.N, Spheroidal fullerene-like carbon in shungite rock, *Proc. of the ECS Fullerene Symposium, Reno*, NJ, May 21-26, 1995, 24-27.
[20] Ivankin PF, Galdobina LP, Kalinin YuK. Shungites: problems of genesis and classification. *Soviet Geology*. 1987; 12: 40—47.
[21] Filippov MM, editor. *Organic matter of Shungite-bearing rocks of Karelia*. Petrozavodsk:Karelian Research Center;1994. p. 208.
[22] Rozhkova NN. Shungite-a carbon-mineral filler for polymeric composite materials. *Composite Interfaces*. 2001; 8(3-4): 307—312.
[23] Rozhkova NN. Role of Fullerene-like Structures in the Reactivity of Shungite Carbon as Used in New Materials with Advanced Properties/ E.Osawa (ed.) in *Perspectives of Fullerene Nanotechnology*, Dordrecht: Kluwer Academic Pub. 2002, 237-251.
[24] Kasatochkin V.I, Elizen V.M,, Mel'nichenko V.M, Yurovski I.M, Samoilov V.S. Submicroporous structure of shungite. *Solid fuel Chemistry*.1978; 3:17—21 (in Russ).
[25] Siemieniewska T, Tomkow K, Kaczmarczyk J, Albiniak A, Grillet Y, Francois M. Application of Dubinin-Astakhov equation to evaluation of benzene and cyclohexane adsorption isotherms on steam gasified humic acids chars from brown coal. *Energy and Fuels*, 1990;4:61-70.
[26] Jankowska A, Siemieniewska T, Tomkow K, Jasienko-Halat M, Kaczmarczyk J, Albiniak A, et al. The pore structure of activated chars of brown coal humic acids obtained at increased rate of carbonization. *Carbon*, 1993; 31:.871-880.
[27] Emel'yanova GI, Gorlenko LE, Tikhonov NA, Rozhkova NN, Rozhkova VS Lunin VV. Oxidative Modification of Shungites. *Zh. Fiz. Khim*. 2004; 78(7): 1232-1239.

[28] Gorlenko LE, Emel'yanova GI, Tikhonov NA, Fionov AV, Rozhkova NN, Yankovska A, Lunin VV. The influence of low-temperature gaze-phase oxidation of shungites on their structure and catalytic activity. *Rus.Jour.of Phys.Chem*.2005;79(8):1232-37.

[29] Slin`ko MM, Ukharskii AA, Peskov NV, Jaeger NI. Chaos and Heterogeneous Catalytic systems: CO oxidation over Pd zeolite Catalysts. *Catal. Today*, 2001; 70 (4): 341-357.

[30] Rozhkov SP., Kovalevski VV., Rozhkova NN. Fullerene containing phases obtained from aqueous dispersions of nanocarbons. *Zh. Fiz. Khim*. 2005, 81(5): 1-8.

[31] Rozhkova NN., Gribanov AV., Khodorkovskii MA. Water mediated modification of structure and physical chemical properties of nanocarbons. *Diamond Relat. Mater*. 2007.16: 2104-2108.

[32] Golubev EA., Rozhkova NN. Filippov VN. AFM study of nanocarbon particles aggregates from aqueous dispersions of shungite and fullerenes. *Surface*, 2007. 10, 47-52. (in Russian)

[33] Rozhkova NN, Gorlenko LE, Yemel'yanova GI, Jankowska A, Korobov MV, Lunin VV, Osawa E. The effect of ozone on the structure and physico-chemical properties of ultradisperse diamond and shungite nanocarbon elements/ submitted to *Pure and Appl. Chem*.

Smart Nanocomposites
Volume 1, Issue 1.
ISSN: 1949-4823

FORMATION OF BIMETAL POWDERS ON REACTION OF NANOCRYSTAL PALLADIUM WITH CHLOROCOMPLEXES OF GOLD(III) IN HYDROTHERMAL CONDITIONS

O. V. Belousov[1,2]*, N. V. Belousova[2] and A. V. Burlo[2]
[1]Institute of chemistry and chemical technology of Siberian Branch of the Russian Academy of Sciences; Krasnoyarsk, 660049, Russia
[2]Siberian Federal University; Krasnoyarsk, 660041, Russia

ABSTRACT

The interaction of palladium black with $AuCl_4^-$ in the medium of 1 M HCl at 110 and 130°C was investigated. It was shown that at 110°C, in contrast to 130°C, gold(III) ions are reduced quantitatively from the solution. Dynamics of a change of solid phase composition was analyzed. A formation of substitutional solid (Au, Pd) solutions was found at mentioned temperatures. The reason of formation of the solid solution up to the isolation of palladium was a simultaneous deposition of palladium atoms as a result of its recrystallization and of Au(0) by the reduction with comparable rates of these processes.

Keywords: palladium, gold, solid solution, nanoparticles.

INTRODUCTION

By going from micro- to nanoparticles, qualitative changes of many physicochemical properties of substances, interesting from the viewpoint of their practical use, are observed [1,2]. Superfine noble metals are of the special significance by virtue of their relatively high chemical resistance.

The bimetallic particles are also an attractive subject because their catalytic properties are superior to those of single metallic nanoparticles [3]. There are various methods for obtaining such systems, for example, simultaneous reduction from solutions [3], thermal decomposition of double salts [4], cementation [5-7], sonochemical reduction [8] and so on. At temperatures

* Tel. 007-3912-543627; E-mail: ov_bel@icct.ru, ov_bel@akadem.ru, netnat1@rambler.ru

above 110°C, palladium black reduces to metal platinum and iridium from solutions of their chlorocomplexes and as a result a formation of substitutional solid (Pd, Pt) and (Pd, Ir) solutions take place [5]. The reduction of palladium by nanocrystal rhodium results in the formation of bimetallic mechanical mixture of Pd and Rh [9]. The main factor determining what products (solid solutions or mechanical mixtures) are obtained on cementation by nanocrystal powders is the ratio between the rate of reduction and the rate of coarsening of nanocrystal metal reducing agent [7].

Investigation of contact reduction of $AuCl_4^-$ by nanocrystal palladium in hydrothermal conditions was conducted in this work.

EXPERIMENTAL

The purity of each reagent was at least of CP grade. Muriatic acid was prepared by isothermal distillation. All solutions were prepared in 1 M HCl. Obtaining superfine palladium was performed in accordance with a procedure published elsewhere [10].

Quartz autoclave [9] was filled with 30 ml muriatic solution of $HAuCl_4$. A portion of palladium black calculated so that the molar ratio of n_{Pd}/n_{Au} amounted to 2 or 4 was placed in the fluoroplastic cup. In order for oxygen to be removed, the autoclave was positioned in an argon-filled chamber; the solution was bubbled with argon during 50 min and then was pressurized. Next, the autoclave was vertically inserted into the bore of the stock of an air thermostat which was preheated to the set temperature. After 30 min stirring was turned on. As a result, the solid and liquid phases were separately heated to the predetermined temperature and then brought in contact. As time passed the autoclave was rapidly cooled. A deposit was separated from the solution, repeatedly washed by distilled water to a negative test for chloride ions, dried in a vacuum at 60°C to constant weight, and weighted.

Concentrations of palladium and gold in the solution were determined by atomic absorption method with the use of an AAnalyst-400 spectrometer (PerkinElmer). The chemical composition of solid phase was found by the dissolution of hanging [11] accompanied by atomic absorption analysis. Coincidence between total palladium contents before and after experiments to within 2 % served as a test for the accuracy of performed operations (phase separation and the quantitative determination of the elements in a solution and a solid phase). The structure of solid phase was determined by the X-ray analysis and transmission electron microscopy. X-ray diffraction data were obtained on a DRON-4M powder diffractometer. The microstructure characteristics of materials were determined using the full-profile analysis of X-ray diffraction patterns by the Rietveld method[12]. The procedure was described in more detail elsewhere [10].

RESULTS AND DISCUSSION

The size of palladium crystallites evaluated by the X-ray analysis and the size of particles of palladium determined by transmission electron microscopy agree qualitatively, suggesting that palladium black has a monoblock structure. In general, the particles are near-spherical in shape and aggregate with each other in long chains. The crystallite size amounts to 24 nm.

Previously it was found [10] that palladium black in hydrochloric acid solutions of palladium(II) chloride got coarsened with the rate of growth depending on temperature. Thus, at 180°C, the particle size was as big as 150 nm in 1 h. Decreasing of temperature resulted in reducing of coarsening rate, and at 80°C, as determined from X-ray diffraction data, palladium black underwent no changes even after 8 h. In the absence of palladium ions in the solution, no structural changes of Pd(0) was found up to 180°C. This fact allowed supposing an electrochemical mechanism of coarsening.

It is well known that the equilibrium potential of metal particle in the solution of ions of this metal depends on its radius:

$$E = E_{\infty} - 2V\sigma/(nFr),$$

where E_{∞} is the equilibrium potential for a flat surface, σ is the surface tension at the metal-solution interface, V is the molar volume of metal, n is the number of electrons, F is the Faraday constant, r is the radius of metal particle.

In the case of the contact of two or more of palladium blocks with different dimensions and consequently different potentials, a chain consisting of concatenated short-circuit galvanic cells arises. As a result, smaller blocks dissolve, bigger ones increase.

For simplicity, we will limit ourselves to the consideration of two spherical blocks with different radiuses. The smaller block is an anode and it will dissolve:

$$Pd^{o}(r_1) = Pd^{2+} + 2e.$$

The bigger block acts as a cathode. Palladium atoms deposit on its surface:

$$Pd^{2+} + 2e = Pd^{0}(r_2).$$

The coarsening process is schematically presented in Figure 1.

In parallel with the coarsening process, a partial dissolution of palladium black caused by the presence of chemisorbed oxygen occurs in muriatic solutions as evidenced by data shown in Figure 2. These data are adequately described by the following equation:

$$2C_{Pd(II)}V = 6\,\alpha\,\frac{m}{d\cdot\rho}\,, \qquad (1)$$

where $C_{Pd(II)}$ is the increase of palladium(II) concentration in the muriatic solution, V is the solution volume, ρ is the density of palladium(0), m is the sample weight of palladium(0) (varied over a range from 50 to 550 mg), d is the particle diameter (28, 60 and 200 nm), α is the quantity of adsorbed oxygen per unit of area. The found value of α agrees satisfactorily with published data [13].

An interaction of palladium black with muriatic solutions of $HAuCl_4$ according to the reaction

$$2HAuCl_4 + 3Pd^0 + 4HCl \rightarrow 2Au^0 + 3H_2PdCl_4 \quad (2)$$

begins almost right away on their contacting both at 130 and at 180°C as indicated by a change of solution color from yellow to red-brown. Thermodynamic estimate shows that the equilibrium of this reaction is heavily displaced in the direction of products, with the efficiency increasing with temperature.

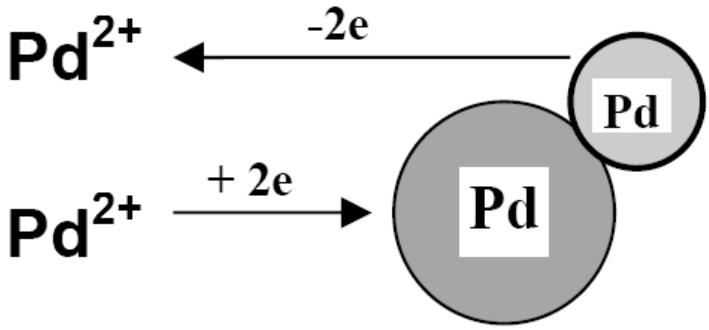

Figure 1. Scheme of palladium black coarsening.

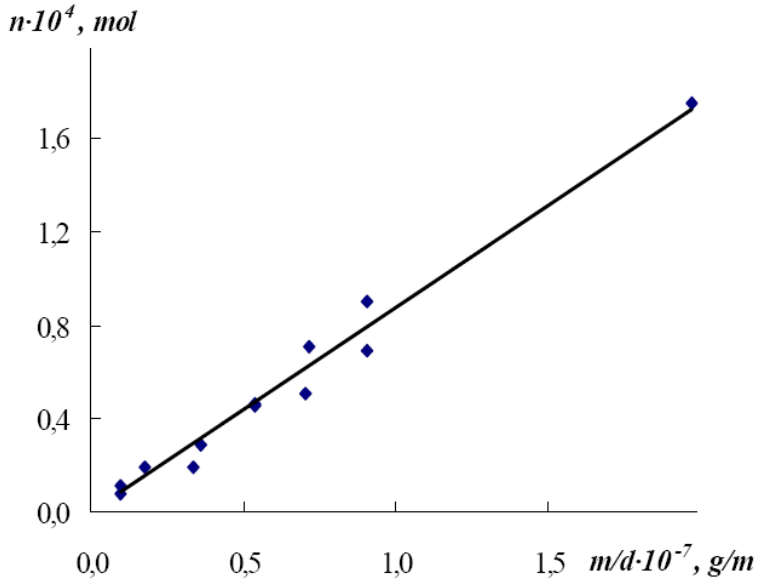

Figure 2. Dependence of the number of Pd(II) moles in solution (n) on the ratio of palladium hanging to diameter of particles (m/d).

At a temperature of 110°C and the molar ratio of n_{Pd}/n_{Au} equal to 2 or 4, gold(III) in solution was not found out in 8 and 4 h, respectively, i.e. reduction was complete (Figure 3).

Increasing temperature doesn't result in the noticeable change of reducing rate, and, what is of particular interest, a quantitative reduction of Au(III) is not obtained, no change of solution composition occurs in 4 h, with the replacement of the molar ratio of n_{Pd}/n_{Au} from 2 to 4 having no effect on the overall picture of process (Figure 4). This fact is explained by an

isolation of palladium particles by gold(0). The X-ray diffraction analysis demonstrated that in all cases the solid phase contained (Au, Pd) substitution solid solutions.

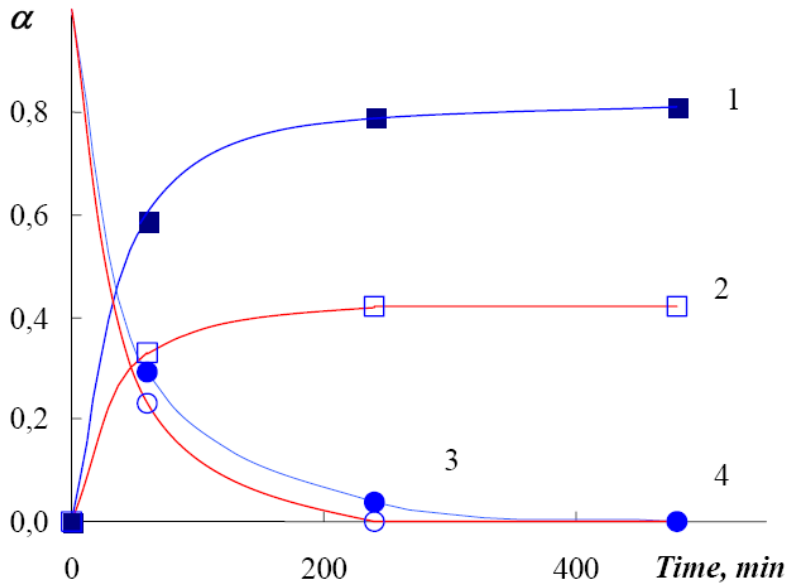

Figure 3. Degree of Pd(II) accumulation in solution (1, 2) and of Au(III) consumption (3, 4). Open markers - $n_{Pd}/n_{Au} = 2$, full markers - $n_{Pd}/n_{Au} = 4$. T = 110°C.

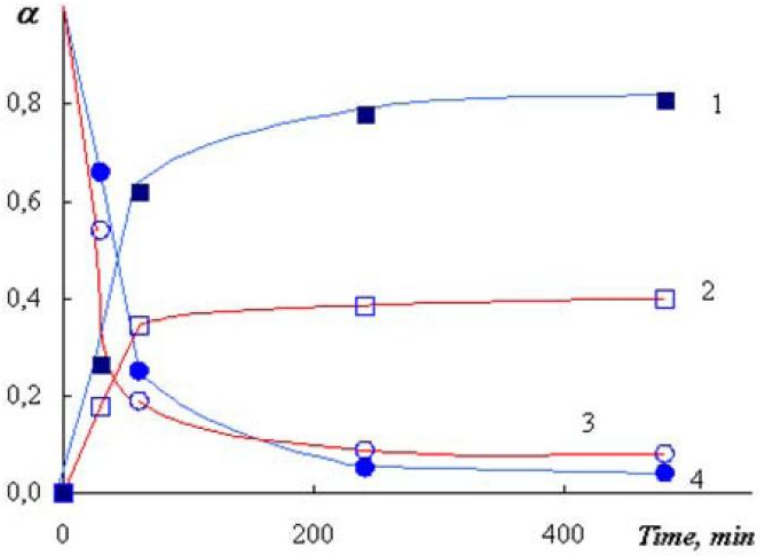

Figure 4. Degree of Pd(II) accumulation in solution (1, 2) and of Au(III) consumption (3, 4). Open markers - $n_{Pd}/n_{Au} = 2$, full markers - $n_{Pd}/n_{Au} = 4$. T = 130°C.

Their formation can be justified using the mechanism of coarsening of palladium black cited above. But in this case a simultaneous precipitation of palladium and gold atoms on the bigger particle takes place. Besides, the formation of solid solution can be explained by a high

diffusion mobility of gold atoms. The solid phase formed at 130°C is a two-phase system: the core of palladium(0) is surrounded by the (Au, Pd) substitution solid solution. The chemical reaction was complete in 4 h. (Figure 4). Further changes are related only to phase transformations. Line broadenings in roentgenograms decrease, i.e. the solid solution becomes more homogeneous in its chemical composition, the portion of palladium(0) phase decreases. The strong broadenings of diffraction lines were observed with samples obtained at 110°C (Figure 5). We explain this fact by a great chemical heterogeneity of solid solutions and a little contribution of diffusion processes.

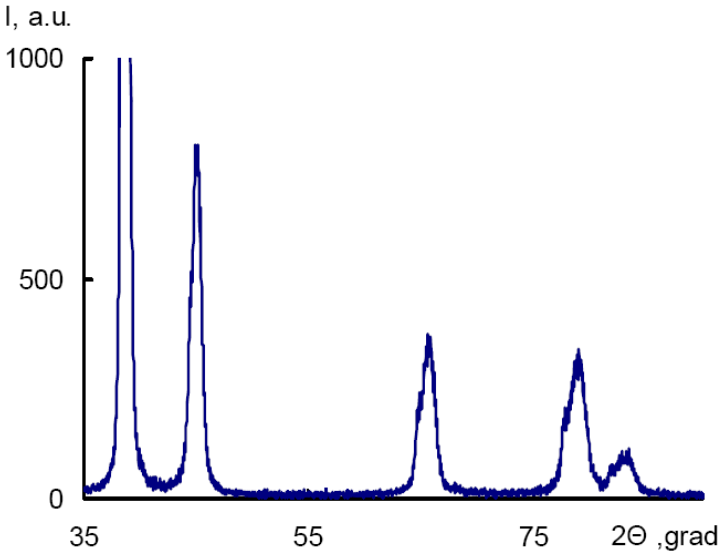

Figure 5. X-ray analysis of powder: experiment time = 8 h, T = 110°C.

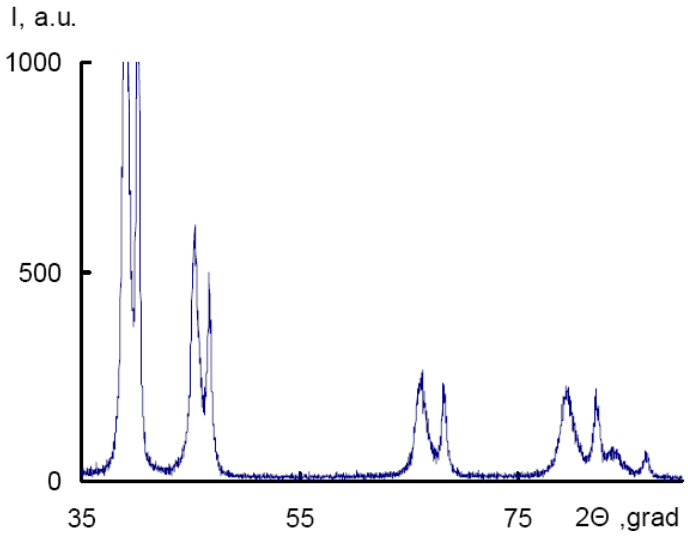

Figure 6. X-ray analysis of powder: experiment time = 1 h, T = 130°C.

It is known [14] that the melting point can decrease considerably as the particles decrease in size. The difference in diffusion mobility of gold atoms at different temperatures results in the observed disparity at 110 and 130°C temperatures. It can be supposed that higher diffusion mobility of nanocrystal gold formed at 130°C promotes, on one hand, the isolation of palladium and, on the other hand, the decreasing heterogeneity in chemical composition. Figure 6 gives diffraction data showing the presence of two phases in the system, namely, palladium black and (Au, Pd) substitution solid solution.

As the length of experiment time extends, the fraction of a palladium phase decreases and is not detected by X-ray analysis after 8 h. The phase of gold(0) was not found in all experiments; apparently, it constituted a thin amorphous layer.

Thus, the formed particles consist of the palladium core surrounded by the (Au, Pd) substitution solid solution which in turn is covered by the thin layer of gold.

REFERENCES

[1] H. Gleiter, *Acta Mater*. 48(1), 1 (2000).
[2] A. Rempel', *Russ Chem Rev*. 76(5), 474 (2007).
[3] R. Harpeness, A. Gedarken, *Langmuir*. 20(8), 3431 (2004).
[4] S. V. Korenev, Yu. V. Shubin, A. V. Belyaev, *Russ. J. Inorg. Chem*. 46(1), 62 (2001).
[5] N. L Kovalenko; O. V. Belousov, L. I. Dorokhova; S. M. Zharkov. *Russ. J. Inorg. Chem.* 40(4), 657 (1995).
[6] J. Brent Hiskey, J. Lee, *Hydrometallurgy*. 69(1), 45 (2003).
[7] N. L. Kovalenko; O. V. Belousov, L. I. Dorokhova, *Russ. J. Inorg. Chem*. 47(7), 967 (2002).
[8] Y. Mizukoshi, T. Fujimoto, Y. Nagata, R. Oshima, Y. Maeda, *J. Phys. Chem*. B. 104(25), 6028 (2000).
[9] N. L. Kovalenko, O. V. Belousov, V. B. Grizan, *Russ. J. Inorg. Chem*. 42(7), 1019 (1997).
[10] V. Belousov, L. I. Dorokhova, L. A. Solov'ev, S. M. Zharkov, *Russ. J. Phys. Chem*. 81(8), 1303 (2007).
[11] E. N. Gil'bert, L. N. Shabanova, N. L. Kovalenko, G. L. Bukhbinder, G. G. Soldatenko, V. A. Kabaeva. *J. Anal. Chem*. USSR. 46(7), 1019 (1991).
[12] H.M. Rietveld, *J. Appl. Cryst*. 2(2), 65 (1969).
[13] V. I. Savchenko, *Russ. Chem. Rev*. 55(3), 222 (1986).
[14] P. Buffat, J.P. Borel, *Phys. Rev. A*. 13(6), 2287 (1976).

MANUSCRIPT PREPARATION SPECIFICATIONS

To ensure more rapid publication and to eliminate the possibility of typesetting errors please include an electronic copy along with a paper copy.

ORGANIZATION

All manuscript headings must be kept consistent within the publication. Manuscripts should consist of the following:

1. Title - typed in capital letters.
2. Author's name.
3. Affiliation - and short address (including country).
4. Abstract - a short abstract (not to exceed 200 words) should be self-explanatory and summarize the paper's essential qualities.
5. Introduction - the introduction should define clearly the nature of the problem. Reference should be made to previously published pertinent papers, accenting the major original contributions.
6. Body - gives the primary message of the paper in detail, may be broken down into sections and subsections. The section and subsection titles should have one blank line space before and after it (section titles in capitals, subsections in initial capital lower case). The contributions made by the author(s) should be clearly stated. Appropriate figures and tables may be used to amplify the text discussion. Each should be numbered consecutively, using Arabic numerals (e.g., Figure 1, Figure 2; Table 1, Table 2, etc.). All figures and tables should be referred to in the text in their numerical order (i.e., do not refer to Table 3 before Table 2). Please do not underline on the original copy to clearly emphasize, please do so on the copy.
7. Conclusions - one blank line before and after "Conclusion". The conclusion should point out the significance of the work, applications of the results and may make recommendations to further work.
8. Reference format - please use the standard format you are accustomed to and are already using. If any problems arise we will contact you.

TECHNICAL PREPARATION

All photographs, charts and diagrams are to be referred to as "Figures", and should be numbered consecutively in the order in which they are referred to in the text. Brief captions should be provided to make the figure as informative as possible (these captions should be typed consecutively on a separate page or pages at the end of the paper). Each caption should give the Figure number.

Photographs should be of good quality (black and white glossies) and submitted in a separate envelope, with the author's name, figure number, and top of the photo clearly marked on the back.

Line illustrations must be clearly drawn in indian ink on good quality white paper or vellum. They should be labeled clearly by typewriter. (If this is not possible, two prints

should be supplied, one appropriately marked and the other unmarked for Nova Science to set).

COPIES REQUIRED

One original paper version (including illustrations) and the computer diskette should be submitted. Please send via regular mail to Frank Columbus, Editor-in-Chief, Nova Science Publishers Inc., 400 Oser Avenue, Suite 1600, Hauppauge, NY 11788-3619. If for any reason regular mail should be inconvenient, please send via e-mail to novaeditorial@earthlink.net. Please send a separate e-mail message informing us that you are sending the files.

PROOFS

The corresponding author receives proofs of his/her article, which should be read, corrected, and returned to the Publisher within 10 days of receipt.

COPYRIGHT TRANSFER

Upon acceptance of an article by the Publisher, the author(s) transfers copyright of the article to the Publisher. The transfer will ensure the widest possible dissemination of information under the U.S. Copyright Law.